SELF-ASSEMBLY OF POLYSTYRENE NANOSPHERES AND ITS APPLICATIONS AS TEMPLATES FOR PLASMONIC STRUCTURES

BY

SHIH-HSIN CHANG

Presented to the Faculty of the Graduate School of

The University of Texas at Arlington in Partial Fulfillment

of the Requirements

for the Degree of

DOCTOR OF PHILOSOPHY

THE UNIVERSITY OF TEXAS AT ARLINGTON

December 2010

ACKNOWLEDGEMENTS

I would like to thank my advisor, Dr. Yaowu Hao. Without his guidance, support, and encouragement, which are not limited to the research, this dissertation would not have been possible.

I would like to thank Dr, Digant P Dave. I learned a lot from him about the optical knowledge and measurement. Without his fully support, this dissertation can not be done.

I would like to thank Dr. Choong-Un Kim, Dr. Weidong Zhou, and Dr. Fuqiang Liu for serving in my thesis committee. I learned a lot from them, not only from the discussions about the research and the courses they taught, but also from their approaches to research and teaching.

I would like to thank James Nyagilo in Dr. Digant P Dave' research group. He helped me much about the measurement of the optical properties and provided me useful opinions about this project.

July 27, 2010

ABSTRACT

SELF-ASSEMBLY OF POLYSTYRENE NANOSPHERES

AND ITS APPLICATIONS AS TEMPLATES

FOR PLASMONIC

STRUCTURES

Shih-Hsin Chang, PhD

The University of Texas at Arlington, 2010

Supervising Professor: Yaowu Hao

Monodispersed colloidal polystyrene spheres have been self-assembled into various structures as templates for the fabrication of different nanostructures. Two unique self-assembly processes have been developed and systematically investigated. A method to make the multi-layer and mono-layer close-packed structure by means of capillary-convective force has been developed. By directly visualizing the self-assembling process using optical microscopy, a mechanism based on the 2-D crystal formation and 3-D repulsive force model has been proposed to explain the process. A vertical deposition technique to produce nanosphere crystal structure with single

orientation on hydrophilic glass substrate has also been developed. Using a lithographically patterned substrate with alternating areas of glass and Au, self-assembled crystal structures can be generated on the hydrophobic Au surface. It has been found that the contact angle of the colloid solution on the substrates controls this self-assembly process.

Using self-assembled polystyrene nanosphere crystals as templates, Au nanovoid arrays, in which the voids about several hundreds of nanometer in diameter are embedded in a gold film with a thickness less than the void diameter, have been fabricated by templated electrodeposition. In order to use Au nanovoid arrays as surface enhanced Raman scattering (SERS) sensors on optical fiber tips for in situ and in vivo applications, a new structure has been designed. In such structure, each void has optical openings on both sides of the nanovoid array, one side is mounted to the fiber tip surface for introduction of incident light and collection of scattered light and the other side is for interrogation of analyte molecules in the voids. The effect of structural parameters, including void diameter, Au film thickness, and the bottom hole diameter of the nanovoid arrays on the electric field confinement are investigated using three-dimensional finite difference time domain (FDTD) simulation. Fiber-based SERS sensing applications have successfully been demonstrated.

TABLE OF CONTENTS

LIST OF ILLUSTRATIONS

Figure Page

LIST OF TABLES

Table Page

CHAPTER 1

INTRODUCTION

In the last two decades, the monodispersive colloidal nanospheres, mainly polystyrene and silica, with sizes ranging from tens of nanometers to micrometers have become commercially available. These nanospheres can be self assembled to create large areas of either dispersive or continuous periodic array of patterns. Such patterns can serve as the etching or shadow mask to fabricate nanostructures for various applications. This process is termed as nanosphere lithography. For example, a hexagonal array of isolated metal dots on the substrate can be created simply by the evaporation of desired metal onto the intervals of a close-packed nanosphere array. More importantly, the patterns generated using nanosphere lithography are good candidates for the fundamental studies of the roughness and/or periodicity effect on the physical properties of structures.

Using self-assembled polystyrene nanosphere crystal as templates, metal nanostructures such as Au, Ag and Cu can easily be generated by electrochemical deposition into the interstitial space between particles followed by removal of the template in a suitable solvent, creating an inverse replica of the nanosphere crystal. Au and Ag nanostructures with dimension smaller than 100nm exhibit a unique optical property, surface plasmon resonance (SPR) effect, and it can be used for various sensing applications such as surface enhanced Raman scattering (SERS).

Surface plasmon resonance is a nanoscale size effect of the interaction of an electromagnetic wave with the conduction electrons in a metal. When a metal is under the irradiation of light, the electric field drives the conduction electrons to oscillate. This collective motion of electrons has its resonance frequency, plasma frequency, and the quanta of this collective oscillation are called plasmons. When dimensions (at least one) of the metal is much smaller than the wavelength of the light, this collective excitation mode of the plasma will be localized near the surface, and the resonant frequency will shift from the ordinary plasma frequency to Surface Plasmon Resonance (SPR) frequency. The SPR frequencies lie in visible light range for Cu, Ag and Au nanostructures. The incident light at SPR frequency is strongly absorbed and scattered, i.e. the electric field associated with the incident light will be greatly enhanced. The SPR frequency and cross-section of SPR scattering and absorption are dependent on the size and morphology of the nanostructures. Due to such concentrated electric field resulting from SPR, when a molecule is in the close proximity of a metallic nanostructure its Raman scattering can be enhanced dramatically (a factor of 10^6-10^{14}). This phenomenon can be used as an extremely sensitive and selective technique for identifying molecular species

Raman spectroscopy is a useful technique to detect and identify molecules by sensing the energy difference between the incident and scattered light related to a particular set of vibration modes. Because of the distinct sharp spectral lines produced, Raman spectroscopy can be used to analyze the multi-components samples simultaneously without tedious separation procedure. However, the Raman signals are

very weak in general due to the inherently low cross-section of the Raman scattering. Therefore, it can be applicable only for detecting high concentration of the analyte molecules. About thirty years ago, it was discovered that the Raman signals can be significantly enhanced by placing the molecules onto the rough metal surface. This phenomenon was explained and referred to as surface-enhanced Raman scattering (SERS). Since then, surface-enhanced Raman spectroscopy has become one of the most important tools in analytical and surface science with enormous promise for high sensitive and selective detection of extremely low concentration molecules.

Optical fibers are an ideal platform for detecting the SERS signal of analytes in remote and/or of small samples volume, offering the ability to probe solutions for in situ chemical sensing and in vivo biosensing. However, fabrication of fiber SERS probes which are cost effective and produce reproducible results is rather challenging. In the past few years a number of fiber-based SERS probes have been demonstrated. Nanoparticle-based fiber SERS probes are simpler to fabricate but their reproducibility is poor and analyte quantification is not possible. Large Raman enhancements occurs in narrow gaps between nanoparticles, where high enhancement of electric field occurs due to SPR.. Because the SPR is extremely sensitive to the morphology of the metal nanoscale features, the number and location of so-called “hot spots” – areas with larger enhancement on these fiber-probe surfaces are unknown, leading to a poor reproducibility. Nanolithographically patterned arrays greatly improve the reproducibility but their fabrication is expensive and difficult. Moreover, since the enhanced electric field strength dramatically decreases with the distance (d) from the

particle surface (a d^{-12} dependence), dropping almost to zero even just 10 nm away from the surface, the detection requires that analyte molecules bind or be in very close proximity to the nanosurface. For detecting molecules in a solution, this greatly hampers the sensitivity or a long waiting time is required for molecules to diffuse to the surface which would lead to very long response time.

Nanosphere self-assembly technique has shown the potential to overcome the limitation and inconveniences of these standard methods to produce the sensitive and reproducible SERS substrates with high throughput and low cost. In addition, owning to the availability of the nanospheres with different sizes in the range of tens of nanometers to micrometers, large periodic arrays of patterns with different sizes can be easily created. In the last few years, the nanovoid structure, where the voids about several hundreds of nanometer in diameter are embedded in a metal film with a thickness less than the void diameter, has been shown the potential to be the reproducible SERS substrate with a high enhancement factor. Electromagnetic fields are strongly confined in and around the nanovoids, acting as plasmon resonators. The nanovoid array structure can be produced by templated electrochemical deposition through self-assembled polystyrene spheres. The plasmon modes can be tuned simply by the choice of sphere size and electrochemical deposited thickness of the film. More importantly, compared to other particle-based structures where the effective fields are less than 10 nm away from the surface, the intensive fields exist up to 100 nm above the metal surface, which dramatically increase the volume of SERS-active zone

dramatically, and therefore, these nanostructures are particularly suitable for fiber-based sensor.

In this thesis, two nanosphere self-assembly techniques have been developed and been systematically studied. Using these techniques, polystyrene nanosphere crystal templates for Au electrochemical deposition have been assembled. Au nanovoid arrays for optical fiber tip have been fabricated, and their plasmonic properties have been investigated through computer simulation and experiments. Sensing applications, including plasmonic sensors and SERS, have been demonstrated.

CHAPTER 2

BACKGROUND INFORMATION

In this chapter, the properties of the colloidal solution, and the theory and method to make the dispersed and periodic array of nanospheres are first introduced. Then, the principle of Raman scattering, the role of the surface plasmon in the surface enhanced Raman scattering, and the development and challenge of the fiber probe in the surface enhanced Raman spectroscopy are introduced.

2.1 Self-assembly of Polystyrene Nanospheres

In the last two decades, polystyrene nanospheres with sizes ranging from tens nm to several μm have become commercially available in a large amount with an exceedingly uniform size distribution. Colloidal particles can self-organize on the surfaces to form the large area of dispersed or periodic array of nanospheres, which can be used as lithographic masks/molds to produce various nano-sized surface structures or novel shape of nanoparticles. Therefore, they can be applied in many areas such as biosensors[1, 2], biomaterial[3], photonic crystals. Here, the characteristics of colloidal solution and the methods and mechanisms for two types of patterns created will be discussed.

2.1.1 Colloidal solution

A solution is composed of solute and solvent. Normally, the maximum diameter of solute particles in a solution is around 1 nm. If the size of solute particles is larger than 1 nm, in the range of 1 to 1000 nm, then we call this solution as colloidal solution. In a colloidal solution, solute particles are not really dissolved into solvent, but they disperse uniformly inside the solvent. As we know, the solute particles in the solvent experience the Brownian movement caused by the vigorous barrage of the rapidly moving molecules of solvent. This motion can cause the collision to happen between particles. When the particles collide, they stick together forming larger particles and settle out of the solution. How can the solute particles of the colloidal solution disperse in the solvent uniformly?

There are two main mechanisms. First, the colloidal particles have large surface area, thus, they can absorb a lot of same types of charges on the surface from the solution, inducing the repelled force between them. Second, due to the charges on the surface of the particles, the water molecules in their vicinity are preferentially oriented, forming a primary and secondary hydration shell of oriented water molecules around colloidal particles[4]. When colloidal particles collide, they do not actually touch each others, and only the water layers contact. Therefore, the particles do not stick together and can stay in the solution. Nowadays, a variety of colloidal particles with positive or negative charges directly created on the surfaces during synthesis process to increase the dispersive property are commercially available. In this study, the colloidal particles used are polystyrene particles.

2.1.2 van der Waals and Double-layer Potentials between Colloidal Particles

van der Waals potential

In colloidal chemistry, the van der Waals and double-layer potentials play main roles in the long-range interactions between particles and surfaces in a solution.

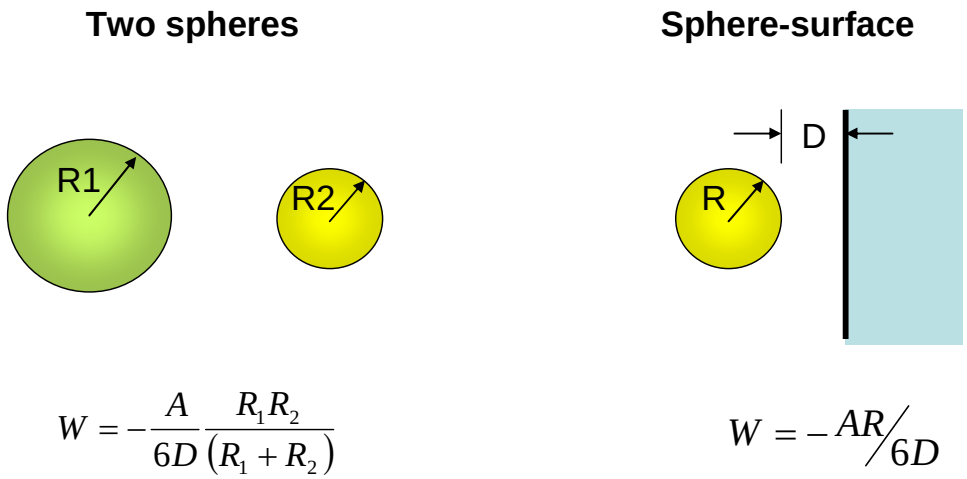

Figure 2.1 Van der Waals interaction free energies between two spheres and between sphere and surface calculated on the basis of pairwise additivity.

Roughly speaking, van der Waals potential arises from interaction between the atomic or molecules dipoles. The interatomic van der Waals pair potential has the form, $w(r) = -C/r^6$. The two-body van der Waals potential can be obtained by integrating the energies of all atoms in one body with all the atoms in the other. The resulting van der Waals interaction energy for two-spheres and sphere-surface system **(Figure 2-1)** can be expressed as[4]:

two-spheres $$W = -\frac{A}{6D}\frac{R_1 R_2}{(R_1 + R_2)} \qquad \textbf{(2-1)}$$

sphere-surface $W = -AR/6D$ **(2-2)**

where, A is called Hamaker constant, that is related to the material properties of the particle. The van der Waals force between similar particles in solution is always attractive.

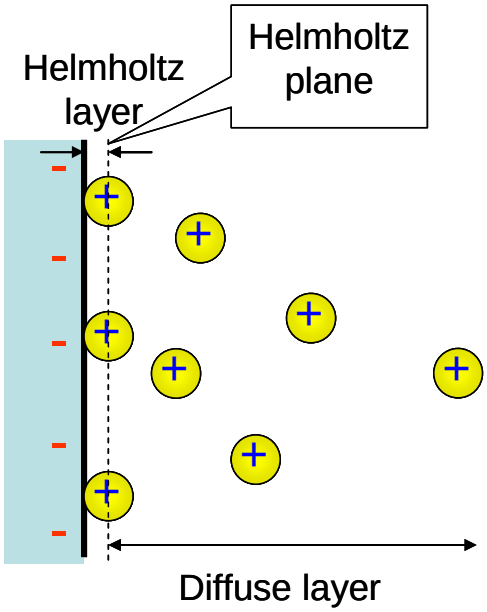

Figure 2.2 The surface charge is balanced by an equal but oppositely charged region of counterions, some of which are bound to the surface within the Helmholtz layer, the others form the diffuse double layer.

Double-layer potential

When the particles suspend in the solution, they are usually charged in two ways to prevent from coalescing by the repulsive electrostatic forces: i) by dissociation of surface group, and ii) by adsorption of ions from the solution. In the steady state, the surface charge is balanced by the same oppositely charged region of counterions, which

is composed of two layers: the Helmholtz and diffuse electric double layers **(shown in Figure 2-2)**. The plane in the interface is called Helmholtz plane. The numerical solution of electrostatic potential can be obtained by solving the nonlinear Poisson-Boltzmann equation:

$$\nabla^2\psi = -\frac{e}{\varepsilon_r\varepsilon_0}\sum_i z_i\rho_{0i}\exp\left(-z_i e\psi/kT\right) \qquad \textbf{(2-3)}$$

The double-layer force can be calculated by the equation[5, 6]:

$$F = \iint_s \left\{\left[kT\sum\left(\rho_i-\rho_{0i}\right)\right]I\bullet n + \left[\frac{\varepsilon_r\varepsilon_0}{2}E^2 I\bullet n - \varepsilon_r\varepsilon_0(E\bullet n)E\right]\right\}dS \qquad \textbf{(2-4)}$$

where

$$\rho_i = \rho_{0i}\exp\left(-z_i e\psi/kT\right) \qquad \textbf{(2-5)}$$

$$E = -\nabla\psi \qquad \textbf{(2-6)}$$

ε_m is the dielectric constant of medium; ε_0 is the permittivity of free space; Ψ is the electrostatic potential; z_i is the valency of ion species; ρ_i is the concentration of ion species and ρ_{0i} is the concentration of ion species in the bulk; I is the unit tensor; E is the electric field.

Once the force is known, the double-layer interaction energy Φ can be calculated by directly integrating the force with respect to the distance between the bodies. The surface charge density for the planar surfaces can be found from the Grahame equation[4]:

$$\sigma^2 = 2\varepsilon_r \varepsilon_0 kT \sum_i \{\rho_{\infty i}[\exp(-z_i e\psi_s / kT) - 1]\} \qquad \textbf{(2-7)}$$

In a low surface potential, the Grahame equation simplifies to

$$\sigma = \varepsilon_r \varepsilon_0 \kappa \psi_s \qquad \textbf{(2-8)}$$

where

$$\kappa^{-1} = (\sum_i \rho_{\infty i} e^2 z_i^2 / \varepsilon_r \varepsilon_0 kT)^{-1/2} \qquad \textbf{(2-9)}$$

is called as Debye-length, the magnitude of which depends only on the property of the solution. The repulsive interparticle electrostatic interaction can be characterized by the Debye-length.

The approximate analytical solutions of non linear Poisson-Boltzman equation for the two spheres and sphere-plane systems are available by different methods, such as linear superposition approximation (LSA) method. In this method, the interaction energy can be expresses as[5, 7, 8]:

$$\phi_{sphere-plane}(x) = 4\pi\varepsilon_r \varepsilon_0 a(kT/e)^2 Y_{sphere} Y_{plane} \exp(-\kappa x) \qquad \textbf{(2-10)}$$

$$\phi_{sphere-sphere}(x) = 4\pi\varepsilon_r \varepsilon_0 a(kT/e)^2 [a^2/(2a+x)] Y_{sphere}^2 \exp(-\kappa x) \qquad \textbf{(2-11)}$$

where Y_{sphere}, Y_{plane} are effective reduced surface potentials and related to the surface potential Ψ_s, which is correlated to the surface charge σ as shown in the Grahame equation. Therefore, if the surface charge is known, then the interaction energy can be obtained from the calculation. From the equations above, we can see the double-layer interaction energies are strongly related to the Debye-length κ^{-1}.

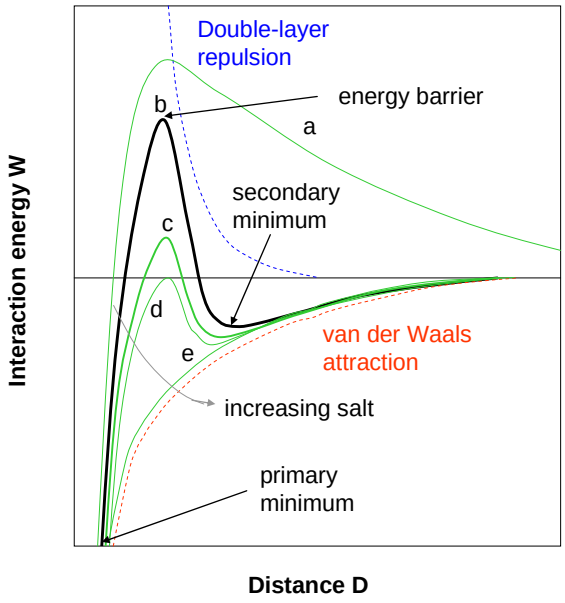

Figure 2-3 Energy vs distance profiles of DLVO interaction. (a) Strong surface charge; colloidal particles are stable. (b) Particles will either sit in the secondary minimum or remain dispersed in the solution. (c) Particles come into secondary minimum and coagulate slowly. (d) Critical coagulation concentration; colloids coagulate rapidly. (e) Particles attract each other at all separation.

The stability of the colloidal solution can be described by combining the van der Waals and double-layer interaction energy in the system, which is called as Derjaguin-Landau-Verwey-Overbeek (DLVO) theory. As shown in the **Figure 2-3[4]**, there is a strong repulsive peak for the highly charged surface in a dilute electrolyte solution. For more concentrated electrolyte solution, the secondary minimum appears. In this case, due to the high energy barrier, the particles stay in secondary minimum. The lower the surface charge, the more particles overcome the energy barrier, leading to a slow aggregation. However, when the concentration of the electrolyte becomes too high,

larger than the critical coagulation concentration, where the energy barrier falls below W=0, the particles aggregate rapidly.

2.1.3 Formation of Dispersed Array of Nanospheres

Colloidal particles have the ability to self-organize to form ordered structures on a substrate with opposite charges by the attractive adsorption under the influence of electrostatic repulsive interactions between particles [9-11]. The average distance between colloidal particles dispersed in solvent can be described by the random sequential adsorption model (RSA)[8, 12, 13]. In the classical RSA model, the colloid particles, treated as hard, non-interacting spheres, are placed sequentially on the surface randomly without overlap with previously adsorbed particles. The jamming limit, where the density of particles saturates, is about 0.547 at infinite adsorption time. However, in real situations, a lot of parameters like particle-surface and particle-particle interactions will affect the adsorption process, leading to very different results. Therefore, a more realistic extended RSA model was developed to describe the particle adsorption. In such approach, the lateral interaction between particles are taken into account by the pairwise summation approximation, where the interaction energy of the pair, based on the double-layer model, is calculated vie the linear superposition approximation (LSA) for spherical particles. Because the double-layer interaction energy is related to the surface charge and Debye-length, therefore, the distance between the particles and saturation coverage can be controlled by the salt concentration, pH, and particle and surface charges [14-16]. Due to the improvement of technique for the synthesis of colloidal nanospheres, a varity of monodisperse nanospheres with different types of charges are

commercially available. Therefore, through self-assembly process, a large area of uniformly dispersed nanospheres on the substrate with adjustable size and space can be formed conveniently and rapidly, which enable them to act as lithographic masks for the production of nanosize structures.

2.1.4 Formation of Periodic Array of Multi-layer Nanospheres

Multi-layered colloidal crystalline assemblies are very useful in many fields, such as acting as templates to form porous structure, as diffractive elements in sensors or photonic bandgap structures.

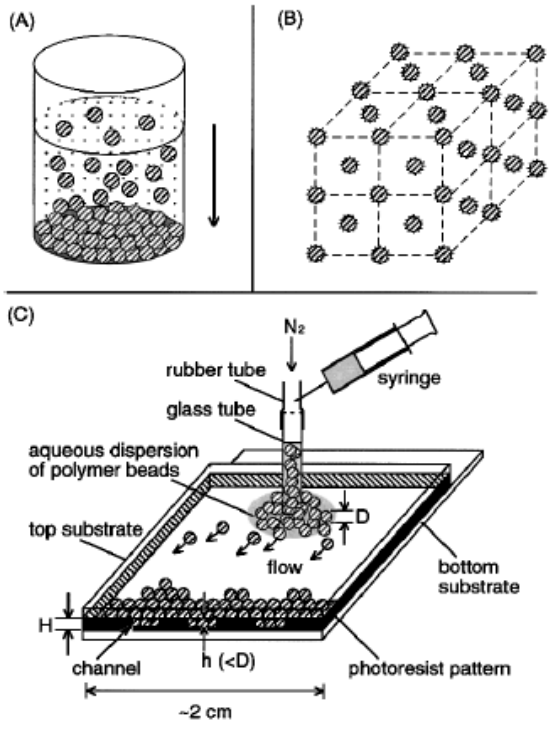

Figure 2-4 (a) Sedimentation in the gravitation field. (b) Ordering via repulsive electrostatic interaction. (c) Crystallization through physical confinement.

There are a number of reported methods to assemble the 3-D periodic array of colloidal nanospheres. They can be roughly categorized, **as shown in the Figure 2-4[17]**, into three types: (1) Sedimentation in a force field[18-20]. (2) Crystallization via repulsive electrostatic interaction[21]. (3) Self-assembly under physical confinement [22, 23]. In the sedimentation method, several parameters like gravitational settling, translational diffusion and crystallization have to be precisely controlled. Normally, only the nanoparticles with high density and neutral or very low charges can be assembled using this method. In the second method, the highly charged colloidal spheres can spontaneously organize themselves into a variety of crystal structures due to the fact that a minimum energy state can be reached when particles form a periodical structure. There are three energy terms involved: van der Waals interaction energy, doubled layer interaction energy, and long-range attractive interaction energy between like-charged spheres. Disorder to order transition can be provoked by increasing the volume fraction or the screening length of the particles. However, this method is very sensitive to the temperature, monodispersity, density of charges on the surface of the spheres, electrolytic concentration, and concentration of spheres. The process is not easy to control and the required volume fraction is usually low. Moreover, the intervals of the spheres are filled with polygel, so it is impossible to deposit the metal into them to form porous structure. In the third method, the periodic array of nanospheres is formed within an engineered physical confinement. Comparing to other two methods, this method is relatively fast, and it can provide a good control on the morphology of

the surface of resulted crystal and the number of layers. The drawback of the method is that it involves a lot of steps during the process.

2.2 Plasmonics and Principle of Surface Enhanced Raman Scattering (SERS) Effect

2.2.1 Surface Plasmon

Plasmons are referred to the collective oscillations of the free electron gas. Suppose that a metal cube exposes to a uniform field, electrons will move in the opposite direction of the field inside the metal and leave the positive ions on the other side. When the external field is turned off, the electrons will move back driven by the attractive force exerted by the positive ions. The movement will give rise to a "overshoot", which cause them to move back. Thus, electrons oscillate back and forth at a specific frequency, which is called plasma frequency. Plasmons are quantization of this electrons oscillation. Surface plasmons are the plasmons confined to the surface and they can interact with the oscillating electric field in light.

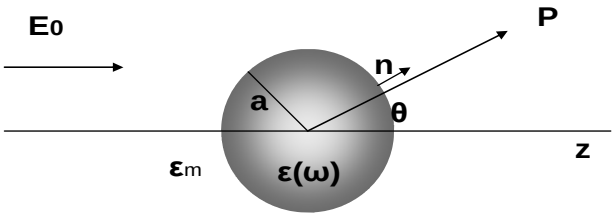

Figure 2-5 A homogeneous sphere placed into an electrostatic field.

Localized surface plasmons

If the metal particle is much smaller than the wavelength of light in the surrounding medium **(Figure 2.5)**, the phase of the harmonically oscillation

electromagnetic field is constant over the particle and the quasi-static approximation can be applied to solve the electron oscillation problem [24]. The first Maxwell equation, correspond to Gauss's law, in a matter can be expressed as:

$$\nabla \bullet D = \rho_f \qquad \textbf{(2-12)}$$

where D is called electric displacement; ρ_f is free charge density. Suppose there is no free charge on the matter and the medium is linear and homogeneous. Then the equation (2-21) becomes the Laplace equation:

$$\nabla \bullet D = \rho_f = 0 \Rightarrow \nabla \bullet E = \nabla^2 \phi = 0 \qquad \textbf{(2-13)}$$

where E is the electric field; φ is the potential. To solve the Laplace equation with suitable boundary conditions for a metal sphere, we can get the potential inside the sphere Φ_{in} and outside the sphere Φ_{out}.

$$\phi_{in} = -\frac{3\varepsilon_m}{\varepsilon + 2\varepsilon_m} E_0 r \cos\theta \qquad \textbf{(2-14)}$$

$$\phi_{out} = -E_0 r \cos\theta + \frac{p \cdot r}{4\pi\varepsilon_0 \varepsilon_m r^3}, \qquad \textbf{(2-15)}$$

$$p = 4\pi\varepsilon_0 \varepsilon_m a^3 \frac{\varepsilon - \varepsilon_m}{\varepsilon + 2\varepsilon_m} E_0 \qquad \textbf{(2-16)}$$

where ε_m is the dielectric constant of medium; ε is the dielectric constant of the sphere; E_0 is the external field; p is the dipole moment; r is the position vector at point P; a is the radius of the sphere.

In equation (2-24), φ_{out} is the superstition of the applied field and that of a dipole located at the sphere center. Thus, the applied field induces a dipole moment p, which is

defined as $p = \alpha E_0$. Therefore, it is apparently that polarizability α has a resonant enhancement, when

$$\mathrm{Re}[\varepsilon(\omega)] = -2\varepsilon_m \qquad \textbf{(2-17)}$$

ε_m : dielectric constant of the medium

This is called Fröhlich condition. Combining with the dielectric function derived from the Drude-Lorentz model under low damping term,

$$\varepsilon(\varpi) = 1 - \frac{\varpi_p^2}{\varpi^2 + i\gamma\varpi} \qquad \textbf{(2-18)}$$

$$\varpi_p = \sqrt{\frac{ne^2}{\varepsilon_0 m}} \qquad \textbf{(2-19)}$$

where ϖ_p is the plasma frequency; n is the number of electrons per unit volume; m is the mass of an electron. We can get:

$$\varpi = \frac{\varpi_p}{\sqrt{1+2\varepsilon_m}} \qquad \textbf{(2-20)}$$

This is called resonant frequency of surface plasmon, and it has a strong dependence on the dielectric environment. For example, the resonance red-shifts when the dielectric constant of the medium increases.

Under plane-wave illumination with $E(r,t) = E_0 e^{-i\omega t}$, the fields induce an oscillating dipole moment $p(t) = \alpha E_0 e^{-i\omega t}$, and leading to the re-radiation. In the near zone, the electric field is:

$$E = \frac{3n(n.p) - p}{4\pi\varepsilon_0\varepsilon_m}\frac{1}{r^3} \qquad \textbf{(2-21)}$$

If the incident light meets the resonant frequency, the external field will be largely enhanced. Another importance consequence is the plasmon resonance of the small metal particles can be excited directly by the light. This result is suitable to the particle size below 100 nm illuminated with visible or near-infrared radiation. For the larger particles, some other techniques have to be used.

Surface plasmon polariton

Surface plasmon polariton are electromagnetic excitations propagating at the interface between a dielectric and a conductor via the coupling of the light to surface plasmon. If the external charge and current are zero on the matter surface, the wave vector β of the surface plasmon polariton on the plane surface, by solving the Maxwell's equation with boundary conditions, can exist only in the TM mode condition and is equal to[24]:

$$\beta = \frac{\omega}{c}\sqrt{\frac{\varepsilon\varepsilon_m}{\varepsilon + \varepsilon_m}} \qquad \textbf{(2-22)}$$

The wave vector β goes to infinity, when ε =- ε_m, and the frequency approaches the surface plasmon frequency ω_{sp}. Recalling Drude-Larentz model under low damping term, we can get

$$\varpi_{sp} = \frac{\varpi_p}{\sqrt{1+\varepsilon_m}} \qquad \textbf{(2-23)}$$

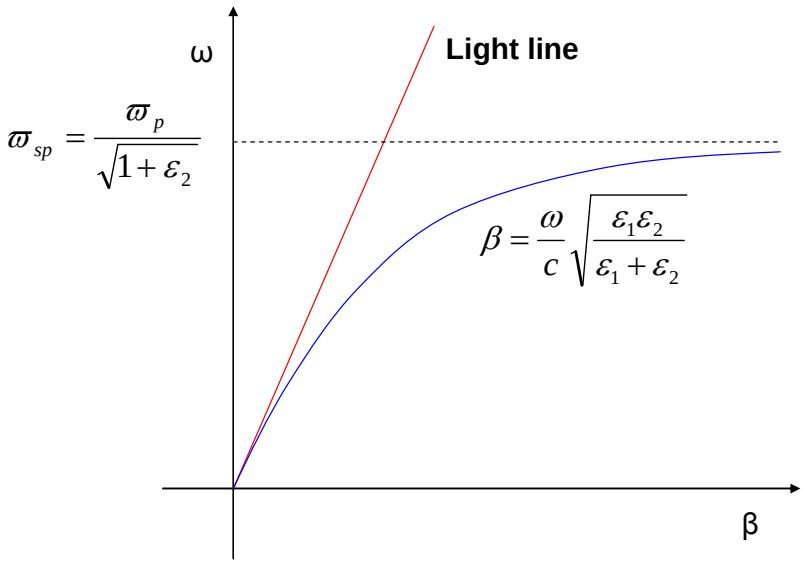

Figure 2-6 Dispersion relation of surface plasmon polariton under Drude model condition.

The dispersion curve for a surface Plasmon mode is shown in the **Figure 2-6**. The surface plasmon polariton has greater momentum than that of a free space photon at the same frequency. Therefore, some techniques are needed to couple the light with the surface plasmon. There are two main methods: prism coupling and grating coupling. In the prism coupling, the light contributes an in-plane wave vector $k_x = k\sqrt{\varepsilon}\sin\theta$ in stead of $k_x = k\sin\theta$, which is sufficient to excite the surface Plasmon polariton at the interface between metal and air. In the grating coupling **(Figure 2-7)**, the in-plane wave vector, due to the interference between light and periodic grating pattern, can be modified to

$$k_x = k_{//} + g_m \qquad \textbf{(2-24)}$$

$$k_{//} = k\sin\theta \qquad \textbf{(2-25)}$$

$$g_m = m\frac{2\pi}{a} \qquad \textbf{(2-26)}$$

which can excite the different surface plasmon modes.

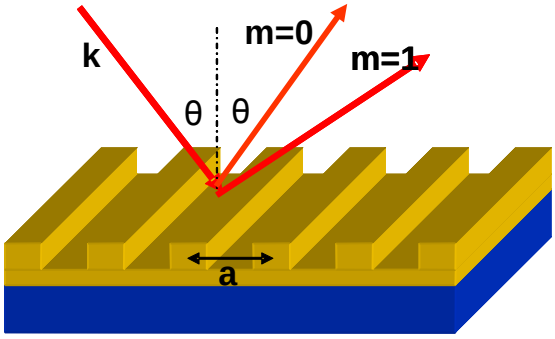

Figure 2-7 Phase-matching of light to SPPs using a grating

2.2.2 Raman Scattering Effect

The atoms in a molecule can vibrate about the bond relative to their equilibrium position. In the practical case, the maximum displacement is small compared to the bond length. Therefore, the potential energy can be expanded in a Taylor series and described by the simple harmonic oscillation. By solving the time-independent Schrödinger equation:

$$-\frac{\eta^2}{2m}\frac{d^2\varphi}{d\chi^2}+\frac{1}{2}m\omega^2\chi^2\varphi = E\varphi \qquad \textbf{(2-27)}$$

We can get the vibrational energy states of each molecular vibrational mode:

$$E_0 = \frac{1}{2}\eta\omega, \qquad E_n = \left(n+\frac{1}{2}\right)\eta\omega \qquad \textbf{(2-28)}$$

Adjacent energy levels differ by one quantum number, $\Delta E_{vib} = \eta\omega$, ω is angular frequency of the vibrational mode, and each vibrational state can be dictated by the Boltzmann distribution function.

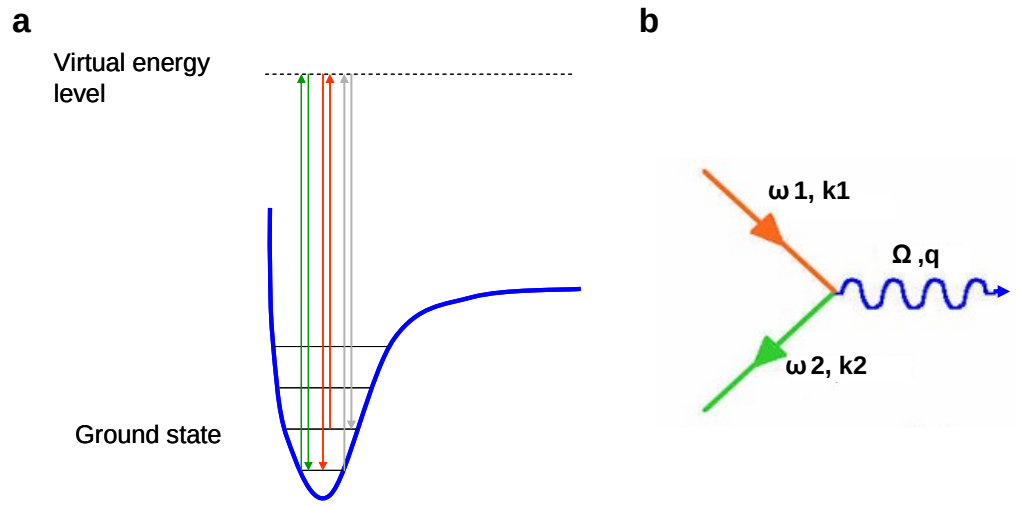

Figure 2-8 (a) Energy level diagram for the ground state and the virtual energy level. Green arrow is Rayleigh scattering; red arrow is anti-Stoke scattering; gray arrow is Stoke scattering. (b) An inelastic light scattering process. The straight arrows represent photons; the wiggly arrow represents the phonon.

When the incident light encounters the matter, the electromagnetic wave induces an oscillating dipole moment and leads the system to a virtual energy state, illustrated in **Figure 2-8(a)**. Normally, the energy level of the virtual state is greater than the vibrational quanta, but not necessarily equal to any particular electronic quantum energy. During the interaction between the photon and molecule, some quantum of energy equals to the vibrational mode may be transferred to the molecules and the longer wavelength is emitted. This is called Stokes scattering. If the molecule is originally in the excited vibration state, it may be back to the lower state and the shorter wavelength

is emitted. This is called Anti-Stokes scattering. The Raman scattering, which is an inelastic scattering, includes the Stokes scattering and anti-Stokes scattering. When the energy state in the virtual state recovers to the original state, the emitted light has the same frequency with the incident light. This is called Rayleigh scattering. Anti-stokes scattering will happen only if there are phonons present in the material. By the quantum mechanical treatment, the ratio of intensity between anti-Stokes and Stokes is given by[25]:

$$\frac{I_{anti-Stokes}}{I_{Stokes}} = \exp\left(-\eta\Omega / k_B T\right) \qquad \textbf{(2-29)}$$

This means the probability for anti-Stokes scattering is very low even at cryogenic temperatures. Raman scattering involves the phonon, leading to the higher order interactions between the photon and molecule **[Figure 2-8(b)]**. Conservation of energy and momentum is required.

$$\omega_1 = \omega_2 \pm \Omega \qquad \textbf{(2-30)}$$

$$k_1 = k_2 \pm q \qquad \textbf{(2-31)}$$

Where ω_1: angular frequency of incident light; k_1 means wave vector of incident light. ω_2: angular frequency of scattered light; k_1 means wave vector of scattered light. Ω: medium frequency; q: medium wave vector. Therefore, the light emitted due to this criteria is very weak compared to Rayleigh scattering. Whether the vibrational mode is Raman active or not should be determined by the selection rule, which resulted from the group theory[26]. To get the full treatment, the theory of quantum mechanism has to be involved. However, we can get a rough idea of the criterion about the selection rule

from the classical derivative. The incident electromagnetic wave induces the dipole moment of the molecule, which is given by:

$$P = \alpha E_0 \cos(\omega_0 t) \qquad \textbf{(2-32)}$$

where the α is polarizability; the $E_0 \cos(\omega_0 t)$ is the electric field of the incident wave.

The vibrational energy of a particular mode, from equation (2-13), is

$$E_n = \left(n + \frac{1}{2}\right)\eta\omega \qquad \textbf{(2-28)}$$

The displacement dX of the molecule can be expressed as

$$dX = X_0 \cos(\omega t) \qquad \textbf{(2-33)}$$

where the X_0 is the amplitude of the vibration.

For small displacement, the polarizability can be expressed by Taylor expansion and simplified as[27]:

$$\alpha = \alpha_0 + \frac{\partial \alpha}{\partial X} dX = \alpha_0 + \frac{\partial \alpha}{\partial X} X_0 \cos(\omega t) \qquad \textbf{(2-34)}$$

Thus, the induced dipole moment shown in equation (2-17) can be expressed as

$$P = \alpha_0 E_0 \cos(\omega_0 t) + \left(\frac{\partial \alpha}{\partial X}\frac{X_0 E_0}{2}\right)\{\cos[(\omega_0 - \omega)t] + \cos[(\omega_0 + \omega)t]\} \qquad \textbf{(2-35)}$$

There are two important results about Raman scattering implied in the equation. First, three distinct frequencies (i.e. ω_0, $\omega_0 - \omega$, $\omega_0 + \omega$) , which brings about three scattering frequencies in turn, are created by the external field: one is elastic scattering Rayleigh scattering; the others are inelastic scattering referred as Raman scattering including Stokes scattering, which has lower frequency, and anti-Stokes scattering,

which has higher frequency. Second, for the Raman scattering to happen, the $\frac{\partial \alpha}{\partial X}$ can not be zero, which is the selection rule for the Raman active mode. Generally speaking, for a vibrational mode to be Ramam active, the polarizability of the molecule must change during the vibration.

2.2.3 Surface Enhanced Raman Scattering(SERS) Effect

Surface enhanced Raman scattering was observed by Fleischman et al. in 1974 [28], and confirmed by Van Duyne, Jeanmarie and Albrecht, Creighton independently [29, 30]. It was found that when molecules were adsorbed on the roughed silver substrate, the Raman signals can be largely enhanced more than million times. Shortly afterward, it was proposed that the excitation of surface plasmon can explain this huge enhancement. Nowadays, the surface enhanced Raman spectroscopy had matured to become a powerful tool to detect the trace amount of molecules through the interaction of light, metal structure, and molecules. More importantly, it has also triggered the development of the near-field optics and other novel devices based on the plasmon.

The SERS effect is related to both electromagnetic [31, 32]and electronic mechanisms[33, 34]. In the electromagnetic theorem, field enhancement occurs due to the resonant effect between the optical fields and the surface plasmon in the metal leading to the redistribution of electric field intensities around the metal surface. Therefore, when the molecules are near or on the metal surface, the signals can be enormously enhanced. The enhancement depends on the type, size, shape, and arrangement of the metal particles and the frequency of the incident light. The SERS

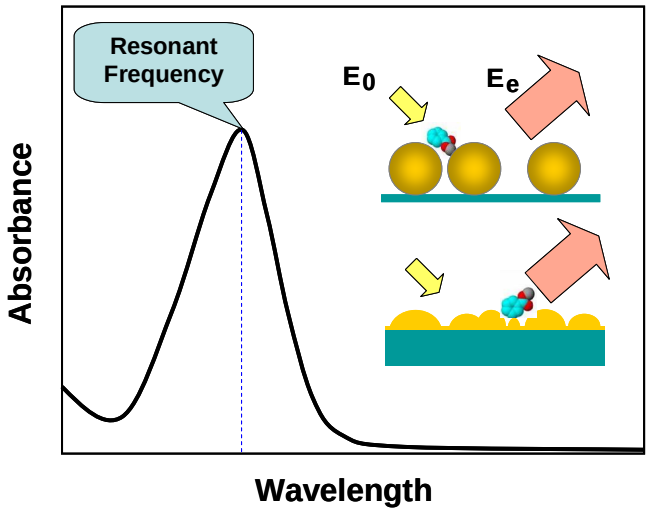

Figure 2-9 Electric field was enhanced on the metal surface in the surface plasmon resonant condition.

enhancement is extremely strong when both the incident and scattering fields are resonated with the plasmon frequency **(Figure 2-9)**. Normally, the frequency shift between the incident and scattering is very small compared with the width of plasmon resonance. Thus, the signal can reach about four power enhancement[35].

$$P_{SERS} \propto N.I_L.\left|A(\nu_L)\right|^2.\left|A(\nu_S)\right|^2.\sigma_{ads}^R \approx N.I_L.\left|A(\nu_L)\right|^4.\sigma_{ads}^R \qquad \textbf{(2-36)}$$

$A(\nu_L) = \dfrac{E_L}{E_0}$, (enhancement factor ; E_L : enhanced local field due to incident light)

$A(\nu_S) = \dfrac{E_S}{E_0}$, (enhancement factor ; E_S : enhanced local field due to scattering light)

In the electronic mechanism, the electronic coupling happened between the metal and molecules can change the polarizability of adsorbed molecules and produce a larger

cross section, increasing the Raman-scattering efficiency. However, the contribution in enhancement from the electronic mechanism is much smaller than from the electromagnetic mechanism.

2.2.4 Surface Enhanced Raman Scattering (SERS) Fiber Probe

Usually, the SERS measurement is carried out by directly dropping the analytic solution onto the metal surface substrate or mixing with colloidal metal nanoparticles using a conventional Raman scattering spectrometer, which is usually large for the need of optical alignment and Raman signal collection. Raman spectrometers with the optical fiber probes used for remote analysis are commercially available. However, the probes just collect the Raman signal scattered from the sample not that generated by SERS.

In the past few years a number of fiber-based SERS probes have been demonstrated [36-53]. Some of them use the two-fiber systems that separate the light source from the SERS-active probe[50, 51]. In that device, the signal is collected via the fiber but excited on the opposite side with an external light source. It is not convenient and is limited in some situation. Single optical fiber probes used for both excitation and collection signal have been reported to overcome the limitation. It becomes possible for the application in the real-time measurement to detect the molecules in solution, especially in the remote detection in the hazardous environment. Basically, they can be attributed to two major types of SERS-active probes, where the fiber with flat, angle, or tapered tip is directly covered with roughened metal film or metal island film[47, 49, 52], or covered by a layer of colloidal nanospheres with a thin metal layer on tops of them[48, 53]. Even though the Raman signal can be enhance by the rough metal surface,

the distribution of deposited metal shapes and size, which forms the hot spots, is not easy to control. The hollow core photonic crystal fibers have been reported to be applied in the probe to increase the SERS active areas[46, 54, 55]. In that devices, the analytic solution mixed with metal nanoparticles are filled into the hollow cores to get the enhanced Raman signal. Although the signal detected can be stronger due to the larger active areas, they also have the same problems and it is inconvenient to prepare the sample and probe for measurement.

In spite of the unique sensitivity, the application of SERS has not incorporated into the in situ analytical tool for real-time sensing commercially. One of major obstacles is the challenge of fabricating a stable and reproducible SERS-active substrate for use. Recently, a new method was reported to directly transfer the periodic array of pattern defined by E-beam lithography to the fiber tip[56, 57]. It becomes possible to tune the resonant frequency and control the density of hot spots to enhance the Raman signal by designing the pattern via E-beam lithography, but it is still inconvenient and time-consuming to produce the SERS-active probe by the E-beam lithography. Here, we propose a special design of the single optical fiber probe by fabricating periodic arrays of spherical voids embedded in metal films on the thin cover slide, which in turn is attached onto the cleaved fiber tip. The voids are embedded in the metal film to form the periodic arrays of hot spots, allowing getting the Raman signal uniformly. Furthermore, the void structure provides more energy confinement than the metal nanoparticles. The intensive fields exist up to 100 nm above the metal surface due to the

large void structure, which increase the volume of SERS-active zone dramatically, and therefore, these nanostructures are particularly suitable for fiber-based sensor.

CHAPTER 3

SELF-ASSEMBLY OF POLYSTYRENE NANOSPHERES

The self-assembly of the two polystyrene nanosphere patterns, dispersed mono-layer and periodic multi-/mono- layer structure, are described. The mechanisms related to each method are also discussed.

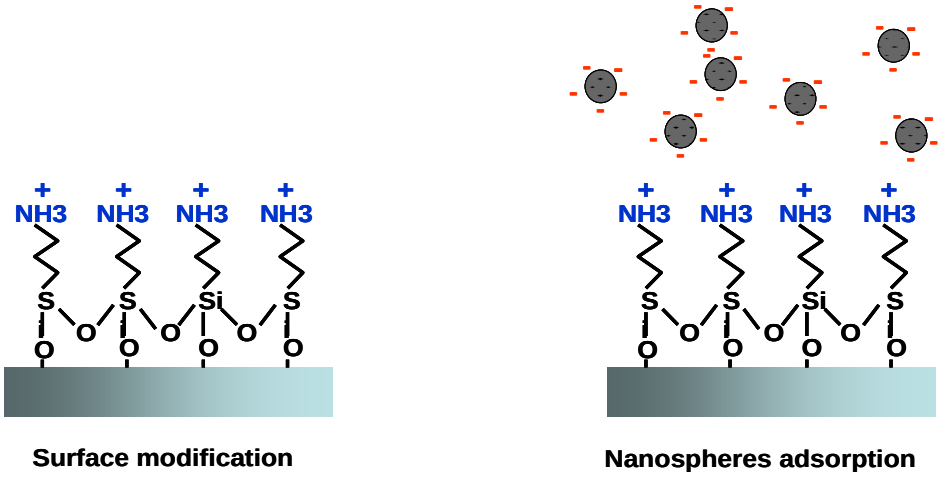

Figure 3-1 Illustration of the fabrication process for the dispersed mono-layer nanosphere structure, which involves two steps: substrate modification by APTES and adsorption process.

3.1 Dispersed Mono-layer Polystyrene Nanospheres

The fabrication process for the dispersed mono-layer nanosphere structure involves two steps: (1) substrate surface modification. (2) adsorption process. The (3-aminopropyl)triethoxysilane (APTES, C2H5O)3-Si-(CH2)3-NH2) with positively

charged amino group was used to form self-assembled monolayer (SAM) on the Si or SiO2 substrate. Then, polystyrene nanospheres with negatively charged carboxyl group were adsorbed onto the substrate surface from the colloidal solution by electrostatic interactions **(as shown in the Figure 3-1)**.

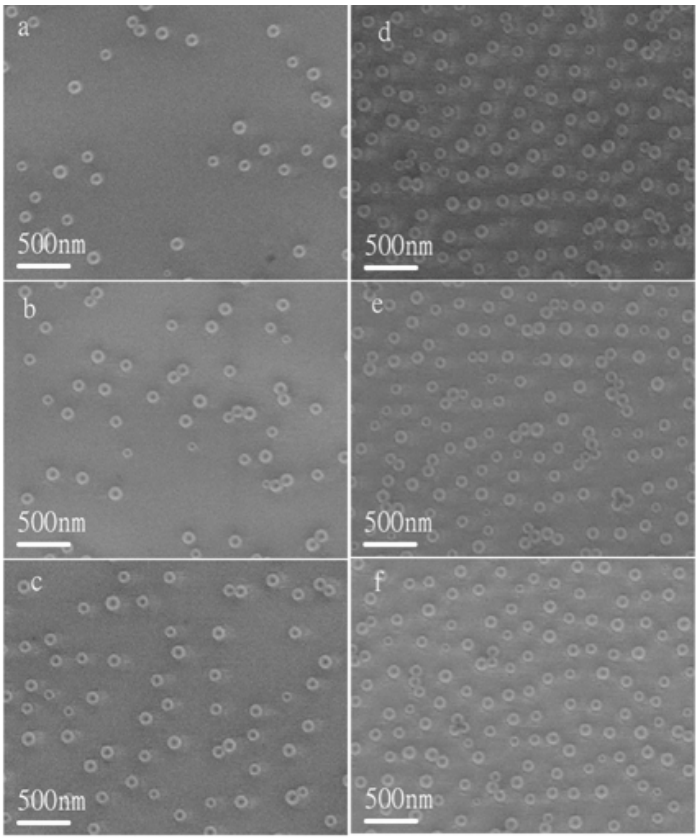

Figure 3-2 SEM images show the surface coverages related with the dipping time for different colloidal concentrations. (a) 0.007% for 5 min. (b) 0.007% for 10 min. (c) 0.007% for 20 min. (d) 0.015% for 5 min. (e) 0.015% for 10 min. (f) 0.015% for 20 min.

The detail procedure is described below. First, The Si wafer with a SiO2 epilayer was cleaned with acetone followed by rinsing with IPA and DI water. Then, the substrate was dipped into 0.5 mM APTES in chloroform for 40 minutes, followed by

rinsing with IPA and blow-drying with N2 gas, resulting in the formation of the self-assembled monolayer(SAM) with positive charges on the surface. Finally, the wafer was immersed into the colloidal polystyrene nanoparticle solution which was diluted with DI water (1:200 by volume) for 10 minutes, followed by rinsing with methanol and blow-drying with N2 gas. The polystyrene nanospheres with negative charges on the surface were adsorbed onto the substrate with positive charges forming a dispersed mono-layer polystyrene nanaospheres with uniform distance between them due to the electrostatic attraction between particle-substrate and electrostatic repulsion between particles. The different concentration of colloidal solution under various dipping time were investigated. **Figure 3-2** shows the SEM pictures for each condition. Surface coverage calculated by the image software was plotted with dipping time in **Figure 3-3**. The detailed results were shown in **Table 3-1**. The maximum surface coverage is about 0.22 for three different concentrations (0.007%, 0.015%, 0.03%).

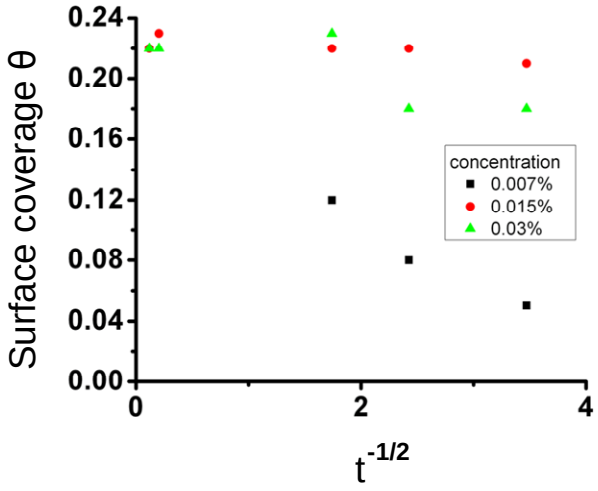

Figure 3-3 Adsorption kinetics were measured at different concentrations of polystyrene colloidal solution and shown in the coordinate system surface coverage θ vs $t^{-1/2}$.

Table 3-1 Surface coverage of different concentrations of polystyrene colloidal solutions (0.007%, 0.015%, and 0.03%) with various dipping times

	0.007%	0.015%	0.030%
5 min	0.06	0.21	0.18
10 min	0.07	0.22	0.18
20 min	0.10	0.22	0.23
24 h	0.21	0.23	0.22
72 h	0.22	0.22	0.22

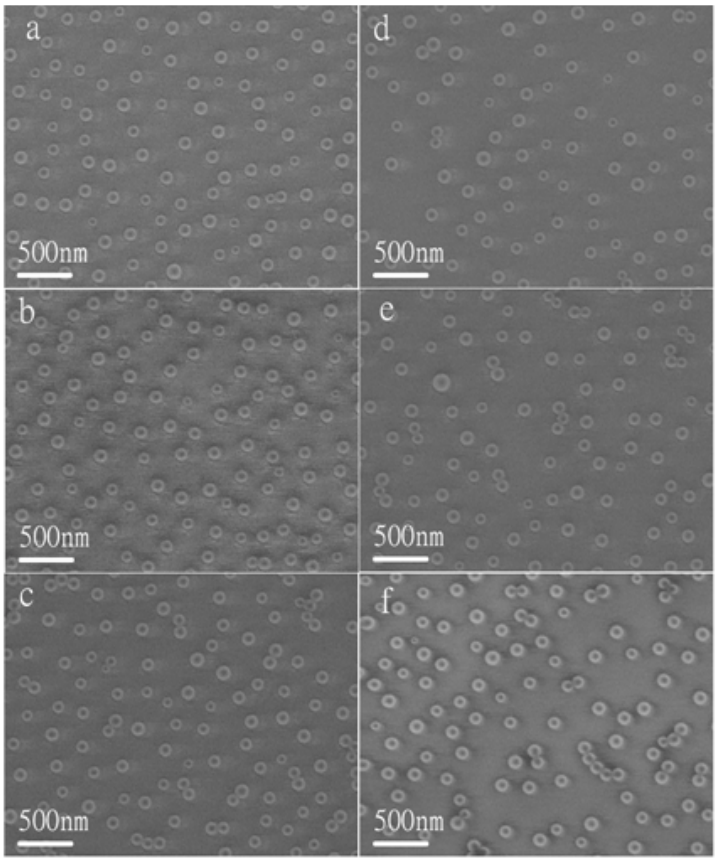

Figure 3-4 SEM images show the surface coverages related with the dipping time under various temperature (5℃ and 50 ℃) for the 0015% polystyrene colloidal solution. (a) 5 ℃ for 5 min. (b) 5℃ for 10 min. (c) 5℃ for 20 min. (d) 50 ℃ for 5 min. (e) 50 ℃ for 10 min. (f) 50 ℃ for 20 min.

The phenomenon can be described by the random sequential adsorption model (RSA). In the classical RSA model for the monodispersed non-interactional spherical particles, the surface coverage θ approaches asymptotically the jamming limit (0.547) according to the power law relationship:

$$\theta(\infty) - \theta(t) \sim t^{-1/2} \qquad \textbf{(3-1)}$$

In this experiment, there are some conditions deviated from the assumptions in the classical RSA model. First, the polystyrene nanospheres are not non-interactional particles. They carry the negative charge on the surface leading to the strong electrostatic repulsive interaction between them. Second, there are some electrolyte existed in the solution. Therefore, the double-layer interaction energy described in the DLVO theory had to be taken into account. In a low ionic concentration solution, the Debye screening effect is minimal and the repulsions dramatically limit the extent of the adsorption onto the surface. At a higher ionic strength, the repulsive force is weakened by the screening effect. Thus, the higher surface coverage is reached. When the Debye length is very small comparing to the nanoparticle size, the situation is similar to the non-interaction nanoparticles among the solution, and the maximum surface coverage about 0.547 can be attained. The extended RSA model was developed to account for this phenomenon[58]. In this model, the effective hard sphere radius was used and the maximum coverage can be got by:

$$\theta_{\max} = \theta_{\infty} (a / a_{eff})^2 . \qquad \textbf{(3-2)}$$

As shown in the Figure 3-3, there exists a nearly linear relationship of coverage with time when using the solution with a concentration of 0.007%. Thus, the system exhibits the RSA-like kinetics. By extrapolating the line to infinite time, the saturation coverage of about 0.22 can be estimated. For higher colloidal concentration solutions, the saturation condition had been reached in the time scale of minutes. The tests for 0.015% concentration of solution under the various temperatures (5℃ and 50℃) for different time were also performed to see the surface coverage. The surface coverage about 0.22, as shown in **Figure 3-4,** has been observed which is similar to the result obtained at room temperature.

The advantage of this method is the saturation coverage or distance between particles can be controlled by adjusting the pH value of the colloidal solution, ion concentration, surface charges of the particles and substrate, parameters that can affect the double-layer interaction energy.

3.2 Periodic Multi-layer and mono-layer Polystyrene Nanospheres

Two different techniques, horizontal and vertical deposition by slow dvaporation have been developed to create the multi- and mono-layer periodical structures.

3.2.1 Horizontal Deposition

Multi-layer structures

We use slow evaporation in a physical confinement to deposit nanospheres to a Au-coated substrate. The physical confinement is composed of a Viton o-ring (1.2 cm diameter), a Teflon washer (0.9 cm I.D., 2 cm O.D.), and the Au coated substrate which

was made by deposition of a thin layer of 5 nm Cr as adhesive film and 10 nm Au as conductive layer (for electrodeposition) on a glass cover slip by the E-beam evaporation **(Figure 3-5 (a))**.

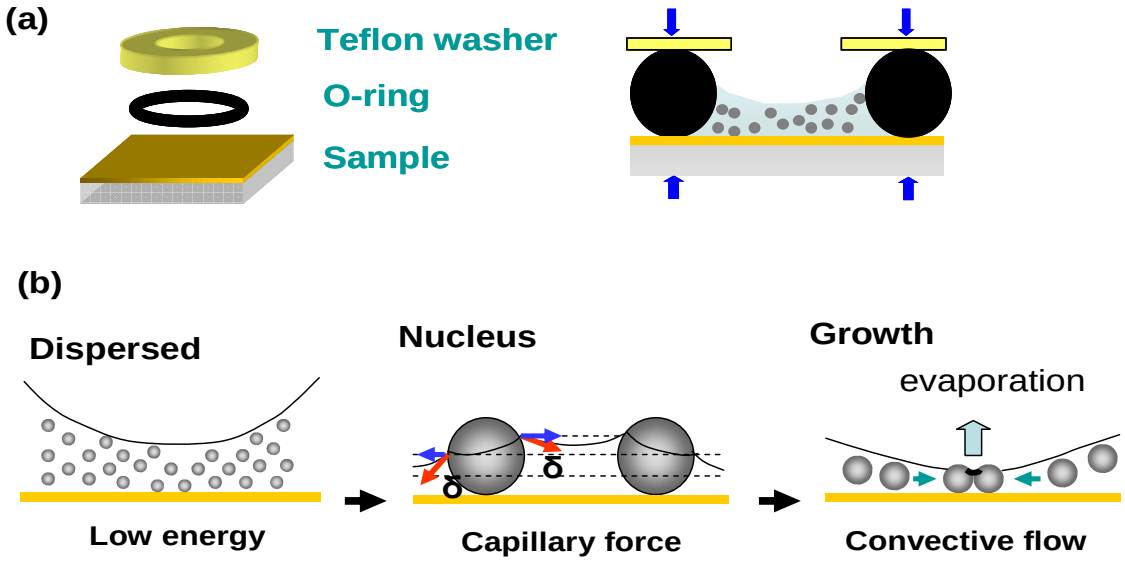

Figure 3-5 (a) Sketch of experiment set-up. (b) Sketch of the process and mechanism to form the 3-D close- packed pattern.

The polystyrene sphere colloid solution diluted with DI water by 1:5 volume ratio was prepared. Then, the colloid was injected into the cell. After that, the cells were put into the humidity chamber. By controlling the evaporation rate of the colloid through tuning the humidity of the chamber, the close- packed pattern with various polystyrene size of 50nm, 100nm, 200nm, 500nm, 750nm had been fabricated **(Figure 3-6)**.

In resulted structures, most of the crystal are FCC structures, but small portion of BCC structure enclosed by the fcc structures and random array of nanospheres near the edge of the disk shape pattern were also found.

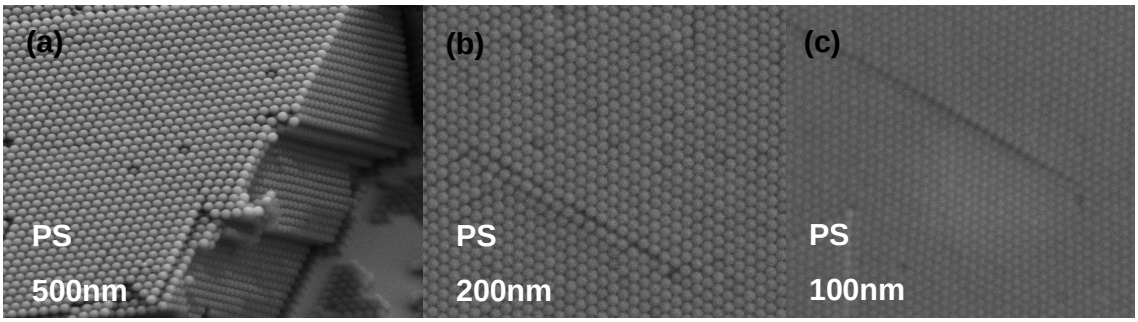

Figure 3-6 Closed- packed multi-layer templates of polystyrene nanospheres with various diameters.((a) 500 nm, (b) 200 nm, (c) 100 nm.)

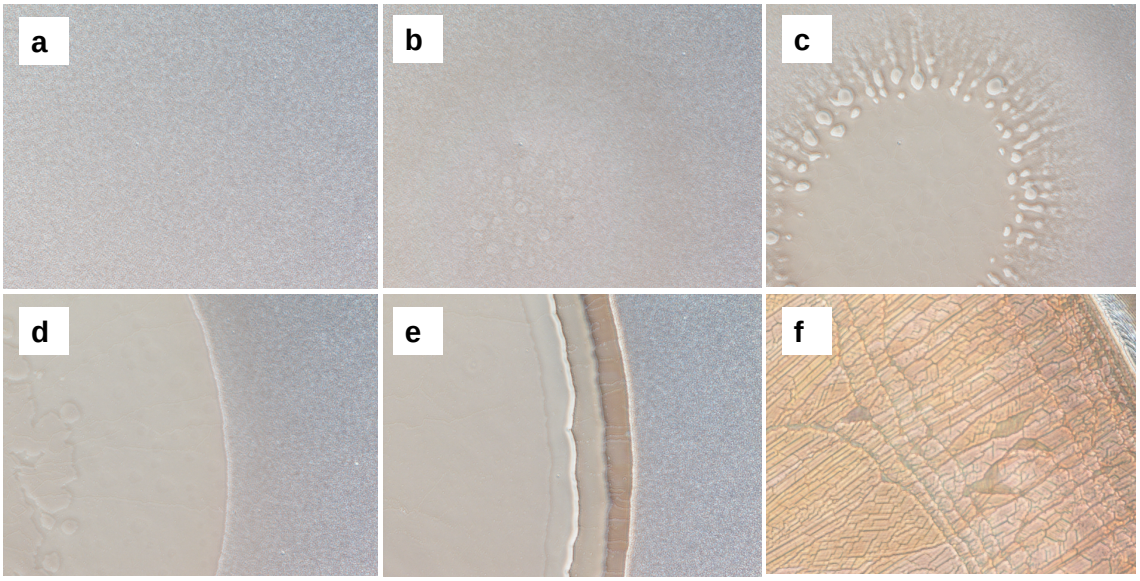

Figure 3-7 Pictures show the drying process. (a) Particles move in the Brownian motion. (b) Nucleation happens when the liquid layer decreases to a critical thickness due to evaporation. (c) Liquid carrying with nanospheres flow toward the center. (d) Ordered monolayer of nanospheres started to form. (e) Multi-layer structures with different layers appeared, which can be identified from the color difference. (f) Multi-layer structure after completely drying.

To study the formation mechanism of the multi-layer structure, an inverted microscope with transmitted polychromatic light on the top side and objective lens on the bottom side was used to observe the drying process. The pictures took at different

time during the formation process are shown in the **Figure 3-7**. At the beginning, the polystyrene nanospheres moved as Brownian motion, which can be estimated from the dark points resulted from the scattering of light by the particles. When the liquid layer decrease to a critical thickness due to water evaporation, nucleation happened in the center, followed by rapid movement of liquid flow toward the center. The ordered monolayer of nanospheres started to form by the continuous movement of the nanospheres toward the center. After a short time, the multi-layer structure appeared. The process continued until water dried up and finally the multi-layer pattern was formed on the whole substrate inside the cell.

A mechanism based on the 2-D crystal formation and 3-D repulsive force model has been used to explain the observed phenomenon [59-62] **(Figure 3-5 (b))**. In the beginning, the colloid drop on the substrate forms the concave shape within the confinement and the polystyrene spheres tend to self-organize to the ordered structure in the solution because of the double-layer interaction between the particles. When the thickness of water layer becomes approximately equal to the particle diameter, the deformation of the liquid-gas interface gives rise to strong interparticle capillary forces and triggers the nucleation of the crystal. Then, the crystal growth is caused by a convective transport of the particles towards the ordered nucleus. Due to the hydrophilicity of particles, the further thinning of the concave meniscus water layer between the particles in the nucleus is hindered, and result in the hydrodynamic pressure of the water which carries the particles toward the nucleus. Finally, the close packed pattern forms.

The mono-layer structure, theoretically, can be formed by controlling the angle θ, either by increasing the evaporation rate or decreasing the suspension volume. But in reality, it is difficult to get the mono-layer structure on the whole substrate. One of the main reasons is hydrophobic nature of the gold layer on the substrate. Most results reported on the mono-layer formation by the similar methods were performed on the hydrophilic surfaces like glass or mica. The small amount of suspension can easily be spread onto the hydrophilic surfaces but not on the hydrophobic surfaces. Therefore, the surface has to be modified to get the mono-layer structure. Another reason is that the angle θ gradually increase during the drying process, leading to the multi-layer structure surrounding the mono-layer structure. In this study, we used a simple method to get the mono-layer pattern on Au-coated substrate (hydrophobic).

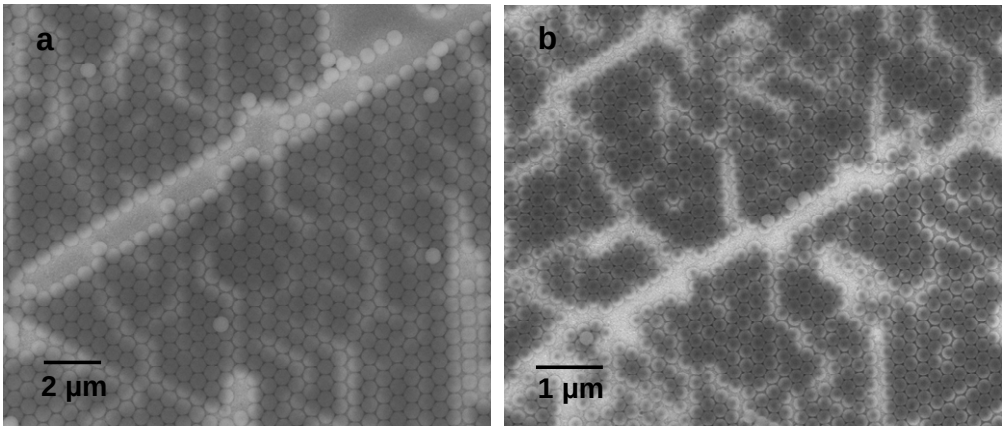

Figure 3-8 SEM pictures show the mono-layer structures on the gold coated substrate. (a) 500 nm of polystyrene nanospheres. (b) 200 nm of polystyrene nanospheres.

Mono-layer structures

We found that the mono-layer patterns can be made by simply rinsing the multi-layer structures with the methanol. After rinsing, the upper layers of nanospheres were

removed leaving the bottom layer on the substrate as the mono-layer structure. It has also been found that using this method the mono-layer structure can only be formed on the metal surface especially on the gold surface, not on hydrophilic surfaces such as Si and glass. When the multi-layer structure created on the Si or glass surface was rinsed, all the layers were removed. Using this simple method, the ordered mono-layer structure, as shown in the **Figure 3-8**, with the nanosphere sizes between 200 nm and 750 nm has been created on the Au-coated substrates.

The following mechanism is proposed to qualitatively explain this finding, which is based on the interaction energies between two identical media (nanospheres) and between two different media (nanosphere-substrate). Because the polystyrene nanospheres carry the negative charge on the surfaces, they can induce the surface charge on the conductive surface, creating the Coulombic attraction energy between the nanospheres and substrate. Roughly speaking, the interaction energy can be described as:

$$w(r) = \frac{B}{r} - \frac{C}{r^6} \qquad \textbf{(3-3)}$$

where r is the distance. The first term is attributed to the electrostatic interaction and the second term is due to the van der Waals interaction energy. In a very short distance, the energy is dominated by the van der Waals interaction energy. To simplify, we assume the system in the dry condition is in the vacuum environment. In this situation, the adhesion force of two rigid macroscopic spheres, according to the Derjaguin approximation, can be described as[4]:

$$F = 2\pi\left(\frac{R_1 R_2}{R_1 + R_2}\right)W_{12} \qquad \textbf{(3-4)}$$

where R_1, R_2 represent the radii of the spheres. In the two identical spheres system, the $R_1 = R_2$; in the sphere-flat plane system, $R_2 = \infty$. W_{12} is related to the van der Waals interaction energy. As introduced in the previous section, the van der Waals interaction energy for two like spheres and sphere-surface in contact can be described as:

For two same spheres: $$W = \frac{-A_{11}R}{12\sigma} \qquad \textbf{(3-5)}$$

For sphere-surface: $$W = \frac{-A_{12}R}{6\sigma} \qquad \textbf{(3-6)}$$

where σ is the contact distance and A_{11} represent the Hamaker constant for same material andA_{12} represent the Hamaker constant for different material. According to the combing relation, we can obtain the approximate values of unknown Hamaker constants in terms of known ones by the equation:

$$A_{12} \approx \sqrt{A_{11}A_{22}} \qquad \textbf{(3-7)}$$

Therefore, we can approximately estimate the adhesion forces between the two-like spheres and sphere-surface systems simply by comparing the Hamaker constants of them. The Hamaker constant for polystyrene is about 7.9×10^{-20} J and for gold is about 40×10^{-20} J. The Hamaker constant for polystyrene-gold J can be obtained from equation (3-7), which is about 17.8×10^{-20} J. It shows a stronger adhesion energy between polystyrene sphere and gold surface than that between polystyrene spheres, leading to the mono-layer spheres stick to the substrate.

Accordingly to this mechanism, the mono-layer structure can form on the substrate where the Hamaker constant is higher than that of the polystyrene sphere. We tried to make it on different metal surface like Cr, the Hamaker constant is about 36×10^{-20}. We found the mono-layer structure can also be formed on Cr substrate. But the ordering of the spheres is not as good as that on the gold surface. This may be due to the oxidation of Cr formed on the Cr surface in the environment reducing the Hamaker constant value so that some polystyrene nanospheres peel off from the substrate **(Figure 3-9)**.

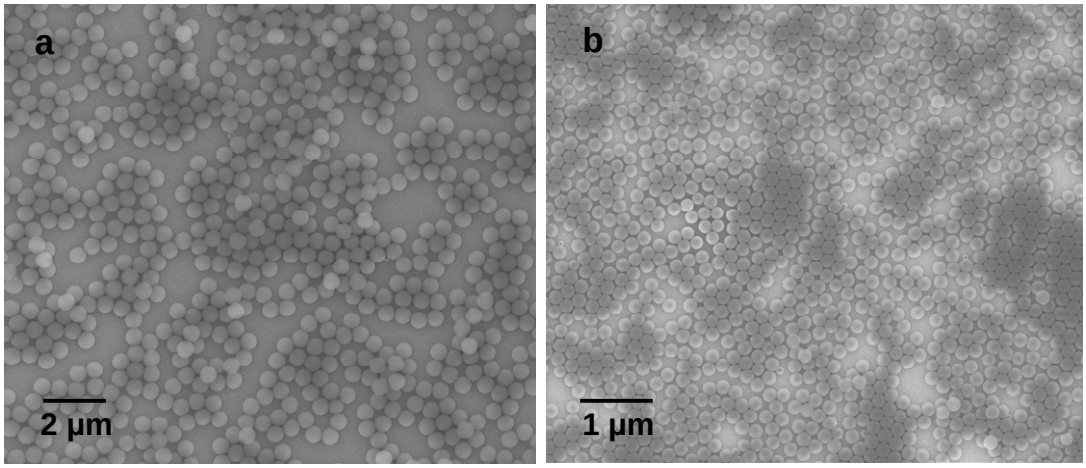

Figure 3-9 SEM pictures show the mono-layer structures on the chromium coated substrate. (a) 500 nm of polystyrene nanospheres. (b) 200 nm of polystyrene nanospheres.

Strictly speaking, the adsorbed layer, such as molecules on the polystyrene nanospheres, dominate the van der Waals interaction energy between spheres and substrate in the short distance. Therefore, the Hamaker constant of $A_{molecule\text{-}molecule}$ and $A_{gold\text{-}molecule}$ instead of $A_{polystyrene\text{-}polystyrene}$ and $A_{polystyrene\ gold}$ have to be considered in the

system. But the Hamaker constants for organic molecules have similar values as polystyrene and are much less than the gold. Thus, this effects can largely be neglected..

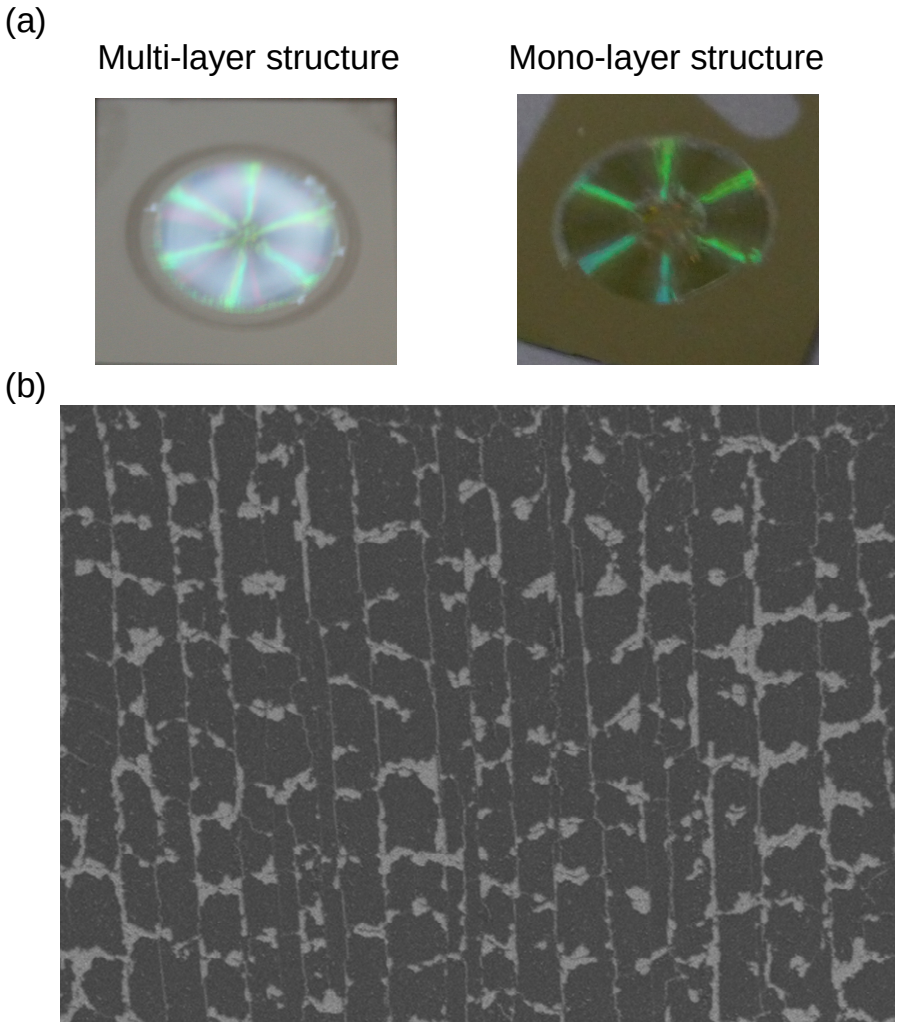

Figure 3-10 (a) Pictures show the six lights in the radial shape emitting from the samples. (b) SEM picture of 500 nm mono-layer structure.

In the mono and multilayer structures with the particle sizes between 350 to 750 nm, the visible iridescent color was observed due to the Bragg diffraction from periodic arrays of the nanospheres. The interesting thing is only six lights with the same color emitting radially were observed for all the samples (as shown in the **Figure 3-10 (a))**.

From the SEM picture **(Figure 3-10(b))**, it can be seen that there exist many stripes, composed of radially arranged ordered array of nanospheres, separated by white lines.

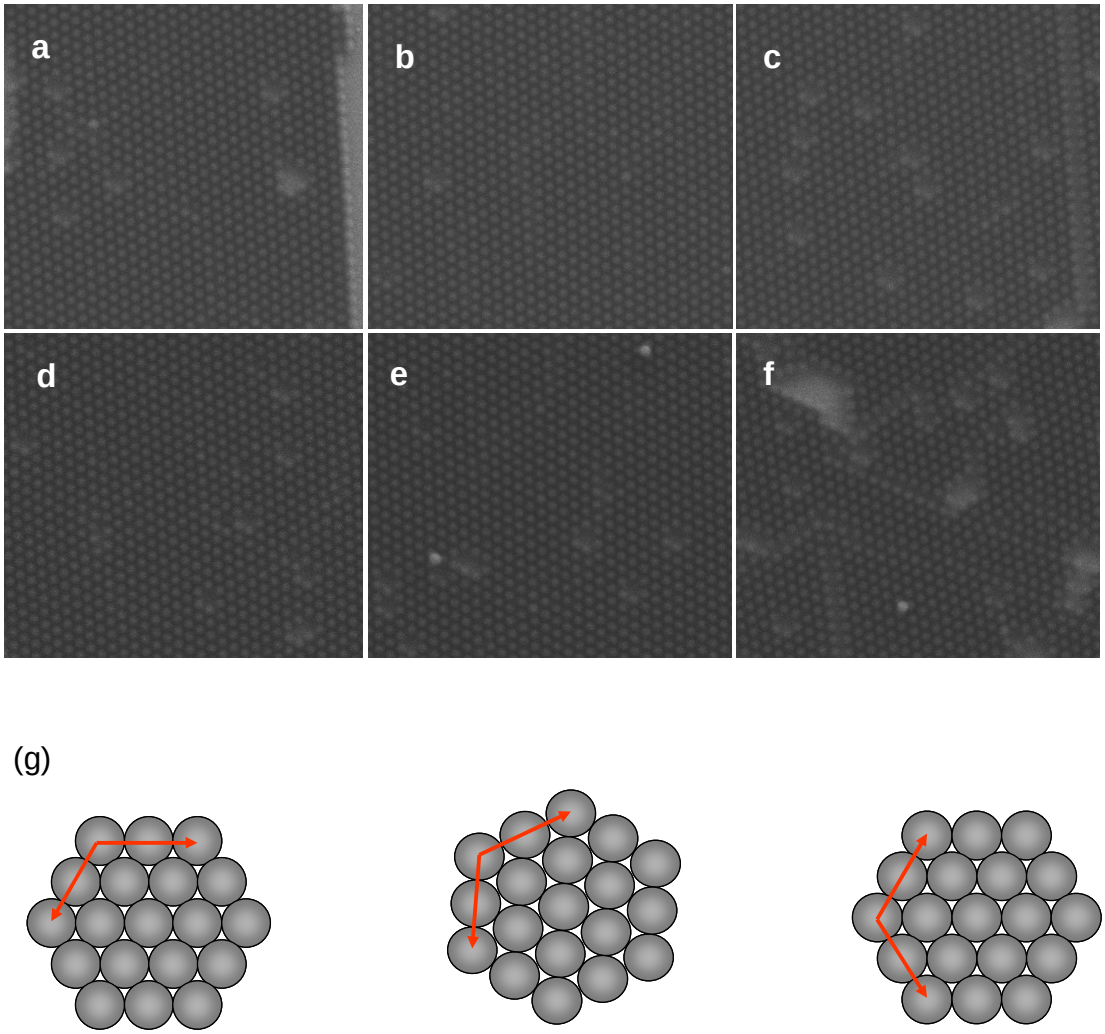

Figure 3-11 (a)~(c) SEM pictures of 500 nm polystyrene nanosphere crystalline structures, which were took with the interval 1 mm along one stripe as shown in Figure3-10. (d)~(f) SEM pictures which were took with the interval 1 mm along another stripe after rotating 60 degree. (g) Illustrations show the orientation of the closed-packed structure with 0, 30, 60 degree rotation angles.

The SEM pictures, **shown in the Figure 3-11(a)~(c)**, were taken every 1 mm along one stripe and found all the closed packed patterns are in the same orientation.

Then, we rotated the sample for 60 degrees **(Figure 3-11(d)~(f))**. Pictures show the same orientation with the previous ones. Therefore, **as shown in the Figure 3-11(g)**, the six lights existed in samples may be resulted from the closed packed structure of the nanospheres. Every 60 degrees, the patterns display the same orientation and show the same color of light.

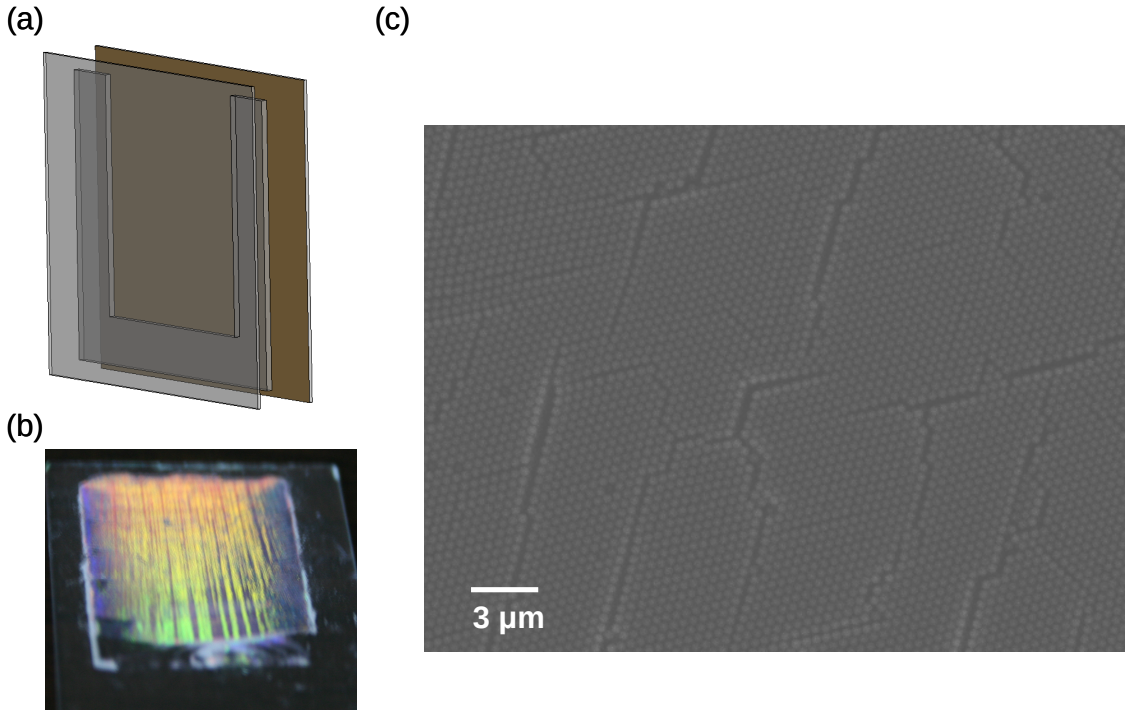

Figure 3-12 (a) Illustration of the set-up for the vertical deposition. The U shape of PDMS film was used as buffer layer between the glass slide and the gold-coated glass slide. (b) Picture shows the color light with the same direction. (c) SEM picture shows the orientation of the closed packed structure.

3.2.2 Vertical Deposition

Flat Substrate

The patterns formed by the horizontal evaporation technique have multi-orientations along the circumference, which is due to the circular shape of the contact

line between solution drop and the substrate. This phenomenon intrigues us to fabricate the single-orientation of structure by simply controlling the shape of the contact line. With this regard, the vertical deposition technique with parallel straight contact line was developed to produce the patterns with single orientation. The set-up for this approach is shown in **Figure 3-12(a)**, the U shape of PDMS film about 2 mm thick was used as spacing layer between the Au-coated substrate and the glass slide. The diluted polystyrene solution was poured into the chamber enclosed by the substrates and PDMS film and then the whole set-up was placed into the humidity chamber for slow evaporation. After drying, the multi-layer structures were formed only on the glass slide. Unlike the pattern created by horizontal deposition which has six lights emanating in the radial shape, these samples showed the light with the same direction **(Figure 3-12(b))**. Checked by SEM, the orientation of the structure was almost toward the same direction **(Figure 3-12(c))**.

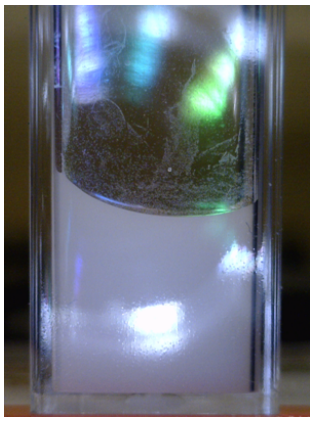

Figure 3-13 Contact angles of polystyrene solution on the glass surface (left side) and on the gold surface (right side).

(a)

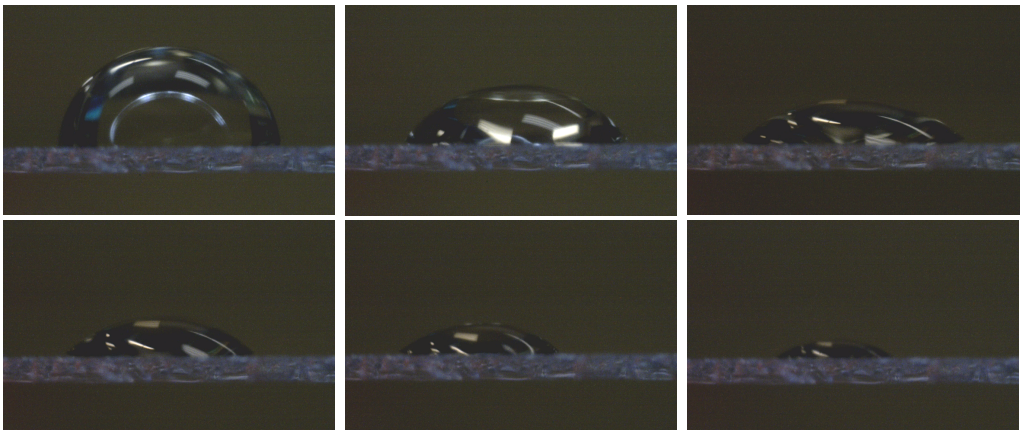

(b)

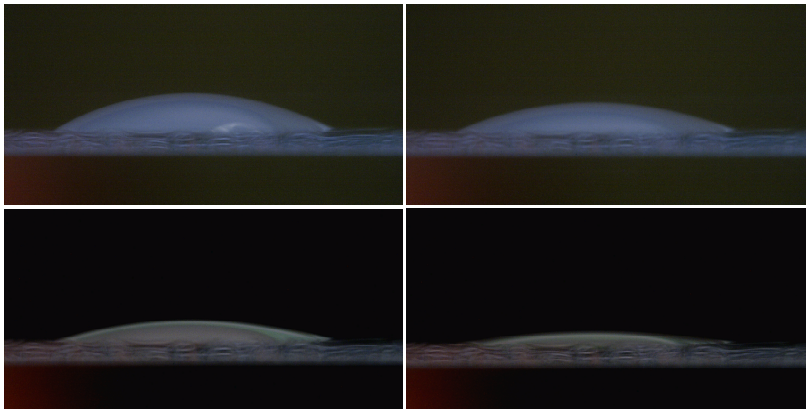

(c)

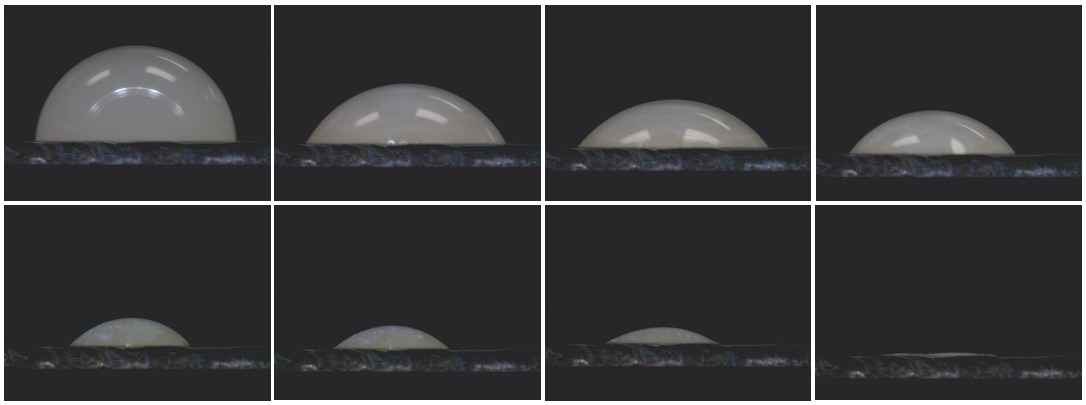

Figure 3-14 Pictures of drying process on different surface. (a) 2 μl of DI water was dropped on the gold-coated substrate as reference. (b) 2 μl of diluted polystyrene solution was dropped on the glass slide (b) 2 μl of diluted polystyrene solution was dropped on the gold-coated substrate.

To directly view the drying process, a cuvette with the glass stripe inserted on the left side and the substrate with gold layer on the right side was used to simulate the similar condition as the cell. The contact angles, from the **Figure 3-13**, on the two surfaces are quite different. The contact angle formed between glass and the polystyrene solution is much sharper than that on the Au-coated substrate side. This is due to the hydrophobic characteristic of gold. To analyze the relationship of the contact angle with the formation of the multi-layer patterens, the diluted polystyrene solution, as well as deionized water as reference, was dropped onto the glass slide and Au-coated substrate respectively and the pictures were taken by the camera sequentially during the drying process. As shown in the **Figure 3-14**, the water drop started to shrink after reaching a critical contact angle on both of the surfaces and finally disappeared through the evaporation. For the polystyrene solution dropped on the glass slide, the drop almost stuck on the original position leaving the stain after drying; while the polystyrene solution dropped on the Au-coated substrate shrank after a critical angle, and then stuck on the substrate until drying. These experiments confirmed the observation and explanation made by other groups that the presence of particles near the drop edge facilitates the pinning of the contact line[63]. Since the evaporation rate is highest at the edge, the liquid with particles must flow outward toward the edge of the drop to compensate the liquid on the edge due to the pinning effect, resulting in the ring pattern after drying. To understand more about this phenomenon, the microscopy with video camera was used to record the drying process. The nanospheres accumulated on the edge and pinned on both glass and gold substrate in the early stage. Then, the settled

nanospheres on the gold substrate started to move toward the center for a few second and stopped again **(shown in the Figure 3-15)**. This happened for a few times and the jet-like protrusions were observed emanating from the drop edge. Finally, a fractal-like stain was left on the gold substrate when the evaporation was complete. On the glass surface, the settled nanospheres also moved slowly on some area of the edge, but the duration of the moving was much shorter. As a result, the smooth, near-circular shape of stain was left on the glass slide.

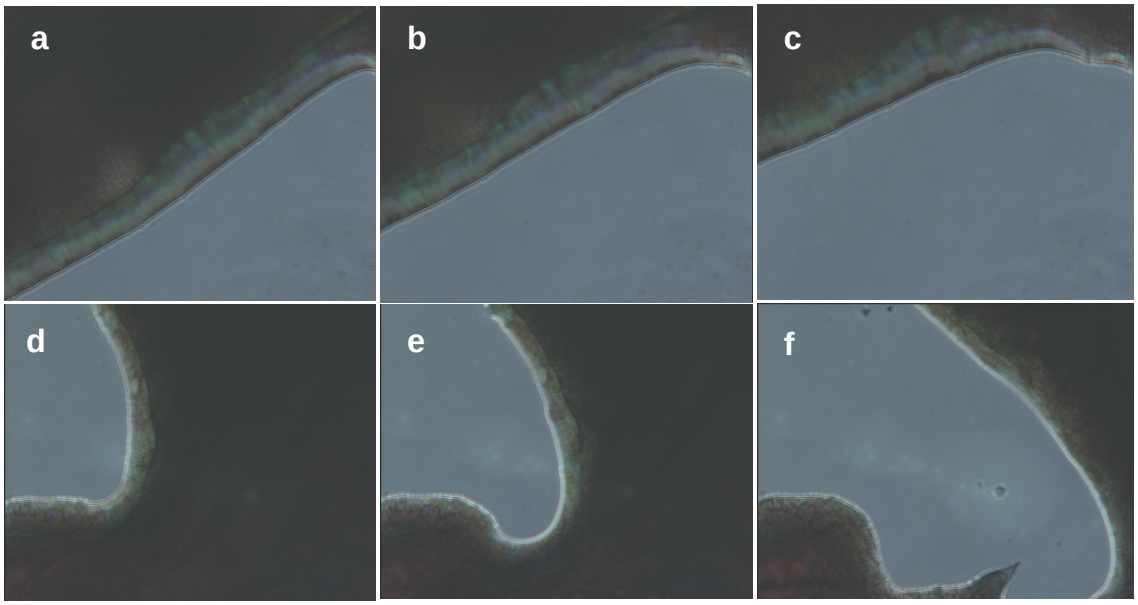

Figure 3-15 Images of drying process of 2 μl diluted polystyrene solution on the gold-coated substrate observed with a microscopy, (a)~(c) shrinking of the diluted polystyrene solution drop happened. (d)~(f) shrinking of the diluted polystyrene solution drop happened (pictures were taken from different area).

These observations can be explained in terms of the contact angle hysteresis[4] (**as shown in the Figure 3-16**), where the advancing contact angle θ_A, analog to contact angle of the drop in the beginning, is larger than the contact angle θ_R, analog

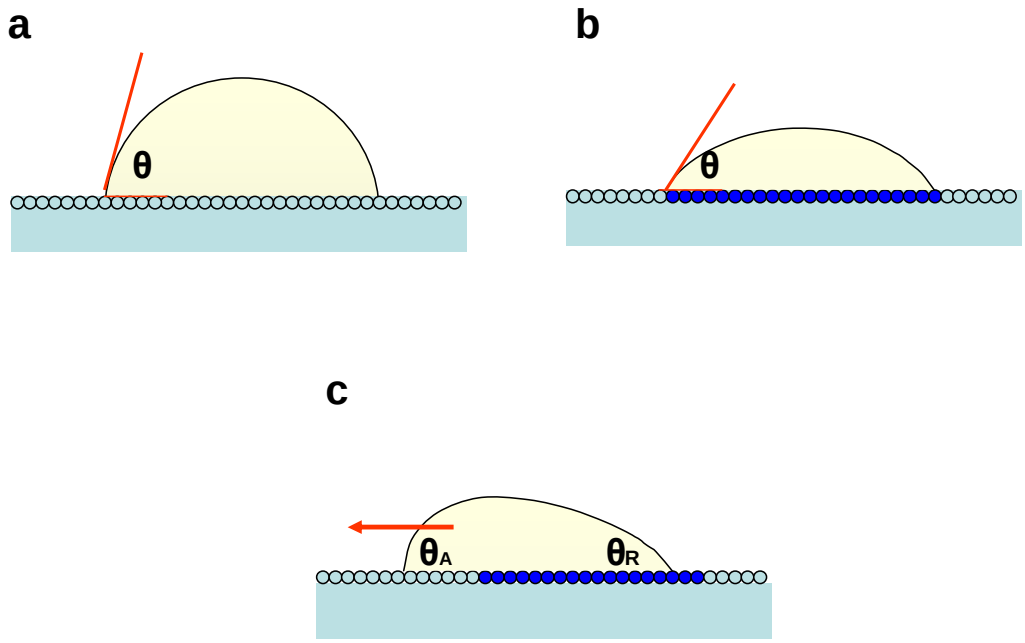

Figure 3-16 (a) Contact angle of one drop in the beginning. (b) Contact angle of one drop changes due to the molecular rearrangement on the interface of solution and substrate. (c) Contact angle hysteresis: advancing contact angle θ_A is larger than the receding contact angle θ_B.

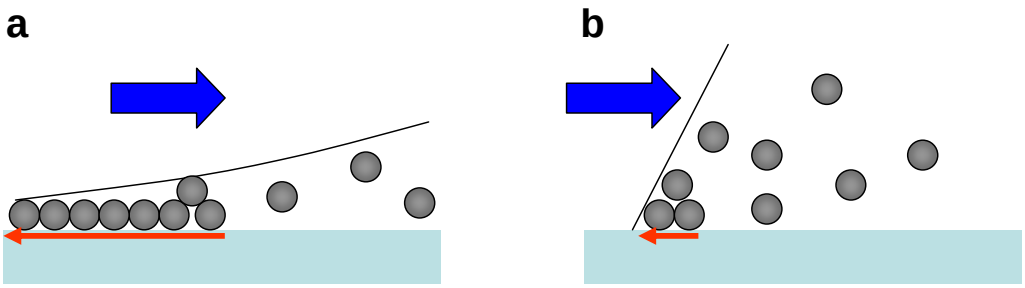

Figure 3-17 (a) Illustration of colloid on the hydrophilic surface. When the contact angle reach to the critical value, the pulling force (blue wide arrow) is induced to retain the critical angle. The sticking force in the hydrophilic surface is strong due to the larger number of settled nanospheres and high effective friction force (red arrow) inserted by the liquid meniscus to repel the pulling force. (b) The sticking force in the hydrophobic surface is weak due to the small number of settled nanospheres and low effective friction force (red arrow) inserted by the liquid meniscus to repel the pulling force.

to contact angle of the drop before moving. When the contact angle is less than the θ_R, the drop shrinks to retain the value of the angle. Thus, the induced force exerts on the settled nanospheres. In the hydrophilic surface, the sticking force is strong, which is due to the larger number of settled nanospheres resulted from high deposition rate on the sharp edge and high effective friction force exerted by the liquid meniscus **(Figure 3-17)**. Thus, the nanospheres can fix on the hydrophilic substrate but not on the hydrophobic one. It can be seen that the contact angle is a key parameter for the pattern formation. Even though we demonstrated this mechanism using a horizontal deposition way, the result is also applicable to the vertical deposition part.

On patterned substrates

From the above-mentioned mechanism, it is known that a sharp contact angle is required to deposit nanospheres on a substrate. In order to deposit nanospheres on Au-coated substrate with a broad contact angle (which is necessary for electrodeposition), we design a photolithographically patterned substrate. The idea is to deposit hydrophilic material like SiO2 on part of the hydrophobic substrate (Au-coated substrate) to decrease the contact angle between the solution and the substrate. The detail procedure is described below. First, the masks, which are composed of the square arrays 100 μm apart with various side lengths 30, 50, 70 μm, respectively, were purchased CAD/Art Services, Inc.. Second, the positive resist 5214 was coated on the Au-coated substrate by the spin coater 4500 rpm for 30 sec, followed by a soft-bake process under 105℃ for 1 min. Then, the sample was exposed to the UV light for 30 sec and developed for 2 min to form pattern in photoresist. Finally, about 50 nm SiO2 was deposited onto the

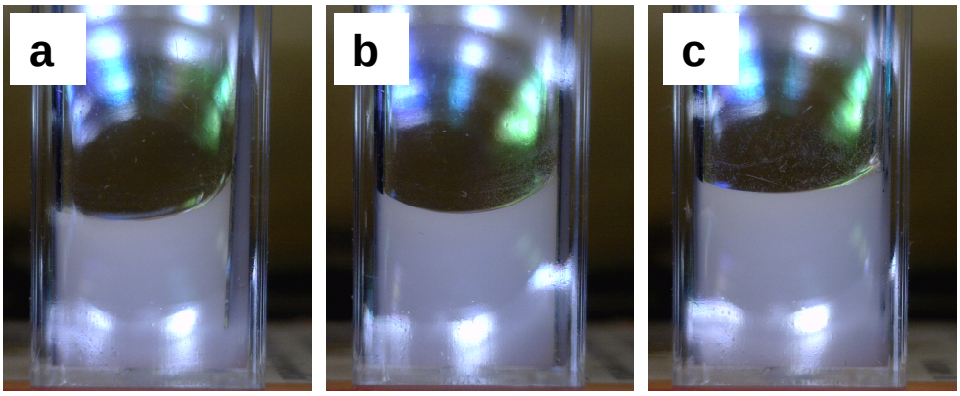

Figure 3-18 Contact angles of diluted polystyrene solution on different surfaces. (a)Au surface (left side); pattern structure which is composed of square arrays of gold pads separated by 100 μm with various side lengths 30 μm (right side). (b) 50 μm. (c) μm.

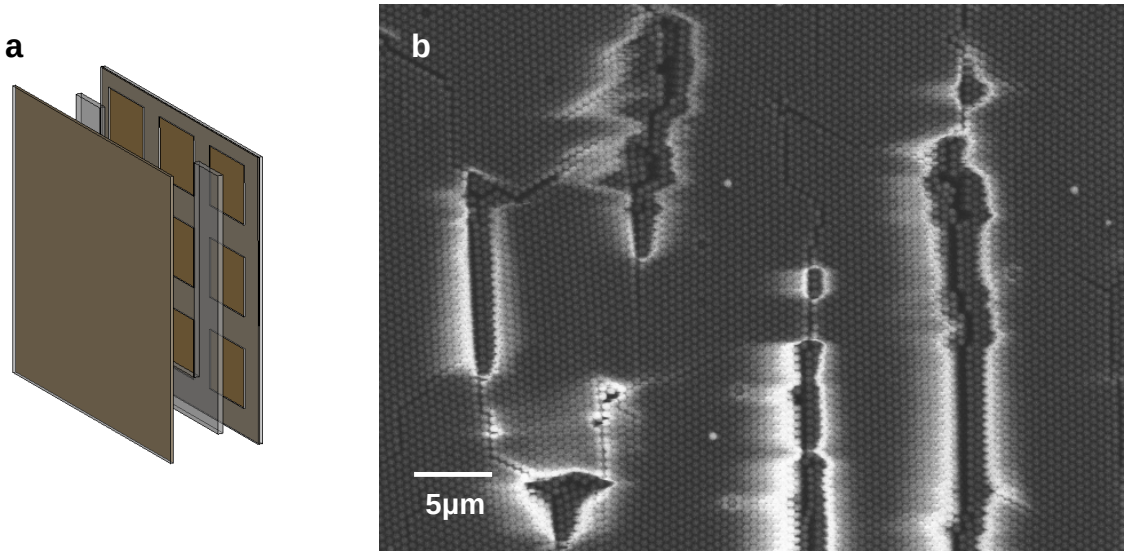

Figure 3-19 (a) Illustration of set-up for the vertical deposition technique. (b) Multi-layer structure was formed on the pattern surface.

substrate using an E-beam evaporator, followed by a lift-off process using acetone in ultrasonic bath for 15 sec to remove the photoresist. The pattern with the square gold pads surrounded by SiO2 film was produced on the substrate. To compare the contact angle, we inserted a pattern substrates and a gold-coated substrates into a cuvette filled

with diluted polystyrene solution. As shown in the **Figure 3-18**, the contact angles are reduced in all patterned substrates and the substrate with the highest ratio of SiO2 shows the sharpest contact angle.

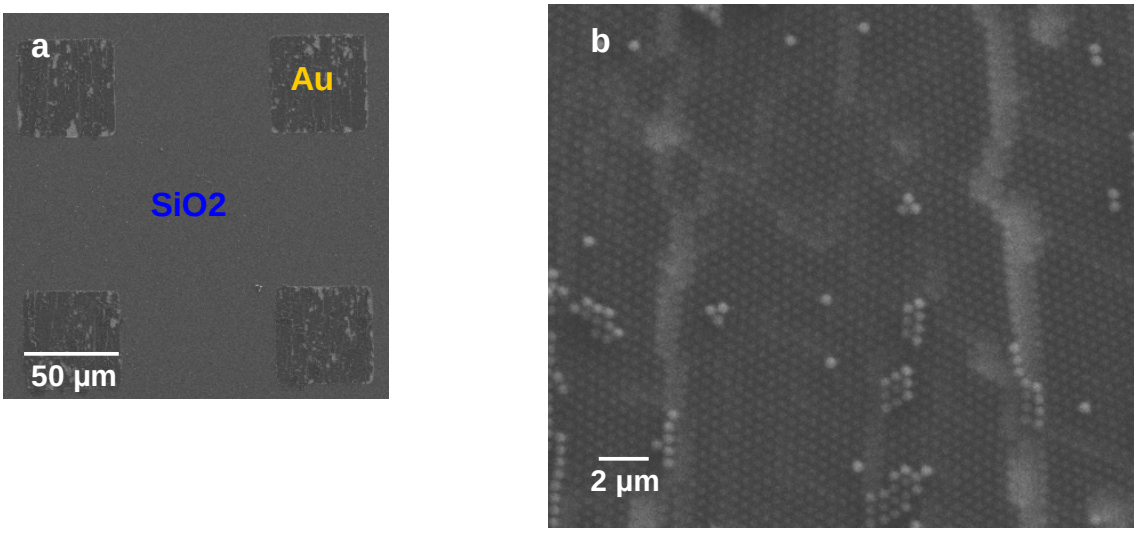

Figure 3-20 (a) Polystyrene nanospheres with 500 nm diameter stayed on the gold pads forming the mono-layer structure on the photolithographically patterned substrate after the rinsing process. (b) Magnification of Au pad area.

With the vertical deposition technique, nanospheres can be deposited to the patterned substrates, covering the whole surfaces (both hydrophilic and hydrophobic parts) **(Figure 3-19 (a) (b)).** Then, the mono-layer structure can be easily formed on the gold pads by a rinsing process with methanol **(Figure 3-20),** which is consistent with our observation that the polystyrene nanospheres can stick on the gold surface not on glass surface. The key point for this process is the pinning of nanospheres on the substrate at the beginning, which is strong enough to repel the dragging force for nanospheres in the suspension to attach on them forming the multi-layer structure. To trigger this mechanism, the sharp contact angle between solution and substrate is

necessary. We designed an experiment to show this vital role of nanospheres pinning at the first stage of the deposition. Au-coated substrate was scratched by a knife to expose a straight line of the glass surface. Then, the vertical deposition technique was performed with the substrate, where the scratched line was parallel to the surface of solution. We did find multi-layer structure formed under the scratched line, and no deposition occurred far away from the line, which is exactly what we expected according to our theory. **(Figure 3-21)**.

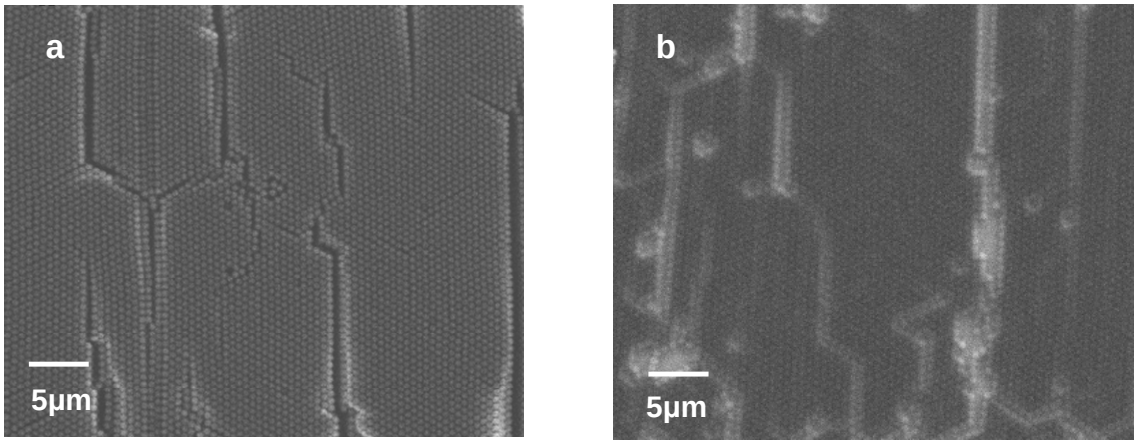

Figure 3-21 (a) Multi-layer structure was formed under the scraped straight line on the gold-coated substrate with a parallel straight line of glass surface. (b) mono-layer structure of polystyrene nanospheres.

CHAPTER 4

SYNTHESES AND OPTICAL PROPERTIES OF GOLD NANOVOID ARRAYS

The synthesis of gold nanovoid arrays by means of templated electrochemical deposition method is described. The nanovoid structure with various thicknesses of films can be fabricated simply by controlling the charges (time) during the electrochemical deposition. The structural dependence of the optical properties of the resulted nanovoid arrays are discussed.

4.*1 Syntheses of Au nanovoid array*

Periodic array of gold cup/nanovoid structures were sunthesized by the templated electrochemical deposition into colloid self-assembled polystyrene nanosphere crystals. The multi-layer polystyrene nanosphere structure assembled on the glass cover slip coated with a conductive gold layer was used. By controlling the total charges, the different thickness of the Au nanostructures can be produced **(Figure 4-1)**. The detail procedure is described below. First, the multi-layer nanosphere structures were produced on the Au-coated glass cover slip using nanosphere self-assembly methods described in Chapter 3. Then, the electrochemical deposition was performed using the potentialstatic mode with the noncyanide gold electrolyte (TG-25ES-RTU, Technic Inc.) in a three electrode cell, where the Au-coated glass cover slip with multilayer structures was used as working electrode, platinum mash as counter electrode,

and silver-silver chloride electrode as reference electrode. The deposition potential was set to -0.45V (vs Ag/AgCl reference electrode). By controlling the charges (deposition time), the different thickness of the gold cup/void nanoarray structures can be created. Finally, the polystyrene spheres were dissolved using toluene in a ultrasonic bath for 5 min, followed by rinsing with the IPA and DI water.

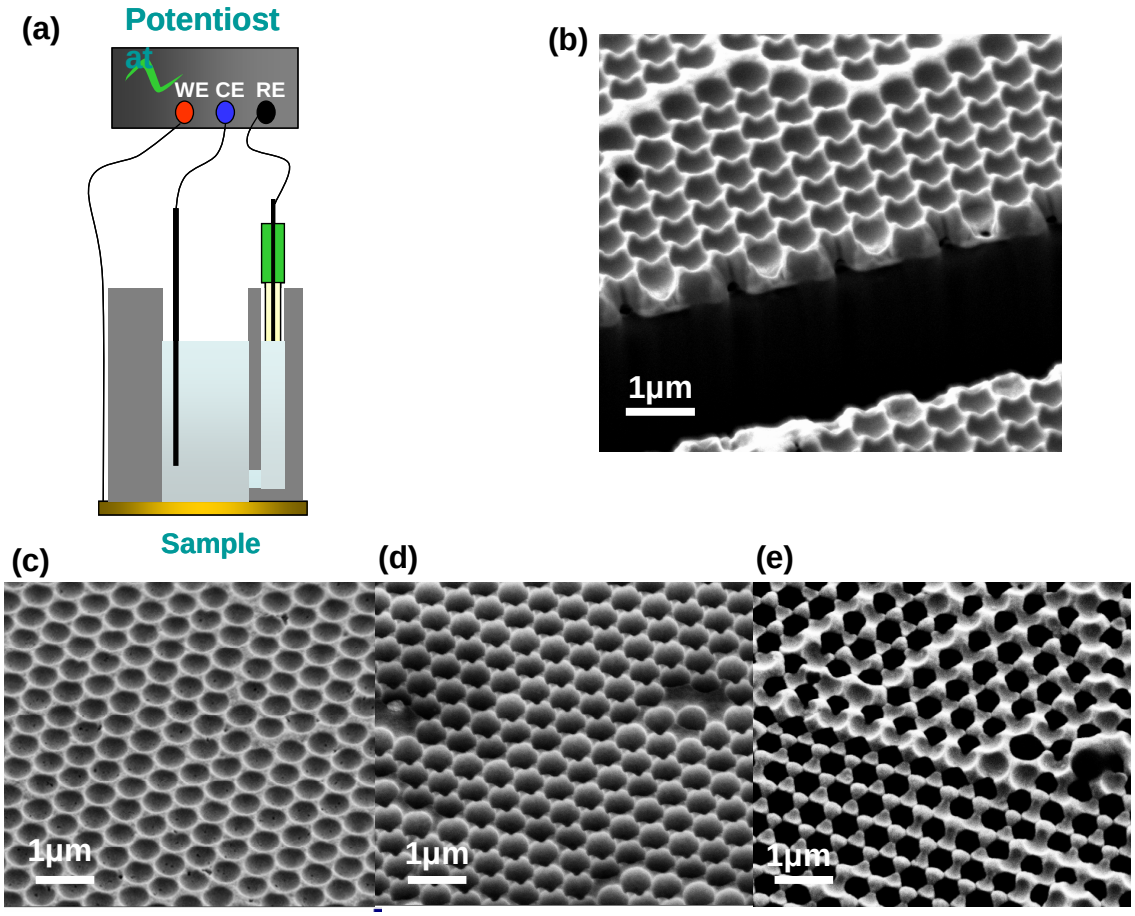

Figure 4-1 (a) Set-up of electrodeposition cell. (b) Cross-section of the cup/void structure. (c) Thickness of film is about 120 nm under 0.15C of charge. (d) Thickness of film is about 200 nm under 0.2C of charge. (e) Thickness of film is about 350 nm under 0.4C of charge.

For the application as the probe, the small holes under cups were created by dipping the structure into a gold etchant (GE-8111, transene inc.) and a Cr etchant (Chromium Etch 1020, transene inc.) for a few seconds, respectively.

4.2 PlasmonicProperties of Au Nanovoid Arrays

4.2.1 Introduction

The periodic void structures embedded in the gold film, which can support a lot of plasmon modes correspondent to both localized surface plasmon and surface plasmon polariton, have been widely studied and demonstrated by Baumberg and Bartlett et al.[64-67]. The resonant frequency can be tuned simply by the choice of the different sphere size and by the thickness of the pattern film controlled by the electrochemical deposition. There are several fundamental characteristics of this structure. First, under resonant condition, the extent of intense electric field of the void structure is much larger than that of the metal particles, which is usually less than 10 nm around the sphere. Second, the intense field is uniformly distributed on the surface due to the ordering of the periodic arrays. The metal particles usually aggregate to form a disordered structure, leading to non-uniform field distribution. The enhanced field mostly comes from the hot spots which is usually irreproducible. Third, the void structure has reduced damping due to the fields concentrated inside the dielectric cavity and better plasmon confinement due to narrower plasmon linewidths in the spectrum. Since the field enhancement depends on both the reradiation(optical loss) and damping

(adsorption loss), a stronger signal can be produced from the void structure. These properties make the nanovoid structure a good candidate for the sensing applications.

In a typical Au nanovoid arrays SERS substrate, the light is incident on the upper surface of the voids arrays and the signal is collected on the same side. It requires the sampling of the analytes and the placement of the sample to the substrate surface. In order to use Au nanovoid arrays as signal amplifier on optical fiber tips for in situ or in vivo sensitive sensing where the light is incident on the bottom of the arrays, a new structure has been designed. In this structure each void has two openings on both sides, one side mounted to the fiber tip surface for introduction of incident light and collection of scattered light, another side for analyte molecules getting into the voids. It is this unique feature that makes it possible for nanovoids arrays to be used on a fiber tip. Without the opening of the holes on the bottom of the arrays, one cannot obtain enhanced electrical field inside the voids when the light from the fiber is incident on the bottom surface of the array. We will focus on the fiber-based application of the nanovoid structure, as substrates for plasmonic and SERS sensors.

4.2.2 Surface Plasmon Resonant Frequency of Au Nanovoid Array

The surface plasmon resonant frequency can be measured as the minimum in the reflection spectrum. The surface plasmon polariton on the flat metal surface cannot be excited directly by the light because the dispersion curve of the surface palsmon polariton lies outside the light cone (as discussed in Chapter 2). The periodic structure of the nanovoids acts as the phase-matching tool to couple the light with the surface plasmon. **(Figure 4-2)**The in-plan vector of light can be modified to[68, 69]:

$$k = k\sin\theta + g_{pq} \qquad \textbf{(4-1)}$$

$$g_{pq} = pA + qB \qquad \textbf{(4-2)}$$

$$A = 2\pi(b \times n)/|a \times b| \qquad \textbf{(4-3)}$$

$$B = 2\pi(n \times a)/|a \times b| \qquad \textbf{(4-4)}$$

where

the a, b are the primitive vectors of the crystal lattice;

the A, B are the primitive vectors of the reciprocal lattice.

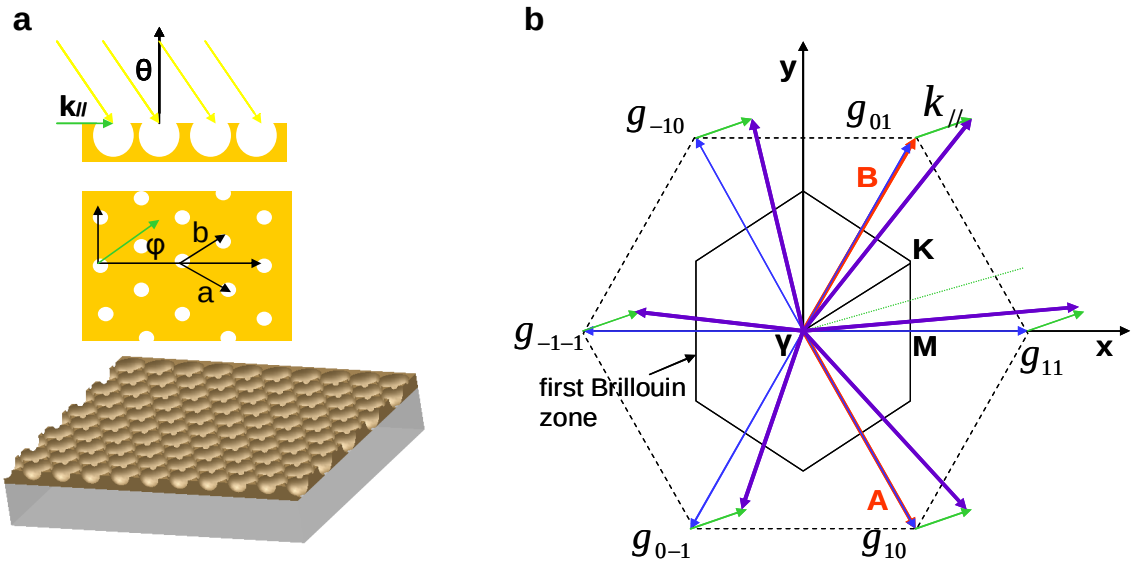

Figure 4-2 (a) Illustration of nanovoid structure with light incident with a tilt angle θand azimuthal angle ψ. (b) Wave vector is changed due to the grating effect. The first Brillouin zone and the wave vector g_{pq} of surface plasmon polaritons in the lowest frequency subband.

When the modified wave vector k matches the wave vector of surface plasmon polariton β, $\beta = \frac{\omega}{c}\sqrt{\frac{\varepsilon\varepsilon_m}{\varepsilon+\varepsilon_m}}$, then the surface plasmon can be excited. The surface

plasmon polariton is a leaky wave inherently, i.e. they lose energy due to the absorption inside the metal. The destructive interference between this leaky radiation and the reflected part of the excitation beam leads to the minimum in the reflection spectrum.

For the fiber-based application, the analytic solution contacts with the nanovoid structure on the front side, and the light is incident and collected from the back side of the structure, so we focused on the reflection from the back side of the structure. The measurement was conducted at the normal incident angle using a home-built Vis-NIR spectrometer. The set-up **(Figure 4-3)** and detailed measurement procedure are described below.

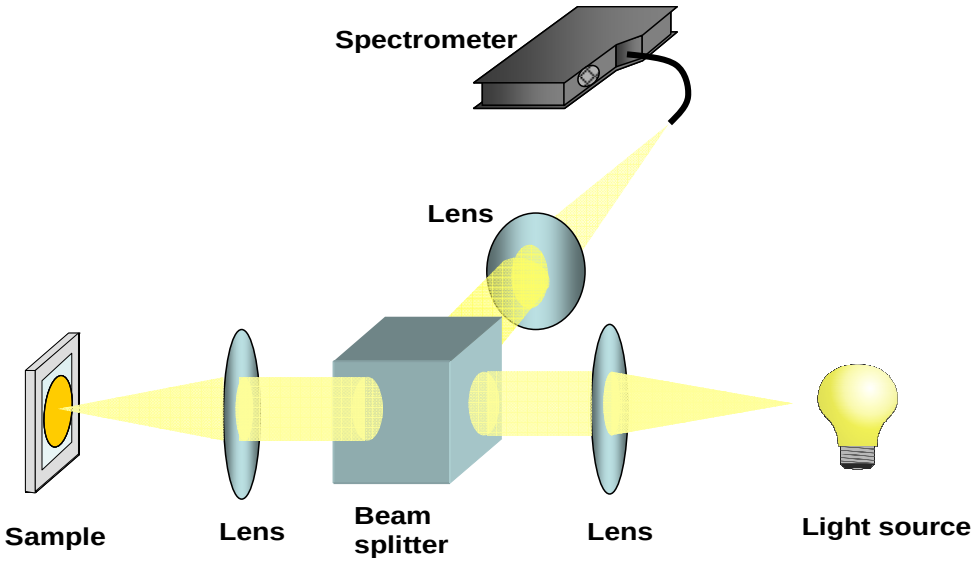

Figure 4-3 Illustration of set-up for reflection spectrum measurement.

A broadband (350 nm to 1100 nm) Tungsten Halogen lamp source was connected to a reflectance module via Vis-NIR optic fibers. In the module the light was directed from the fiber to a 50:50 beam splitter via a collimating lens. The beam splitter

transmitted half the light to a focusing objective lens and was incident on the sample. The objective lens also acted as a collection lens and redirected the reflected light back into the beam splitter which reflects the light through a focusing lens to a Vis-NIR optic fiber connected to a spectrometer. The fluidic cell, which is composed of the sample, a hollow square poly-(dimethylsiloxane) (PDMS) frame as the spacer layer, and a cover glass slide, was assembled to insert the analyte solution and mounted on the stage for measurement. The reflectance measurement was taken with 5 ms integrating time.

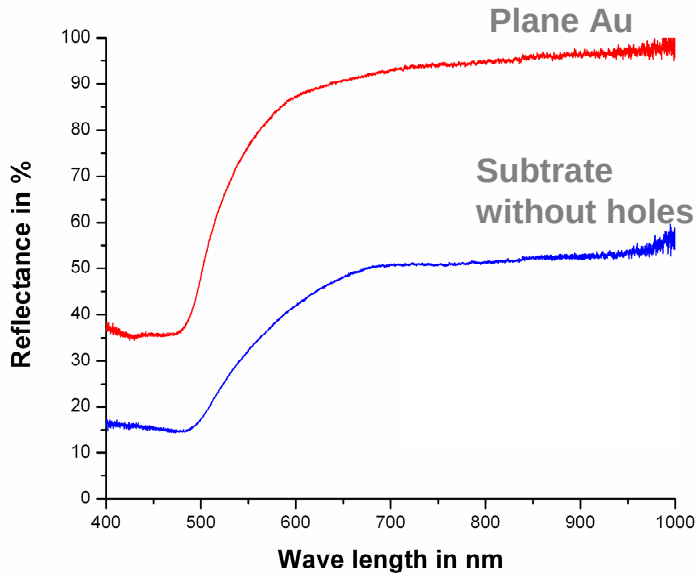

Figure 4-4 Reflection spectra of plane gold surface and nanovoid structure with void dimeter 450nm and film thickness 230 nm measured measured by illuminating the light from the back side normally.

When measuring nanovoid array without opening the bottom holes, as shown in the reflection spectrum in **Figure 4-4**, no dips appear. The reflection spectrum is similar to that of flat gold surface except the weaker intensity. This means no surface plasmon

modes has been excited. This result can be explained by the concept of phase-matching. Due to the greater wave vector of surface plasmon polariton, the matching tool has to be used to excite it. Even though there exist two potential mechanisms in this structure to excite the surface plasmon polariton, the conditions were not right. First, the glass slide used as the substrate can act as the prism to modify the in-plane wave vector via the equation $k_x = k\sqrt{\varepsilon}\sin\theta$ to excite the surface plasmon polariton on at the metal/ air interface. But the normal incident condition brings the wave vector close to zero. Second, the periodic array of nanovoid pattern on the front side can act as the grating to excite the surface plasmon. However, the surface of the structure is flat when the light is incident from the back side. By creating the bottom holes on the back side of the substrate, this problem is resolved.

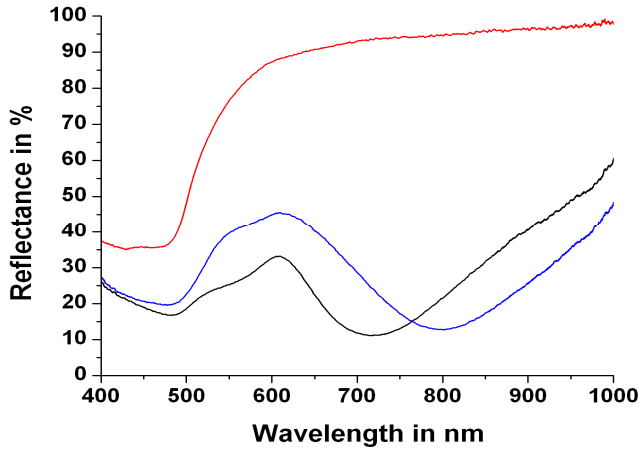

Figure 4-5 Reflection spectra of nanovoid structure, which has the void dimeter 450 nm, film thickness 230 nm, and bottom hole diameter 150 nm, measured by illuminating the light from the back side normally. Red line: reference measured from the plane Au film; black line: measured under air condition (refractive index 1); blue line: measured under water condition (refractive index 1.33).

In the reflection spectrum for the substrates with the opening of the bottom holes **(Figure 4-5)**, it clearly shows the dip. A large red sift of the resonant frequency is also observed when the media surrounding the substrate is changed from air to water. The simulation based on the finite difference time domain method was carried out (see details in the next section). The simulated reflection spectra show the similar dip positions comparing with experiment results. The red shift of resonant wavelength due to the change of refractive index of the medium is also clearly seen in the spectra **(Figure 4-6)**. This result reveals us two things: the surface plasmon polariton can be excited in this structure and its resonant frequency is strongly affected by the medium.

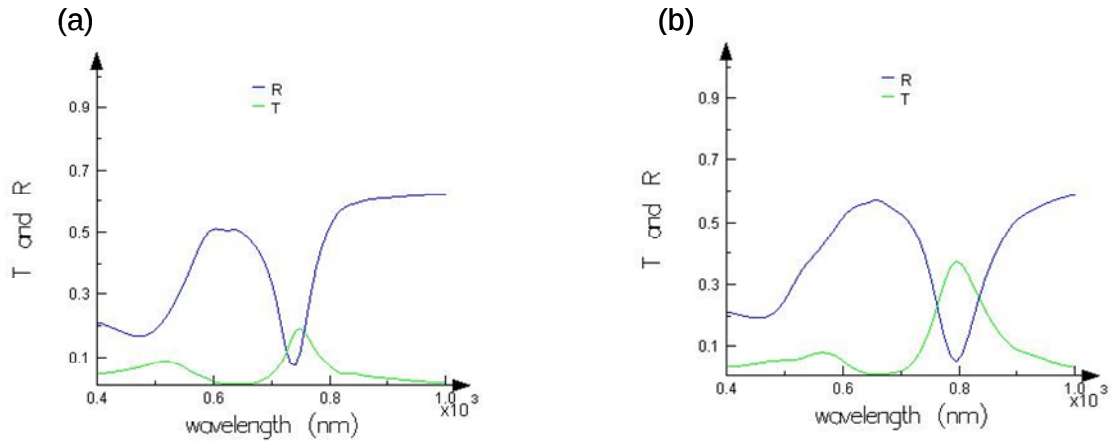

Figure 4-6 Reflection and transmission spectra obtained from the simulation under the same condition as Figure 4-5. (refractive index of the medium is (a) 1, (b) 1.33.)

4.2.3 Finite Difference Time Domain (FDTD) Simulation

For the SERS application, to maximize the signal, the resonant frequency of the plasmonic structure has to match with the frequency of applied laser light. The plasmon resonant frequency is strongly dependent to the shape and size of the structure, the

dielectric constants of the structure material and the surrounding medium, the incident angle and the polarization of the light, and orientation of the structure. Therefore, we cannot just use the trial and error to find the optimum structure which has the same resonant frequency as the incident laser light. The simulation has to be carried out to find the optimum parameters of the substrate with the specific resonant frequency. We used the finite difference time domain (FDTD) method to solve the Maxwell's equations. In the simulation, the Maxwell's equations can be expressed as[70]:

$$\frac{dB}{dt} = -\nabla \times E - J_B - \sigma_B B \qquad \textbf{(4-5)}$$

$$\frac{dD}{dt} = \nabla \times H - J \ - \sigma_D D \qquad \textbf{(4-6)}$$

where D is the displacement field, ε is the dielectric constant, J is the current density, J_B is the magnetic-charge current density, B is the magnetic flux density, μ is the magnetic permeability, H is the magnetic field, and σ_B, σ_D correspond to magnetic and electric conductivities respectively.

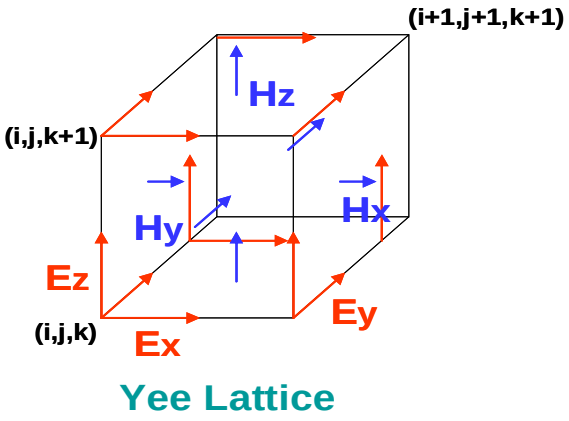

Figure 4-7 Illustration of Yee lattice in 3D for a single grid voxel.

In this method, the space and time are divided into a discrete grid made up of so-called Yee lattice **(as shown in Figure 4-7)**. The three components of E are stored on the edges of the cube, while the components of H are stored on the faces of the cube. As the grids are made finer and finer, this becomes a closer approximation for the true continuous equations. The field pattern, the reflection/transmission spectra, and the resonant modes can be attained, which allows us to compare with the experimental data to find the optimum structure of the substrate. The detailed procedure and results of FDTD simulation are described in the appendix. Briefly, the geometry of structure to be simulated was first generated. Then, other parameters like dielectric constant of the structure material and the surrounding medium and the direction and polarization of the light source were entered. Finally, the different kinds of monitors can be chose to obtain the correlated information.

The laser light with wavelength of 785 nm was used as light source in the measurement of SERS. Therefore, the purpose of the simulation is to find the suitable nanovoid structures with the plasmon resonance around 785 nm. In the simulation, the effect of structural parameters, including void diameter, film thickness, and the bottom hole diameter, on the plasmonic properties of the nanovoid arrays was investigated. The resonant frequency of the surface pasmon is characterized as the minimum in the reflection spectrum.

Figure 4-8 shows the simulated reflection and transmission spectrum with the two dimensional plot of the enhancement of the electric field when illuminated using the light with the same SPR frequency of the nanovoid structures with different void

diameters (350, 450, 500 nm) but with the same Au film thickness of 230 nm and a bottom hole diameter of 150 nm located on the bottom of each void. The refractive index of the medium 1 (air) was used in this simulation. It can be seen that resonant frequency red shifts as the diameter of the void increases.

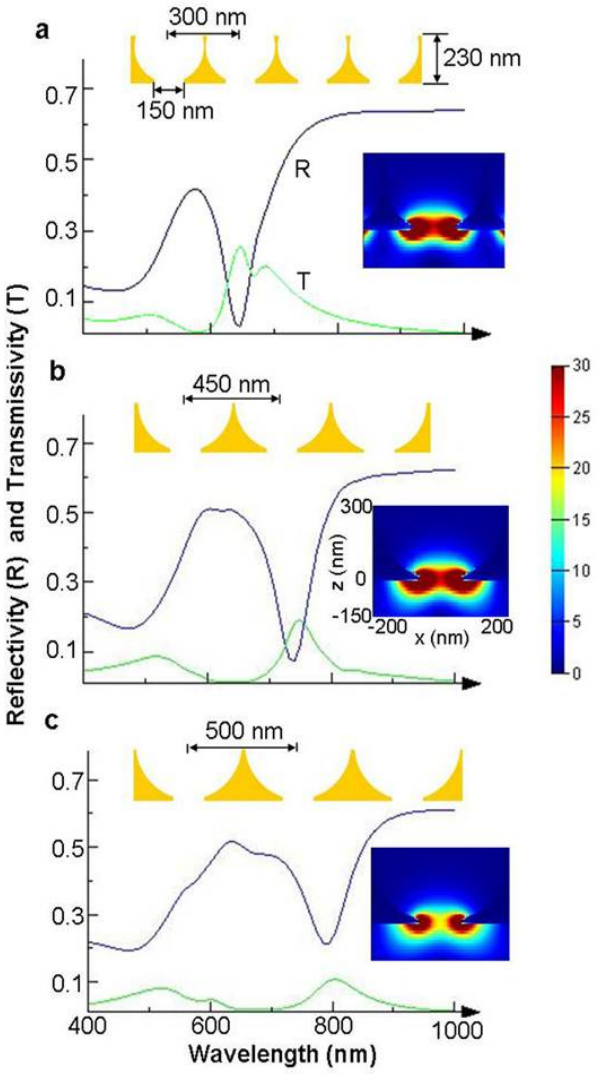

Figure 4-8 The simulated reflection and transmission spectrum with the two-dimensional plot of the enhancement of electric field when illuminated by the light with the SPR frequency for nanovoid structures with different void diameters (350 (a), 450 (b), and 500 nm (c)).

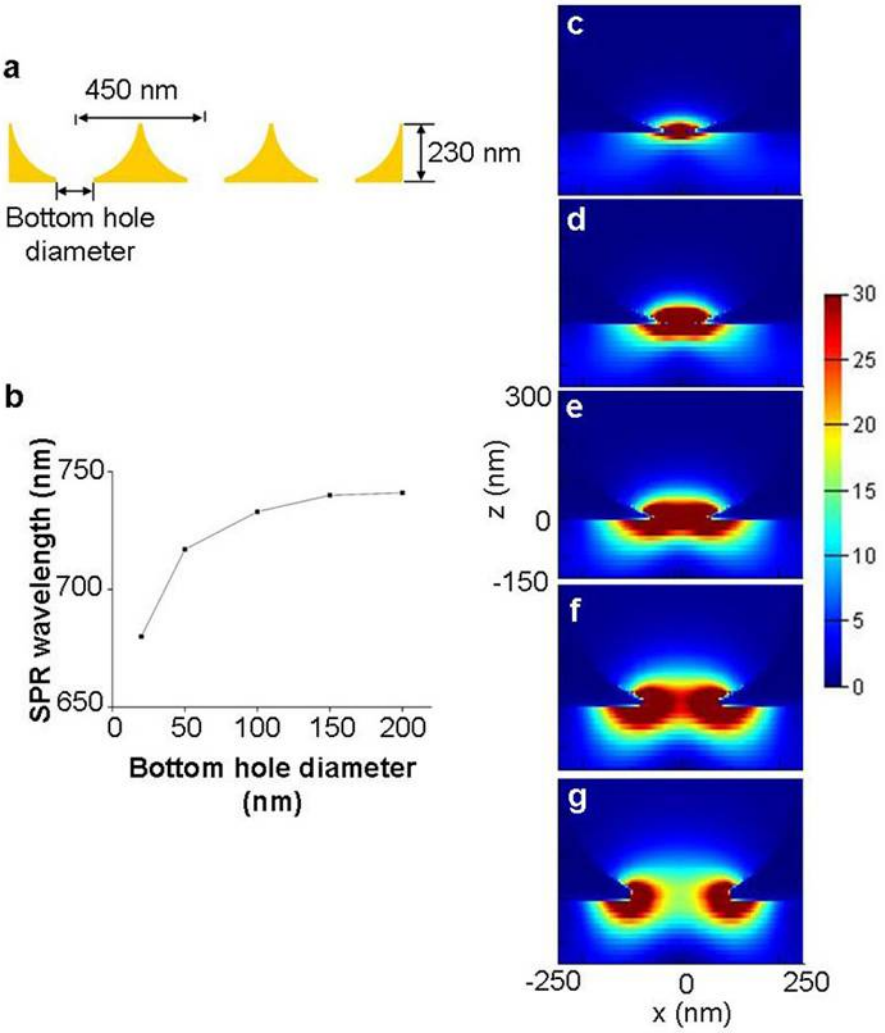

Figure 4-9 The effect of the bottom hole size on the SPR peaks and the distribution of the enhanced electric field inside the void when illuminated by the light with the SPR wavelengths. (a) Illustration of the structures simulated. Void diameter is 450 nm and the film thickness is 230 nm. (b) Plot of SPR wavelengths as a function of bottom hole diameters. Other structural parameters are kept the same. (c) – (g) The enhanced electric field for the structures with the bottom hole diameter of 20 (c), 50 (d), 100 (e), 150 (f), 200 (g) nm, respectively.

Shown in **Figure 4-9** is the effect of the bottom hole size on the SPR peaks and the distribution of the electric field inside the void. As the hole size increases the SPR

peak only slightly shifts towards longer wavelength, but the enhanced electric field extends much more into the voids.

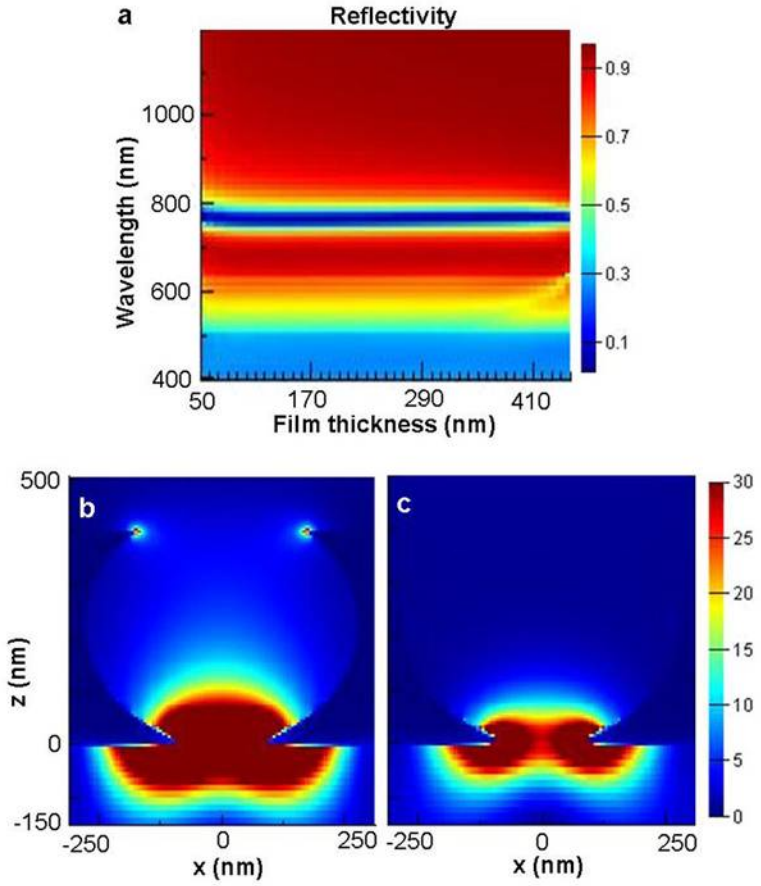

Figure 4-10 The effect of the Au thickness on the plasmonic properties of the void array structures. (a) The plot of reflectivity of nanovoid arrays with different film thickness and at different wavelengths. The wavelength with the minimum reflectivity is the SPR wavelength. (b) and (c) Plots of the distribution of the enhanced electric field inside the void with film thickness of 400 nm (b) and 230 nm (c), respectively. All structures have a void diameter of 450 nm and a bottom hole size of 150 nm.

Figure 4-10 shows the effect of the Au thickness on the plasmonic properties of the void array structures. All structures have a void diameter of 450 nm and a bottom hole size of 150 nm. **Figure 4-10(a)** is the plot of reflectivity of nanovoid arrays with different film thickness and at different wavelengths. The wavelength with the

minimum reflectivity is the SPR wavelength. It shows that the thickness has little effect on the position of SPR peaks. However, the distribution of the enhanced electric field changes significantly with the film thickness. **Figure 4-10 (b)** and **(c)** are the plots of the distribution of the enhanced electric field inside the void with film thickness of 400 nm and 230 nm, respectively, when illuminated by the light with SPR wavelengths. It can be seen that as the film thickness increases, more electric field is concentrated inside the void.

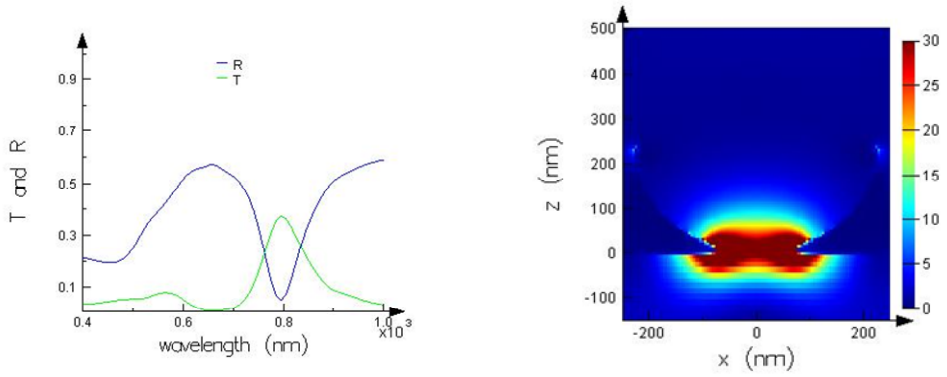

Figure 4-11 The simulated reflection and transmission spectrum with the two-dimensional plot of the enhancement of electric field when illuminated by the light with the SPR frequency for nanovoid structures with void diameter 450 nm in the refractive index of medium 1.33.

To mimic the experimental conditions, the refractive index of the medium has been changed to 1.33 (water) and conducted the same simulation for all the structures. We found the nanovoid structure with a diameter of 450 nm has the resonant wavelength in 795 nm, which is very closed to the laser wavelength of 785 nm used in the experiments **(as shown in Figure 4-11).** We fabricated various nanovoid structures with the diameter of 220, 456, and 750 nm. We found that the nanovoid structure with

void diameter of 456 nm possessed a resonant frequency closed to 785 nm, which is in a very good agreement with the simulated results.

4.3 Using Au Nanovoid Arrays as Substrates for Optical Fiber-based Sensing Applications

The surface plasmon resonant (SPR) frequency is very sensitive to the structure of the substrate and the surrounding medium. This can be utilized for sensing applications, which is termed as SPR spectroscopy. SPR spectroscopy is a surface sensitive technique to detect the refractive index changes within the evanescent field around the metal-dielectric interfaces. The plasmon resonance condition shift, due to the change in the refractive index of the medium, can be detected as intensity, angle, or wavelength shifts to provide quantitative information of the analyte solution. Our nanovoid structures can be used as substrates in the SPR spectroscopy.

As we know, when the frequency of the incident light matches with the surface plasmon resonant frequency resulted from the structure of the substrate, the external field can be largely enhanced around the metal-dielectric interface. This can be applied in the Raman spectroscopy to enhance the detected signal to form so-called surface enhanced Raman spectroscopy (SERS). We also use Au nanovoid arrays for SERS.

4.3.1 SPR spectroscopy

The application of Au nanovoid arrays for SPR spectroscopy was demonstrated. By changing the concentration of the analyte solution to vary the refractive index of the medium to which the substrate is exposed. The detail set-up for the measurement is the

same as the reflection measurement except a polarizer is added to compare the influence of the different polarities of incident light. The nanovoid structure with void diameter of 456 nm and Au film thickness of 230 nm was used for the measurement. The glycerine (86%) diluted with DI water to various concentrations were used as the analytical solutions. The refractive indexes for different concentrations, and the resonant frequencies measured under the vertically and horizontally polarized condition were shown in the **(Table 4-1)**. The reflection spectra and the correlation between the resonant frequencies and refractive indexes were plotted in **Figure 4-12**. For both polarized conditions, it shows that there is a linear relationship between resonant frequencies and refractive indexes which is determined by the concentrations of the solution. Therefore, the concentration of the analyte can be precisely determined using this resonant frequency-refractive index relationship.

Table 4-1 The average SPR frequencies of Au nanovoid arrays under different refractive indices corresponding to glycerin concentrations with the incident light polarized vertically and horizontally with the x axis of the sample stage respectively.

% glycerin	refractive index	Ave. Ver. SPR	Ave. Hor. SPR
0	1.33303	822.51	819.11
12	1.34792	826.18	821.25
22	1.35945	830.02	823.26
42	1.38616	834.48	828.73
65	1.4197	842.35	833.75
86	1.45313	845.13	837.62

Under different polarized directions, the resonant frequencies for the same concentration of the solution changed. This can be understood as the coupling between

the plasmons: the coupling between the localized plasmon and surface plasmon polariton, or between localized plasmons themselves via the tip mode which appears for the structures with the film thickness larger than half of the diameter of the void.

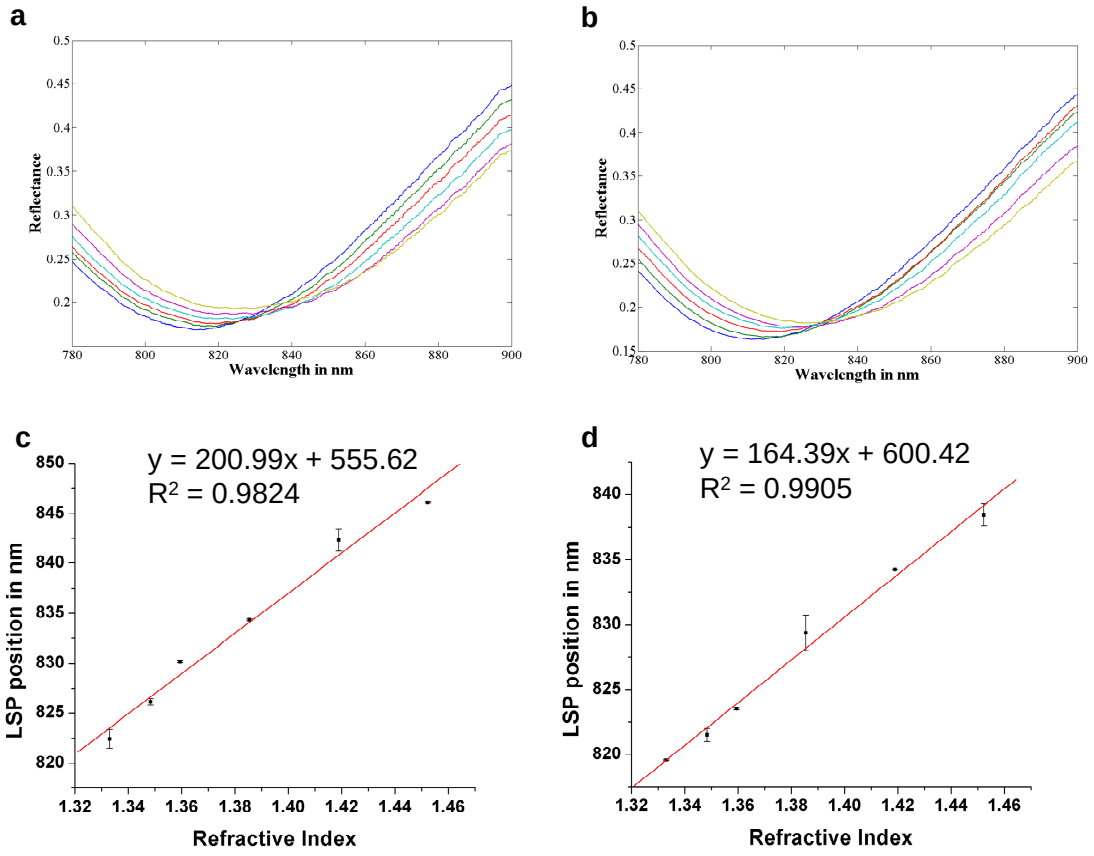

Figure 4-12 Measured reflectance spectra (a, b) and corresponding plots (c, d) of relationship between SPR frequencies and refractive indices of the medium under different glycerin concentrations with the incident light polarized vertically (a, c) and horizontally (b, d) with the x axis of the sample stage respectively.

For comparison, the simulation with the same structure and experimental conditions was carried out. The reflection and transmission spectra with corresponding electric field intensity and distribution in media with different refractive indices, 1 for air, 1.33 for water, 1.45 for 86% of glycerol are shown in the **Figure 4-13.** The

simulated resonant frequencies for all the three conditions are in very agreement with those measured in the experiments.

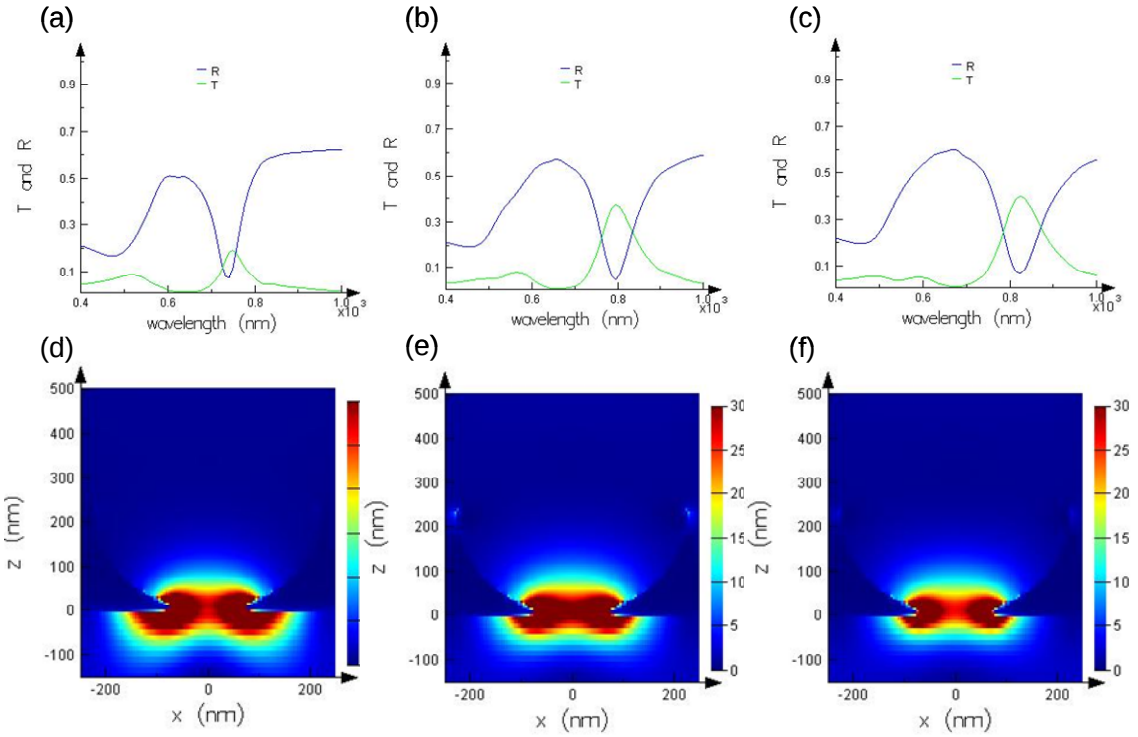

Figure 4-13 Reflection and transmission spectra correlated to electric field intensity and distribution under different refractive indices, (a, d)1 for air, (b, e)1.33 for water, (c, f)1.45 for 86% of glycerol, obtained from the FDTD simulation.

This sensing mechanism can also be applied in biosensors to probe interaction between an analyte in solution and a biomolecular recognition element immobilized on the plasmon active substrate surface to provide the real-time analysis of the molecules in the medium. The SPR biosensor offers several advantages. The SPR biosensor can be tailored to detect any kind of analyte by choosing a suitable biomoleculer recognition element for the analyte. The binding between the analyte and recognition element can be directly observed without the use of any labels such as fluorescence.

4.3.2 Surface Enhanced Raman Spectroscopy (SERS)

The nanovoid structures with void diameter of 456 nm and Au film thickness of 230nm were chose as SERS substrate since the wave length at plasmon resonance for these structures is near 800 nm which is closed to the laser wave length 785 nm used in the Raman measurement.

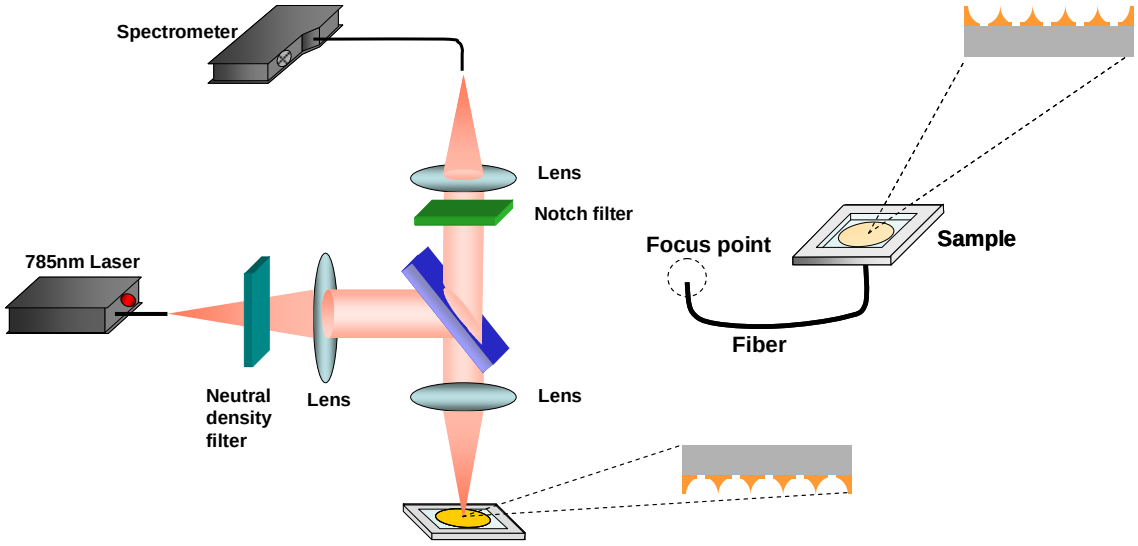

Figure 4-14 Diagram of the modular Raman optical setup used to measure the SERS signal from the Au Nanovoid array at a normal angle of incidence. The samples can be illuminated with a microscope objective or a multimode fiber by attaching appropriate optic at the input path of the Raman module.

The SERS spectra were measured by a home-built Raman spectroscopy. The detailed set-up and measured procedure are described below **(Figure 4-14)**. The 785 nm laser for sample excitation is couplee to a Raman module through an optical fiber (600 um, NA=0.39). At the Raman module, the light from the fiber is attenuated using a neutral density filter (ND=0.2), collimates after a dichroic mirror onto a 20x, 0.4 NA objective lens with working distance of 8.4 mm, and is then incident on the sample.

Back scattered light from the sample is collected by the objective lens and transmitted by the dichroic to a notch filter before being focused by a 10x, 2.5 NA lens into optic fiber (600 um, NA=0.39) which then led to a spectrometer . The spectra were taken over 3s integration time. The Au nanovoid array substrates were tested with two analytes, 3,3'-Diethylthiatricarbocyanine iodide (DTTC) and Cresyl violet (CV), in solution form. DTTC and CV were first dissolved in solvents and mixed in distilled water in 5:95 ratios. The final concentration of DTTC and CV used for the experiments were 0.08 mM and 1 mM, respectively. The analyte solutions were injected in the fluidic cell for SERS measurement.

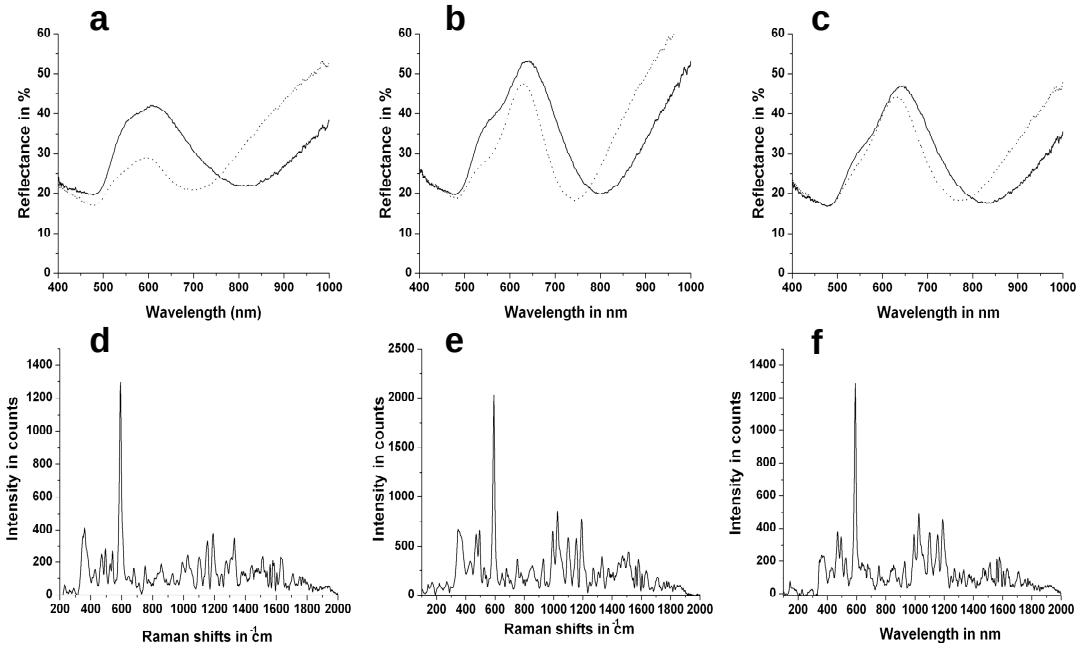

Figure 4-15 Measured reflectance spectra (a-c) and corresponding Raman spectra (d-f) of Au Nanoviod array with 450 nm diameter voids and film thickness around 250 nm. The different SPR peaks result from the variation of bottom hole sizes due to the different etching time. The Raman spectra are of Crystal Violet.

Reflectance spectra of fabricated Au nanovoid arrays were measured at normal incidence angle. The light was incident on the glass cover slips. The reflectance measurements obtained from the substrates with (dotted line) and without (solid line) water in the fluidic cell for three different samples with varying bottom hole sizes are shown in **Figure 4-15**. A large red spectral shift of the localized plasmon resonance in the near infrared region (~ 720-750 nm range) is observed for all nanovoid structures when the media surrounding the substrate is changed from air to water. The SERS spectra of CV for these three slightly different void arrays are also shown in **Figure 4-15**. Although a distinct SERS spectra is recorded from each sample but the largest enhancement is detected when the plasmon resonance of the sensor is closest to the excitation wavelength. This clearly demonstrates the expected strong correlation between the match of SPR and Raman excitation wavelengths and the enhancement of Raman scattering. It is noteworthy that when conducting SERS using nanoparticles in solution, it is found that this correlation does not always hold. When maximum Raman scattering signals are recorded, the excitation wavelength differs significantly from the SPR wavelength of the nanoparticles. Though many possible mechanisms have been proposed, the reason is still not well understood.

The comparison between SERS measurements using microscope with focused light and optical fiber is illustrated in **Figure 4-16**. For the optical fiber experiment, the sample was just attached on the cleaved side of the fiber **(Figure 4-14 right)**. The set-up for the fiber-based measurement is the same as for above-mentioned SERS measurements except the light after the Raman module is focused onto a piece of

multimode fiber (200 nm, NA=0.22) with sample attached on the other side. SERS signal created also passed through the fiber entering the Raman module and was then collected by the spectrometer. SERS spectra of CV recorded with focused light using a lens (blue line) and a multimode fiber (200 µm core) directly attached to the sample (red line) are compared in **Figure 4-17**, in which spectra are displayed with a vertically offset for the sake of clarity. Even though the scattered light collection efficiency of the multimode fiber is low, the distinct vibrational mode of CV was still clearly visible in both spectra.

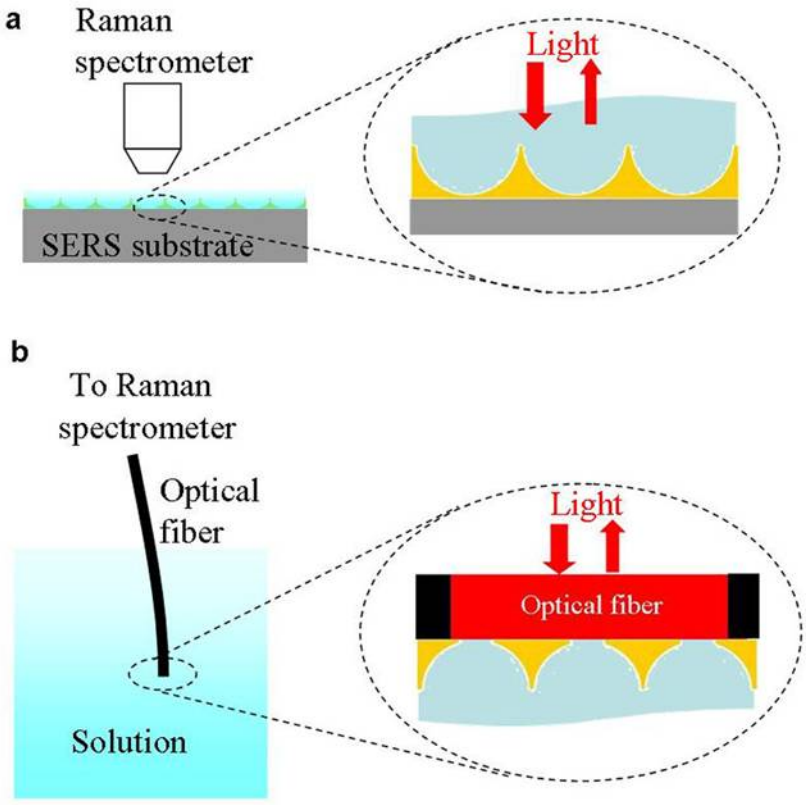

Figure 4-16 Illustrations of using Au nanovoid arrays as conventional SERS substrate (a) and for a fiber-based SERS sensor.

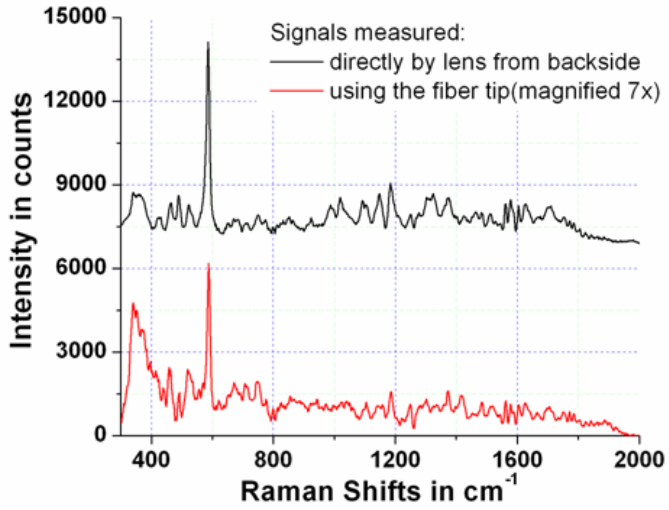

Figure 4-17 Measured Raman spectra of Crystal Violet on Au Nanovoid array when illuminated with a microscope objective (20×, 0.4 NA) (red) and multimode fiber directly in contact (black) with back side of the sensor, respectively. The spectra have been vertically offset for the sake of clarity.

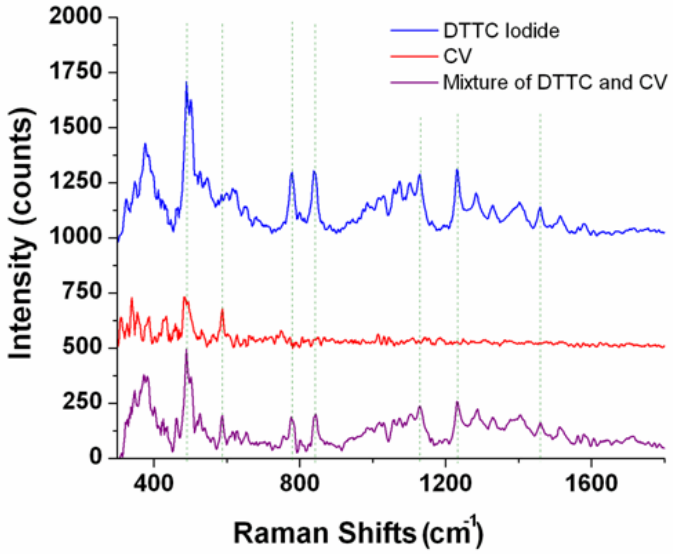

Figure 4-18 Demonstration of multiplexed detection from mixture of two dyes (DTTC and CV). Shown are the Raman spectra of each pure dye and their mixture. Major peaks belonging to each dye are identified in the Raman spectra of the mixture.

The nanovoids were further tested for their ability to detect multiple Raman analytes by mixing two freshly prepared Raman reporter dyes Cresyl violet (1 mM) and DTTC Iodide (80 uM) and injecting the mixture into the cell. **Figure 4-18** shows the Raman signatures of the individual dyes; cresyl violet (red) and DTTC iodide (blue) and the spectrum from the mixture (purple). All the spectra were obtained using the fiber over a 3s integration time. The 587.73 cm^{-1} vibrational mode of cresyl violet can still be clearly seen as well as 778.69 cm^{-1}, 843.23 cm^{-1} and 1129.61 cm^{-1} among other vibrational modes of DTTC iodide.

CHAPTER 5

CONCLUSION

We developed a method to make the multi-layer and mono-layer close-packed structure of polystyrene nanospheres by means of capillary-convective force. The mono-layer crystal of polystyrene nanospheres on Au surface can be produced by simply washing the multi-layer structures with methanol. By directly visualizing the self-assembling process using optical microscopy, a mechanism based on the 2-D crystal formation and 3-D repulsive force model has been proposed to explain the process. Using interaction energies between two identical media (nanospheres) and between two different media (nanosphere-substrate), the formation of mono-layer structures can be qualitatively explained. This method not only allows us to make the multi- or mono-layer structures by the same process but also provide us a way to study the formation of first mono-layer related to the whole structure in the future research.

We developed the vertical deposition technique to produce polystyrene nanosphere crystal structure with single orientation on hydrophilic glass substrates. In order to obtain the structure on the hydrophobic gold surface, lithographically patterned substrate has been used. We found that it is the contact angle of the colloid nanosphere solution on the substrates that control this self-assembly process.

The nanosphere crystal structures were used to fabricate Au nanovoid arrays by electrochemical deposition into the intervals between spheres. Au nanovoid arrays can

serve as a plasmonic structure, which is extremely sensitive to changes in the refractive index of the surrounding medium, and whose surface plasmon resonant (SPR) frequency is closely related to the size and morphology of the structure. It can be applied in the surface Plasmon resonant (SPR) spectroscopy and the surface enhanced Raman spectroscopy (SERS) to detect the extremely low concentration of molecules. In order to use Au nanovoid arrays as sensors on optical fiber tips for in situ or in vivo sensitive sensing where the light is incident on the bottom of the arrays, a new structure has been designed. In this structure each void has optical openings on both sides of the nanovoid array , one side is mounted to the fiber tip surface for introduction of incident light and collection of scattered light and the other side is for interrogation of analyte molecules in the voids. The effect of structural parameters, including void diameter, Au film thickness, and the bottom hole diameter of the nanovoid arrays on the electric field confinement are investigated using three-dimensional finite difference time domain (FDTD) simulation. We found that it is this unique feature that makes it possible for nanovoids arrays to be used on a fiber tip. Without the opening on the bottom of the arrays for introduction of light, one cannot obtain enhanced electrical field inside the voids when the light from the fiber is incident on the bottom surface of the array.

We demonstrated that our Au nanovoid arrays are suitable for fiber-based SERS sensors. The large SERS-active zone (the enhanced electric field extends 100 nm into the voids) which is several orders of magnitude larger than particle-based sensors makes our nanovoid arrays well suited for in situ and in vivo sensing applications. A large SERS-active zone would potentially result in quick response time which is critical for

many in situ and in vivo applications. In addition, owing to its large SERS active zone, this structure has the potential for direct SERS sensing of macromolecules such as proteins and DNAs. Unlike SERS spectra of small molecules, SERS spectra of macromolecules usually do not resemble their normal Raman spectra and are often not reproducible. The reason is that only the part of macromolecules in close proximity to the metal surface can be enhanced [71], and that which part gets enhanced is a random process. With a SERS-active zone in nanovoid array structures is much larger than macromolecules, we expect all parts in a macromolecules will be enhanced, and therefore a reproducible result can be obtained, realizing a label-free direct SERS sensing of macromolecules. The simplicity and low cost of the fabrication process of nanovoid arrays is another very important advantage comparing to nanoparticle-based SERS sensors. This even makes it possible to have disposable sensor tips for each measurement, which is a highly desirable feature for all in situ and in vivo applications. This will become a research subject in the future.

We also demonstrated the Au nanovoid array can be applied in the surface plasmon resonant (SPR) spectroscopy to detect the concentration of the analyte. This concept can be used in biosensing to detect the biomolecule qualitatively and quantitatively such as immunoassays, protein conformational changes, DNA hybridization, and small molecule binding interactions. The sensitivity of the SPR spectroscopy can be rather improved by labeling the target analyte with plasmonic nanoparticles (NPs). These labels increase the refractive index at the metal surface and couple to the metal substrate electromagnetically, leading to larger SPR shifts.

APPENDIX A

FINITE DIFFERENCE TIME DOMAIN (FDTD) SIMULATION

The FDTD solution (software from Lumerical Solutions, Inc) was used to perform the simulation. The procedure to run a simulation is shown **in the Figure A-1** and each step is described respectively in more detail in the following text.

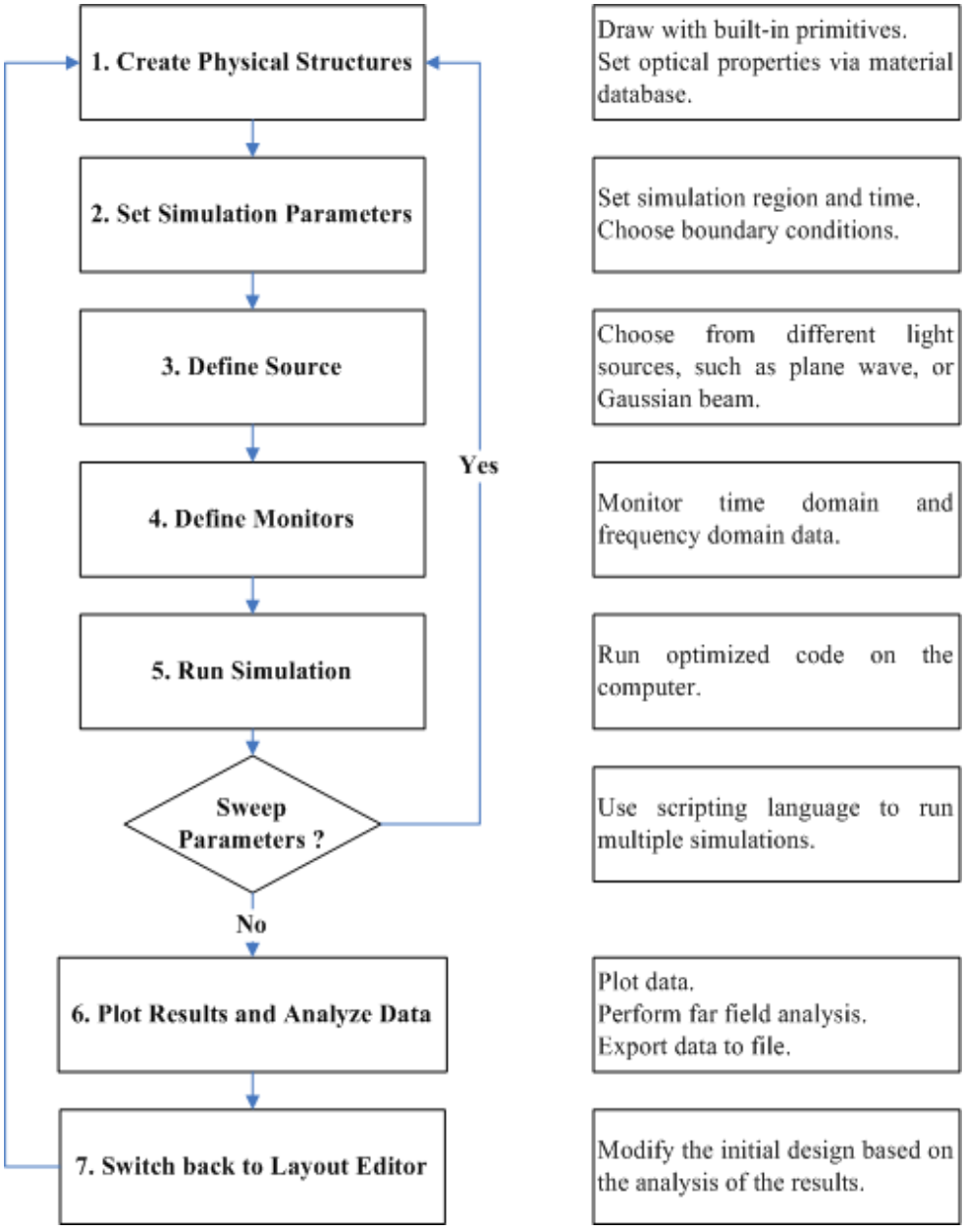

Figure A-1 The flow chart of steps involved in the FDTD simulation.

Step 1: Create Physical Structures

The structures are created by using the icons along the top of the structures tab. The various shapes of object are available, the properties of which can be set via the edit tool. Each object can be defined its own material properties by selecting from the extensive materials database or by user-defining. Dielectric, metallic and dispersive materials are supported.

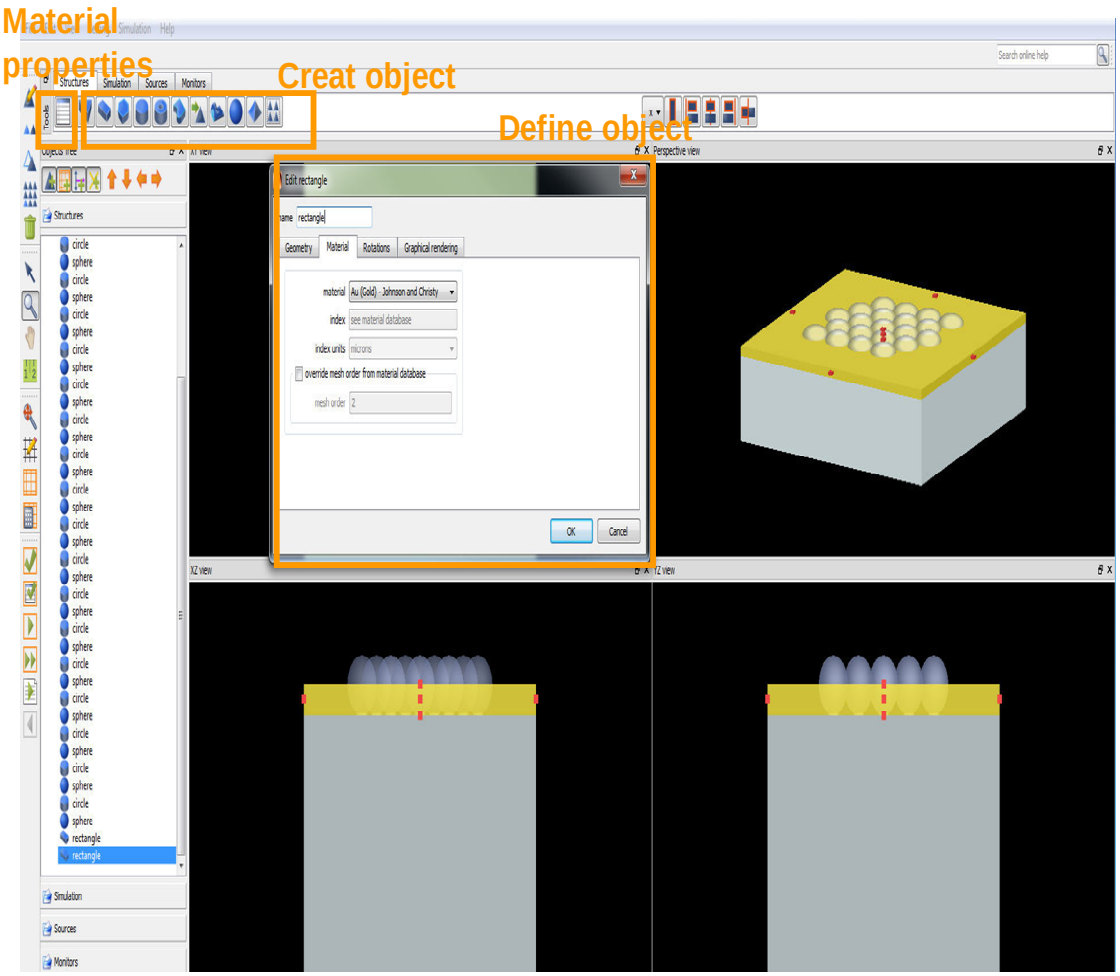

Figure A-2 Create Physical Structures.

Step 2: Set Simulation Region and Time

The simulation region is the region over which the calculation is performed. The location and size of the region must be set, and the appropriate boundary conditions must be specified. The mesh refinement object can be added to increase the precise control over the mesh in part of the simulation region. Since frequency domain information is calculated by a Fourier transform of the results obtained in the time domain, it is necessary the simulation time should be long enough to get the converged result.

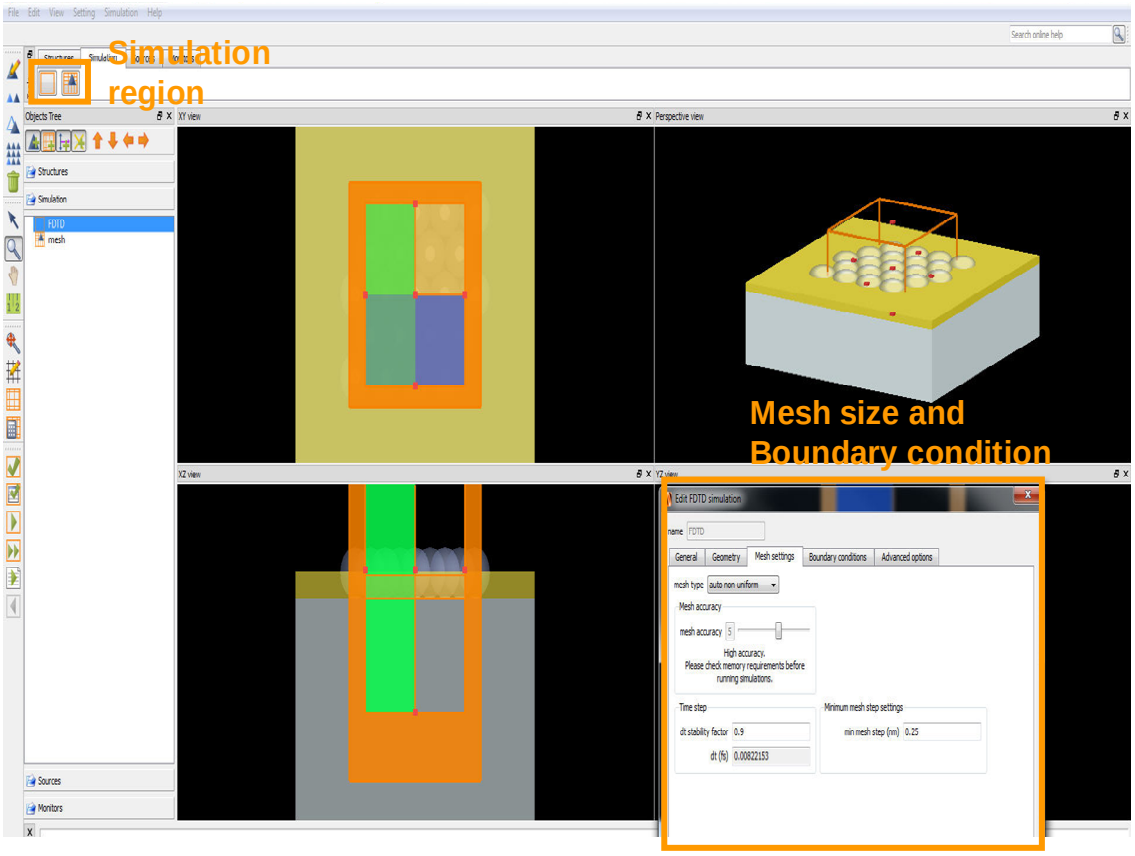

Figure A-3 Set simulation region and time.

Step 3: Define Sources

Different types of source are available for use depending on the application, e.g. point dipole useful for exciting modes in cavities and resonators, Gaussian beam and plane wave for textured surface, total field scattered field for particle scattering. The source properties like location, size, and propagation direction can be edited once created.

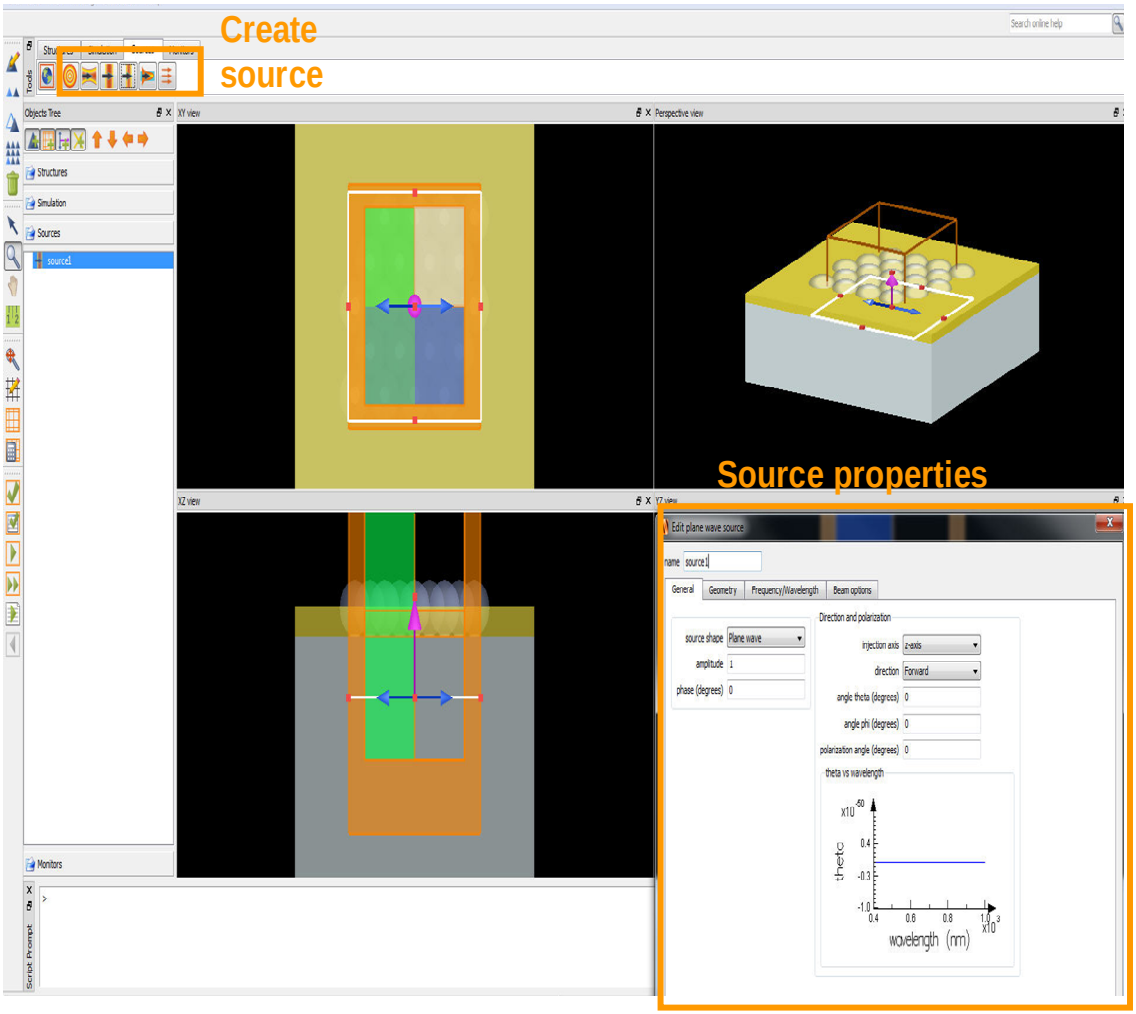

Figure A-4 Define sources.

Step 4: Define Monitors

Monitors are used to record the electromagnetic fields required for subsequent plotting and data analysis. Different types of monitors can be chose depending on the application and the required results. In addition to the basic monitors, the complex monitors comprised of basic monitors and a script to process monitor data also can be created for use.

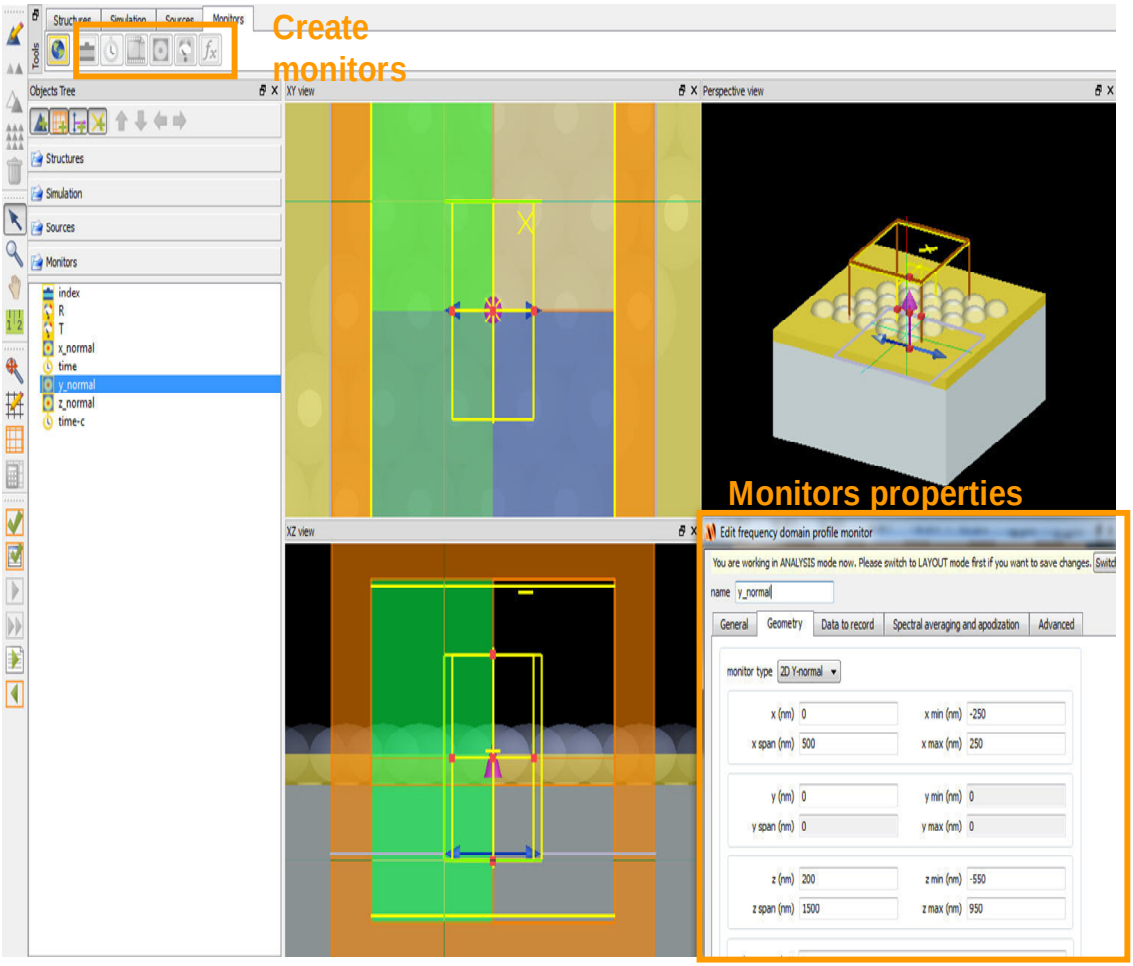

Figure A-5 Define monitors.

Step 5: Run Simulation

Once the simulation objects have been created, the FDTD project can be saved and run. The memory requirements for a particular simulation can be checked from the Check Memory Requirements on the simulation menu. The number of mesh points, where the electric and magnetic field as well as the material properties are stored, is highly related to the memory requirements. The monitors used also increase memory requirements dramatically.

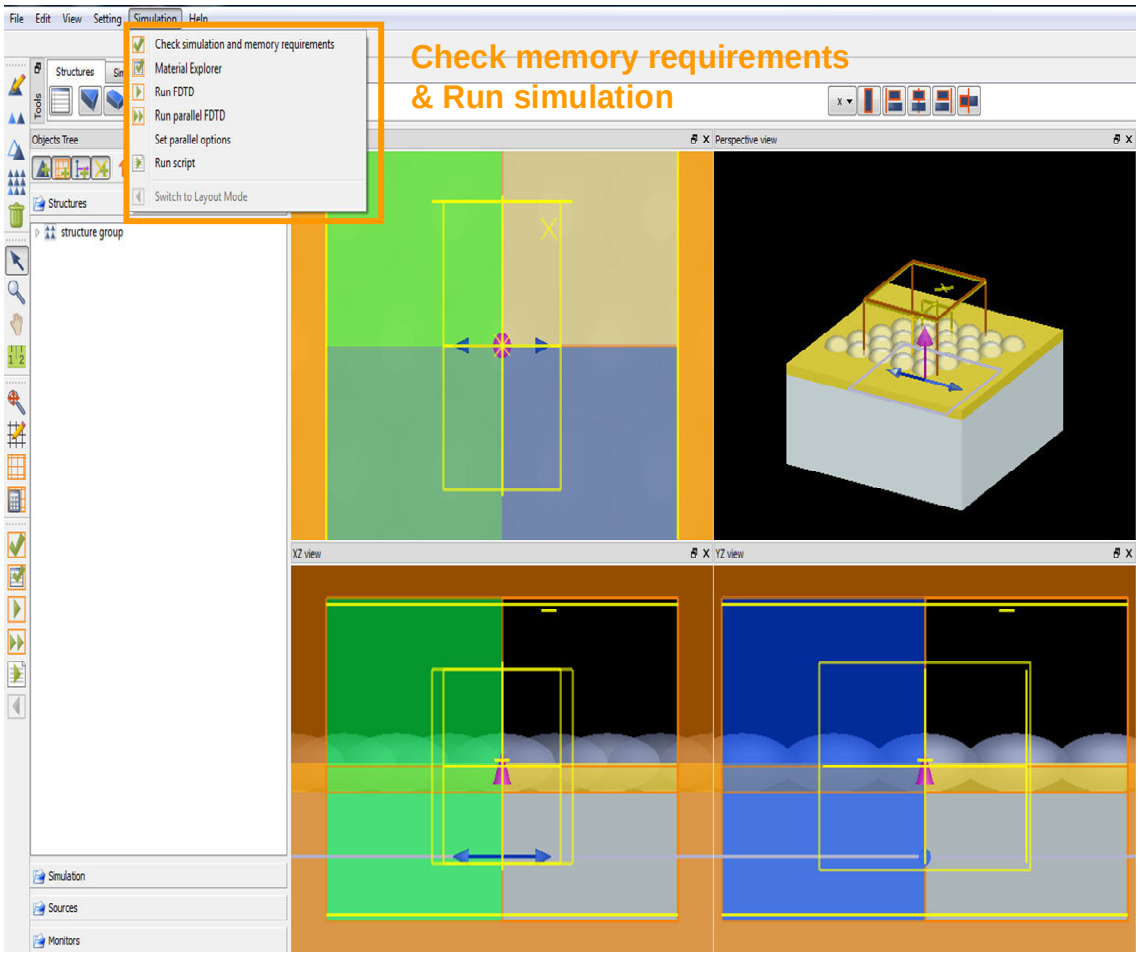

Figure A-6 Run simulation.

Step 6: Plot Results and Analyze Data

The data created for each selected monitor, after the running of the simulation, were stored in the file and can be used for the analyzation. For example, the electric field intensity can be obtained from the frequency domain field profile monitor. The results can be plotted or exported to a text file for further use. By applying the scripting language, the advance analysis can be process.

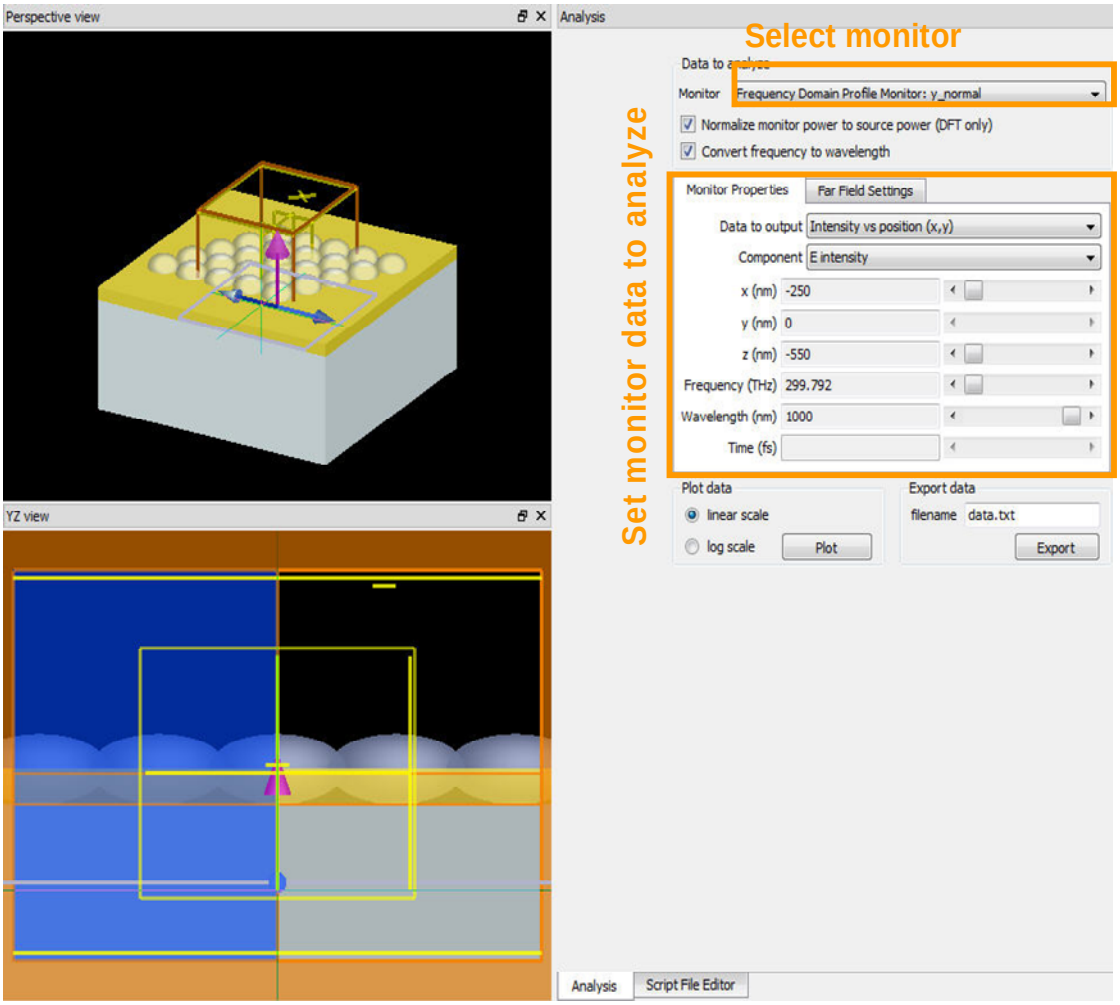

Figure A-7 Plot results and analyze data.

Step 7: Switch back to Layout Editor

Based on the results of the analysis, some modification of the initial design may be needed for another simulation. In that case, the data have to be saved under a different file name. Then, the window can be switched back from the analysis mode to the layout mode for the further design modification and simulation rerunning.

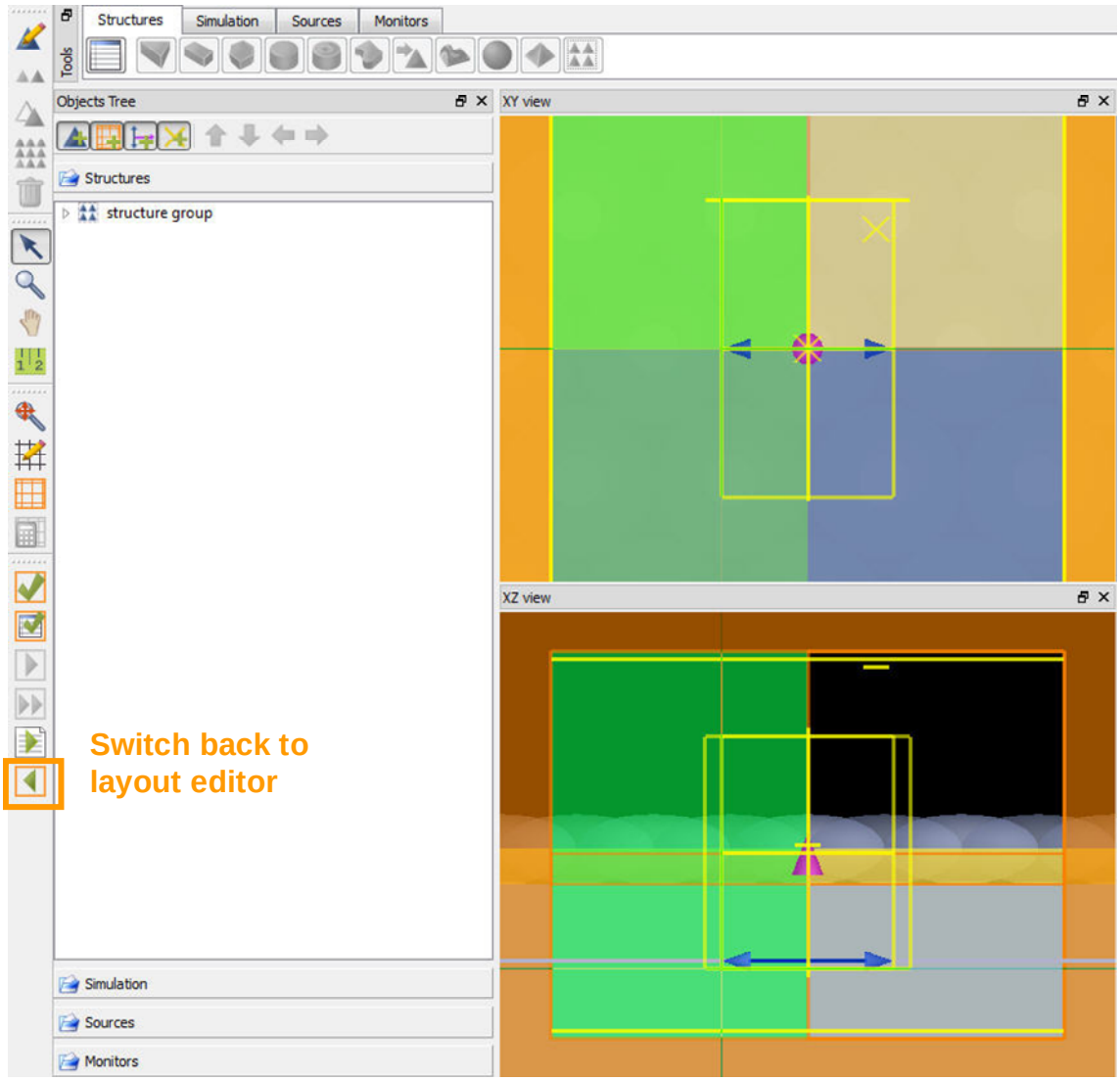

Figure A-8 Switch back to the layout.

FDTD simulation

The finite-difference time-domain (FDTD) method is a kind of method used to solve the Maxwell's equations in matters with complex geometries.

$$\frac{dB}{dt} = -\nabla \times E - J_B - \sigma_B B$$

$$\frac{dD}{dt} = \nabla \times H - J \ - \sigma_D D$$

where B is the magnetic flux density, E is the electric field, J_B is the magnetic-charge current density, D is the displacement field, H is the magnetic field, J is the current density, σ_B and σ_D correspond to magnetic and electric conductivities.

In this method, the space and time are divided into a discrete grid. The electromagnetic fields are stored at different grid location. The discretization is called Yee lattice. The E fields are stored on the edges of the cube and H fields are stored on the faces of the cube. As the grids are made finer and finer, this becomes a closer approximation for the true continuous equations. The field distribution, the reflection/transmission spectra, and the resonant modes can be attained through the simulation by computing the fields at each frequency separately or, more efficiently, by a broad spectrum response via a single computation by Fourier transforming the response to a short pulse. Here, we used the FDTD Solutions (Lumerical Solutions, Inc) to do the simulation.

Result

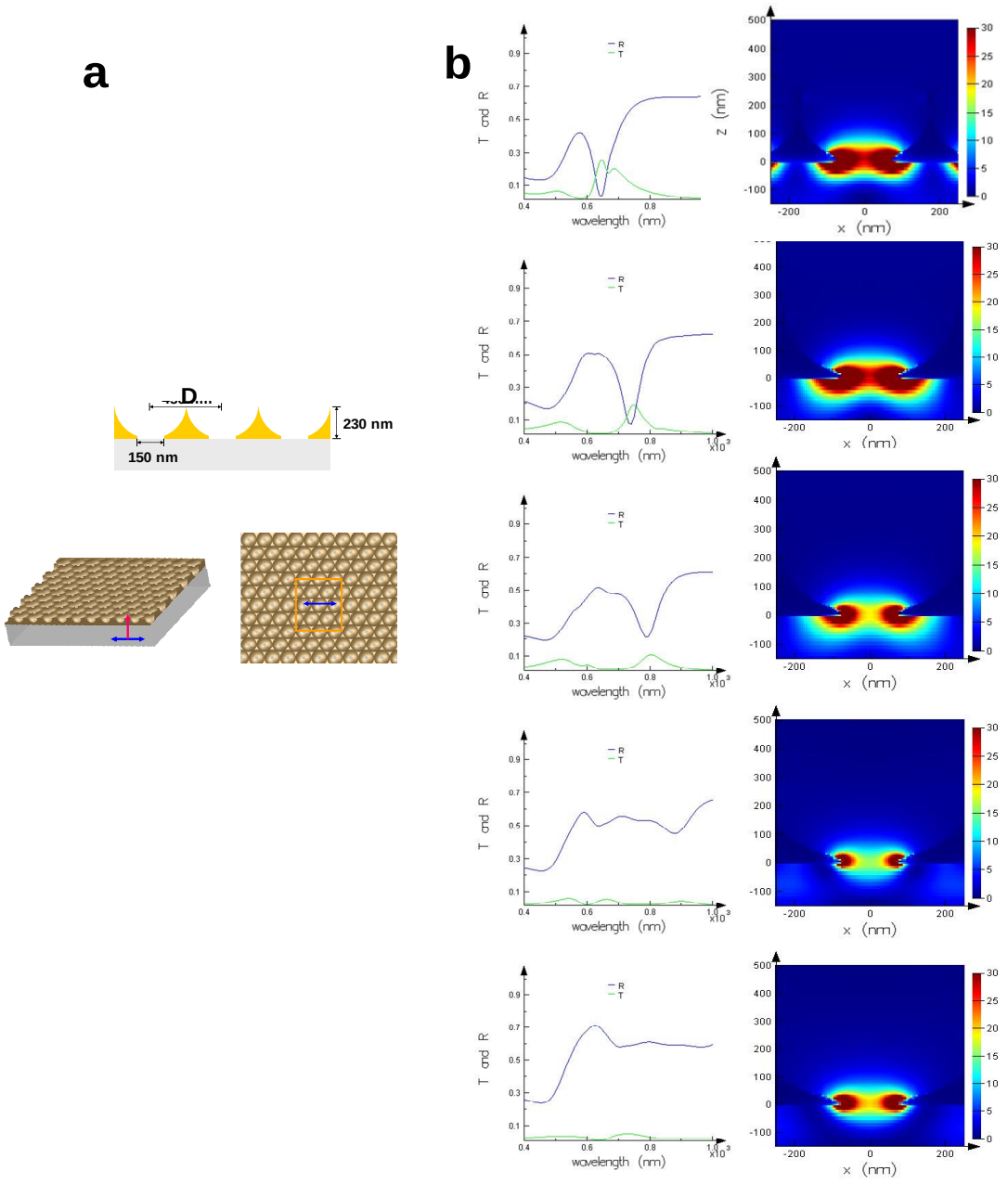

Figure A-9 The effect of the void size (D) on the SPR peaks and the distribution of enhanced electric field under resonant conditions when illuminated by light polarized along x axis (blue arrow) from the back side (red arrow) in the refractive index of medium 1. (a) Illustration of the structure simulated. The bottom hole size is 150 nm, the film thickness is 230 nm. (b) The simulated reflection and transmission spectra and corresponding plots of electric field distribution under resonant conditions. The void diameters are 350nm, 450nm, 500nm, 600nm, 700nm respectively from the top.

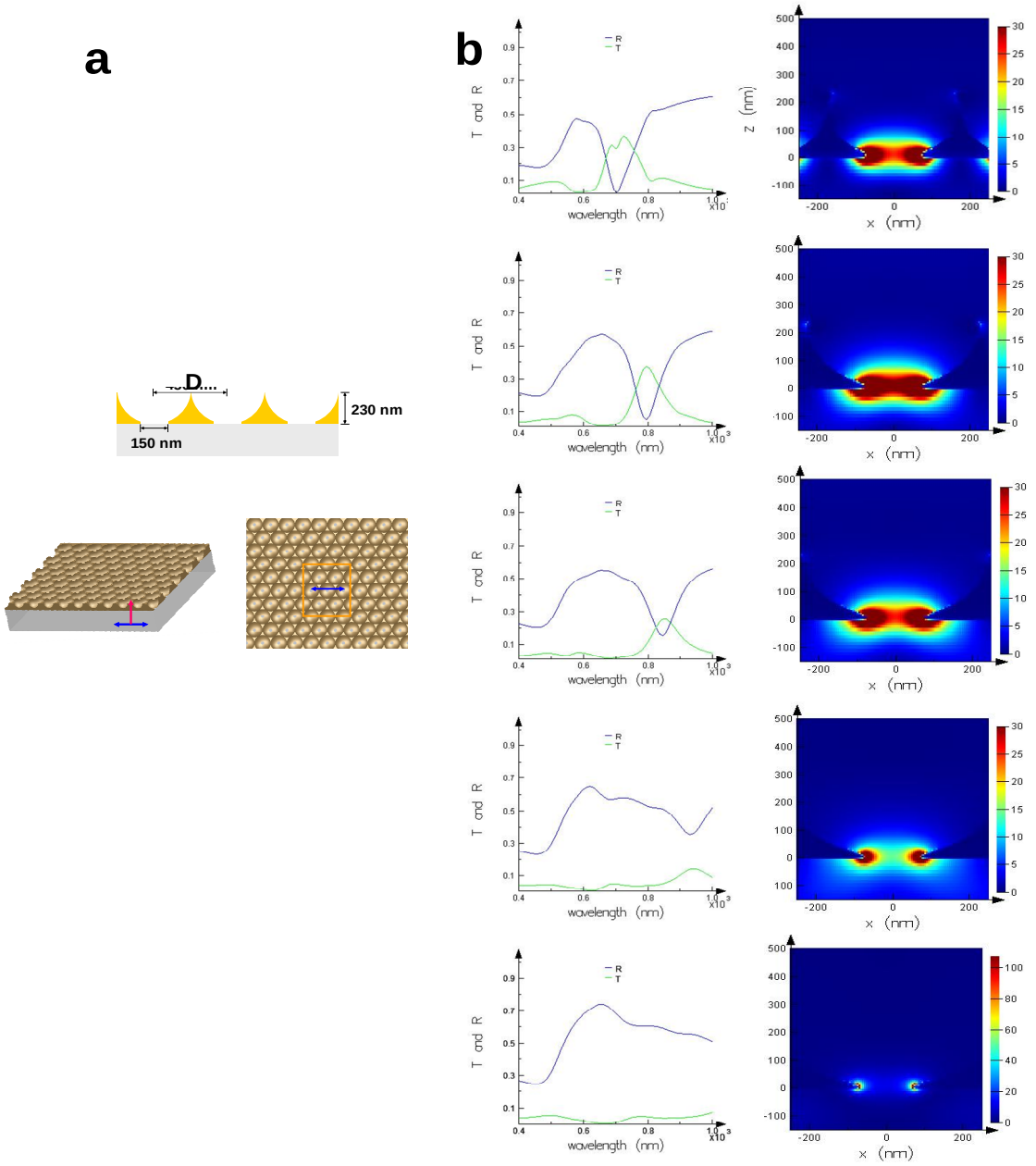

Figure A-10 The effect of the void size (D) on the SPR peaks and the distribution of enhanced electric field under resonant conditions when illuminated by light polarized along x axis (blue arrow) from the back side (red arrow) in the refractive index of medium 1.33. (a) Illustration of the structure simulated. The bottom hole size is 150 nm, the film thickness is 230 nm. (b) The simulated reflection and transmission spectra and corresponding plots of electric field distribution under resonant conditions. The void diameters are 350nm, 450nm, 500nm, 600nm, 700nm respectively from the top.

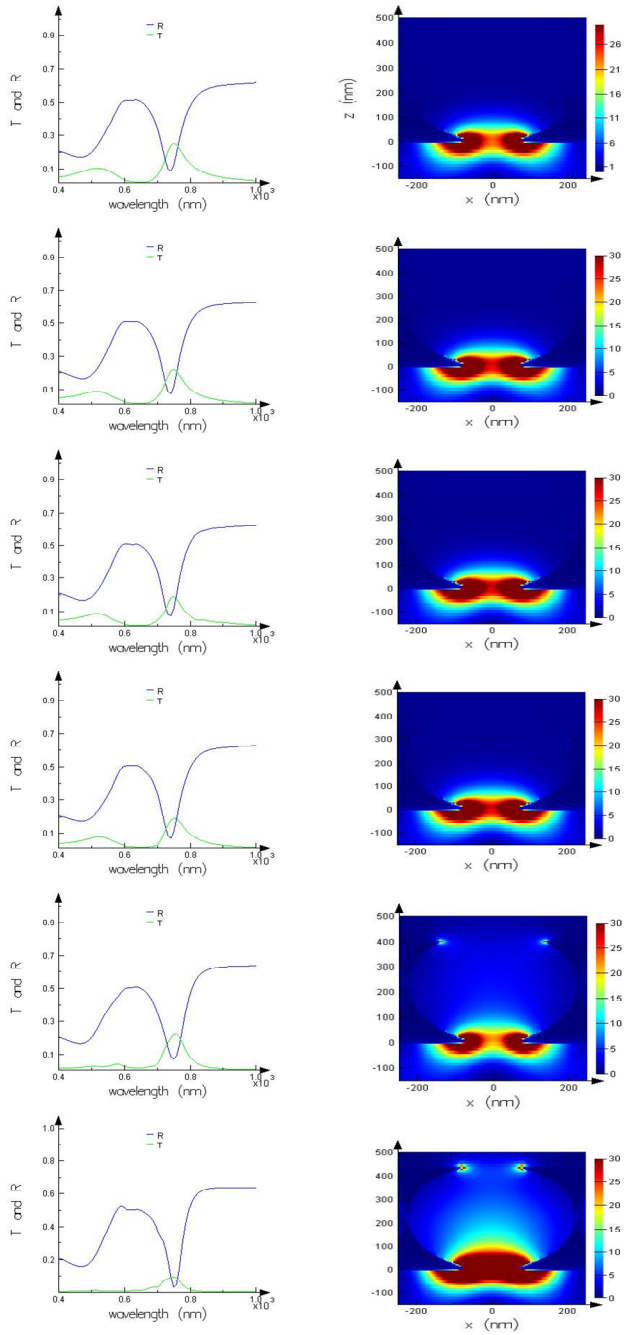

Figure A-11 The effect of the Au thickness on the plasmonic properties of the void array structures.The simulated reflection and transmission spectra and corresponding plots of electric field distribution under resonant conditions in the refractive index 1 environment. All structures have a void diameter 450nm and a bottom hole size 150nm. The film thicknesses are 100nm, 200nm, 230nm, 300nm, 400nm, 430nm respectively from the top.

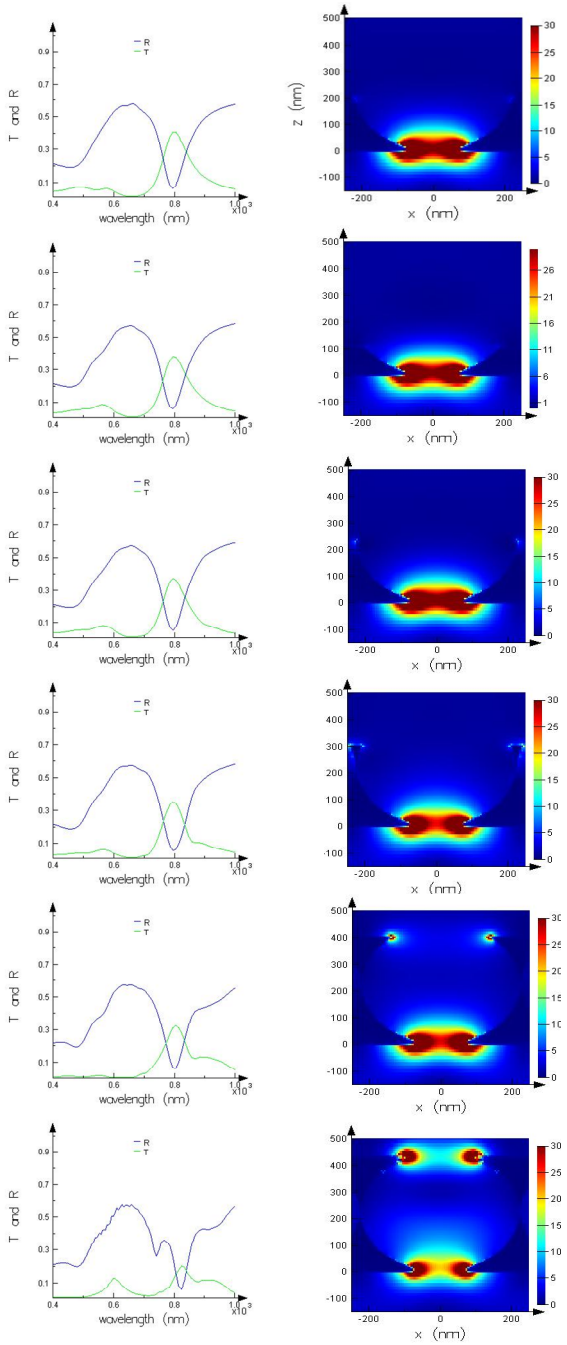

Figure A-12 The effect of the Au thickness on the plasmonic properties of the void array structures.The simulated reflection and transmission spectra and corresponding plots of electric field distribution under resonant conditions in the refractive index 1.33 environment. All structures have a void diameter 450nm and a bottom hole size 150nm. The film thicknesses are 100nm, 200nm, 230nm, 300nm, 400nm, 430nm respectively from the top.

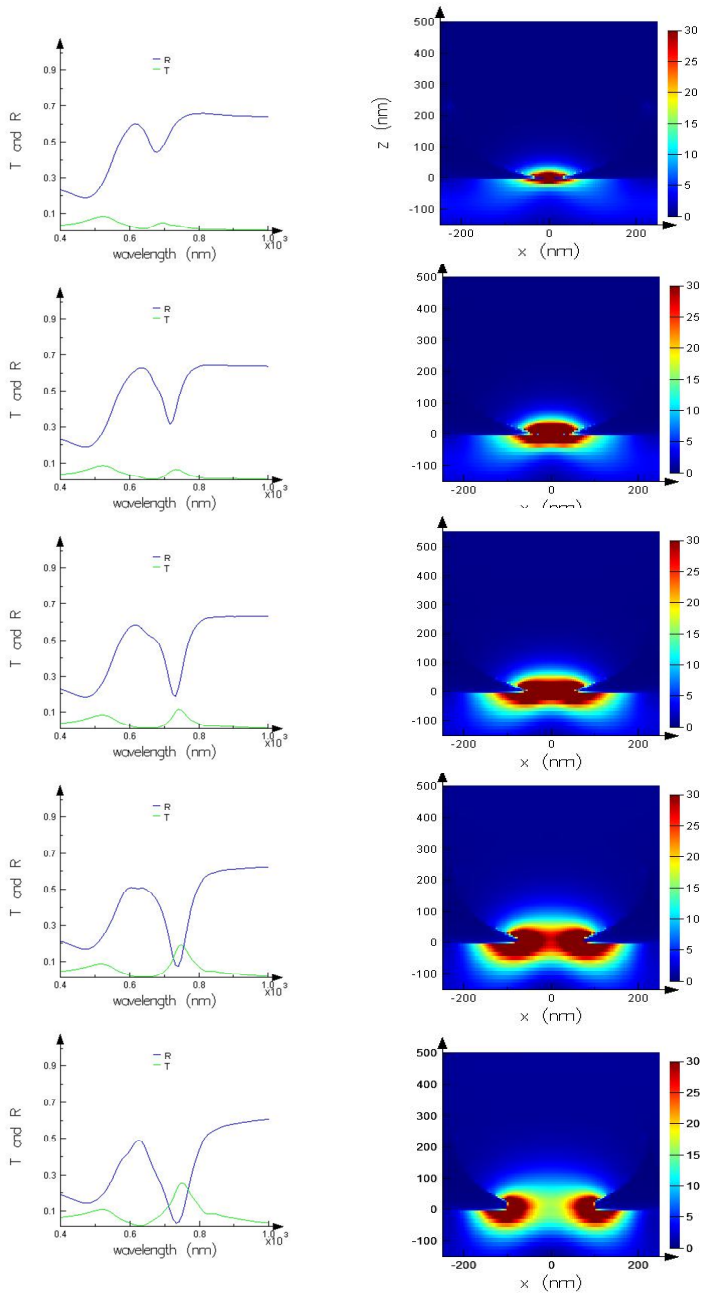

Figure A-13 The effect of the bottom hole size on the plasmonic properties of the void array structures. The simulated reflection and transmission spectra and corresponding plots of electric field distribution under resonant conditions in the refractive index 1 environment. All structures have a void diameter 450nm and film thickness 230nm. The bottom hole diameters are 20nm, 50nm, 100nm, 150nm, 200nm, respectively from the top.

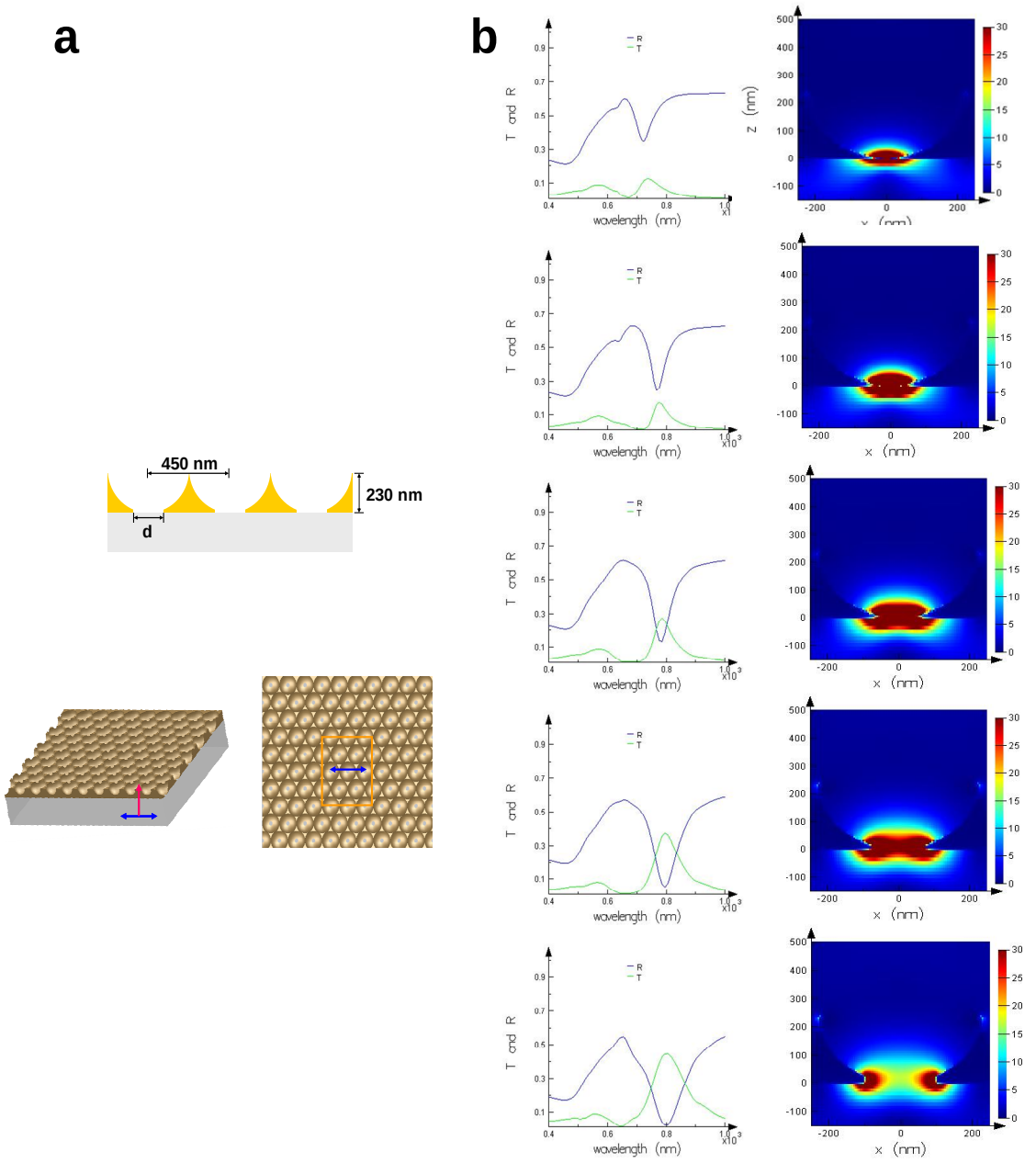

Figure A-14 The effect of the bottom hole size (d) on the SPR peaks and the distribution of enhanced electric field under resonant conditions when illuminated by light polarized along x axis (blue arrow) from the back side (red arrow) in the refractive index of medium 1.33. (a) Illustration of the structure simulated. The void diameter is 450 nm, the film thickness is 230 nm. (b) The simulated reflection and transmission spectra and corresponding plots of electric field distribution under resonant conditions. The bottom hole diameters are 20nm, 50nm, 100nm, 150nm, 200nm respectively from the top.

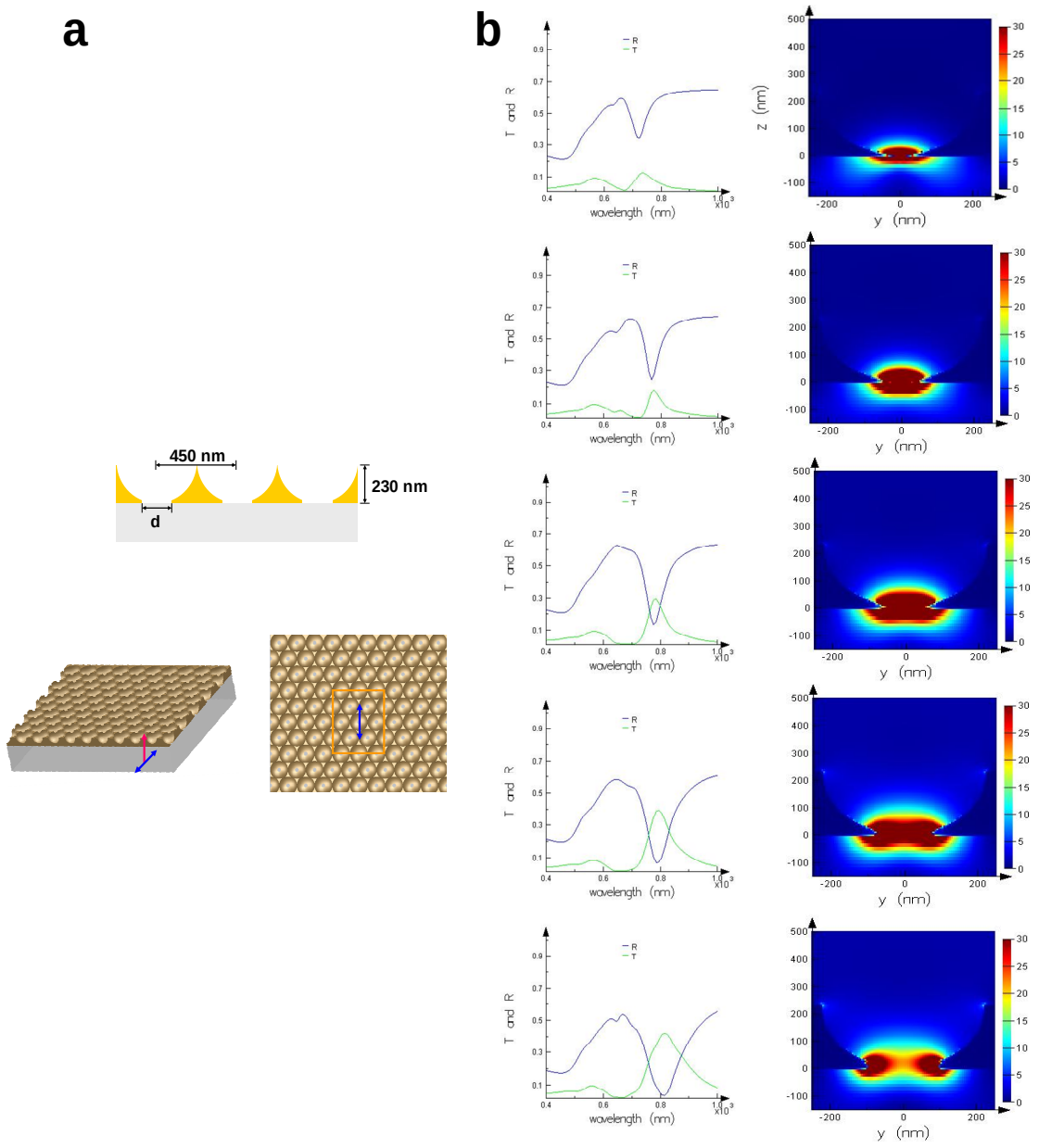

Figure A-15 The effect of the bottom hole size (d) on the SPR peaks and the distribution of enhanced electric field under resonant conditions when illuminated by light polarized along y axis (blue arrow) from the back side (red arrow) in the refractive index of medium 1.33. (a) Illustration of the structure simulated. The void diameter is 450 nm, the film thickness is 230 nm. (b) The simulated reflection and transmission spectra and corresponding plots of electric field distribution under resonant conditions. The bottom hole diameters are 20nm, 50nm, 100nm, 150nm, 200nm respectively from the top.

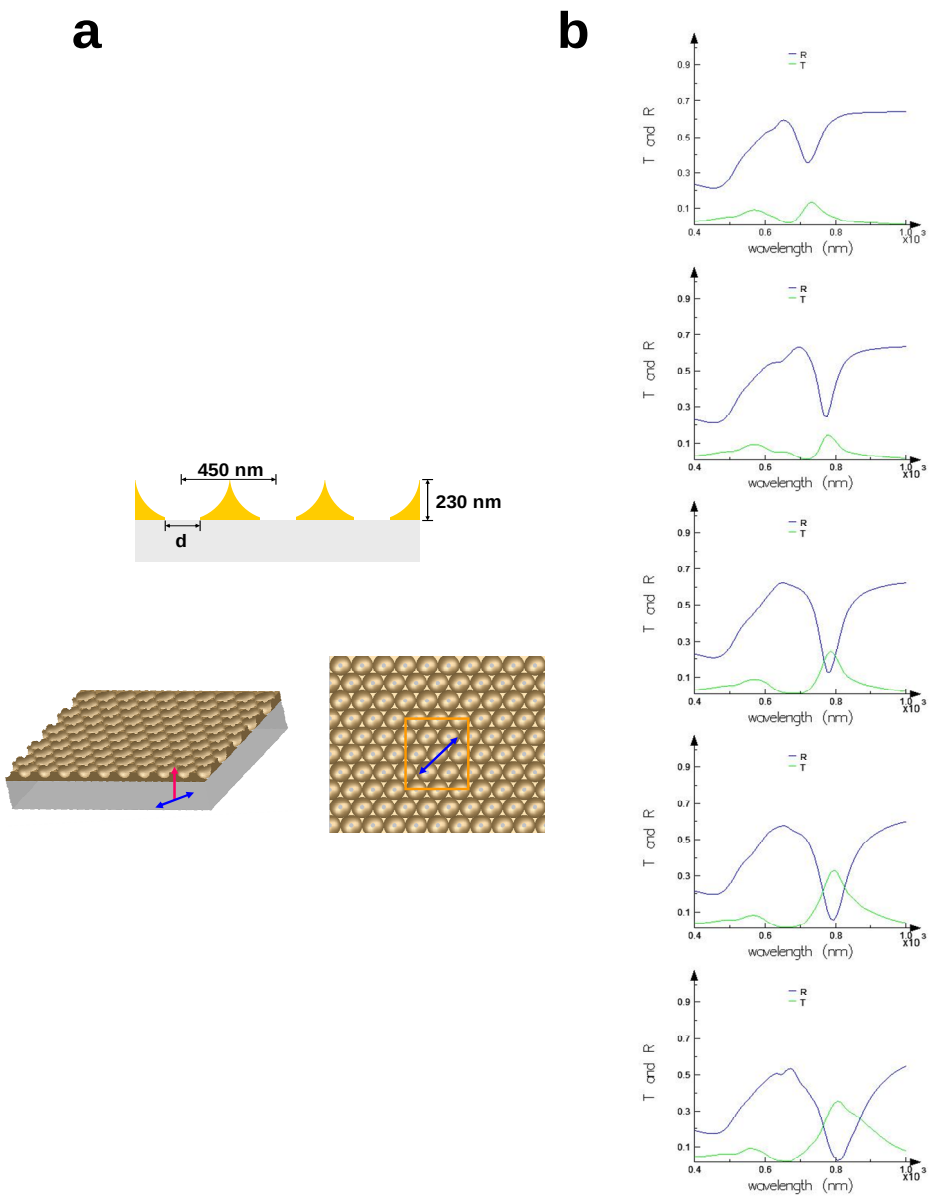

Figure A-16 The effect of the bottom hole size (d) on the SPR peaks when illuminated by light polarized along the direction of 45 degree with x axis (blue arrow) from the back side (red arrow) in the refractive index of medium 1.33. (a) Illustration of the structure simulated. The void diameter is 450 nm, the film thickness is 230 nm. (b) The simulated reflection and transmission spectra and corresponding plots of electric field distribution under resonant conditions. The bottom hole diameters are 20nm, 50nm, 100nm, 150nm, 200nm respectively from the top.

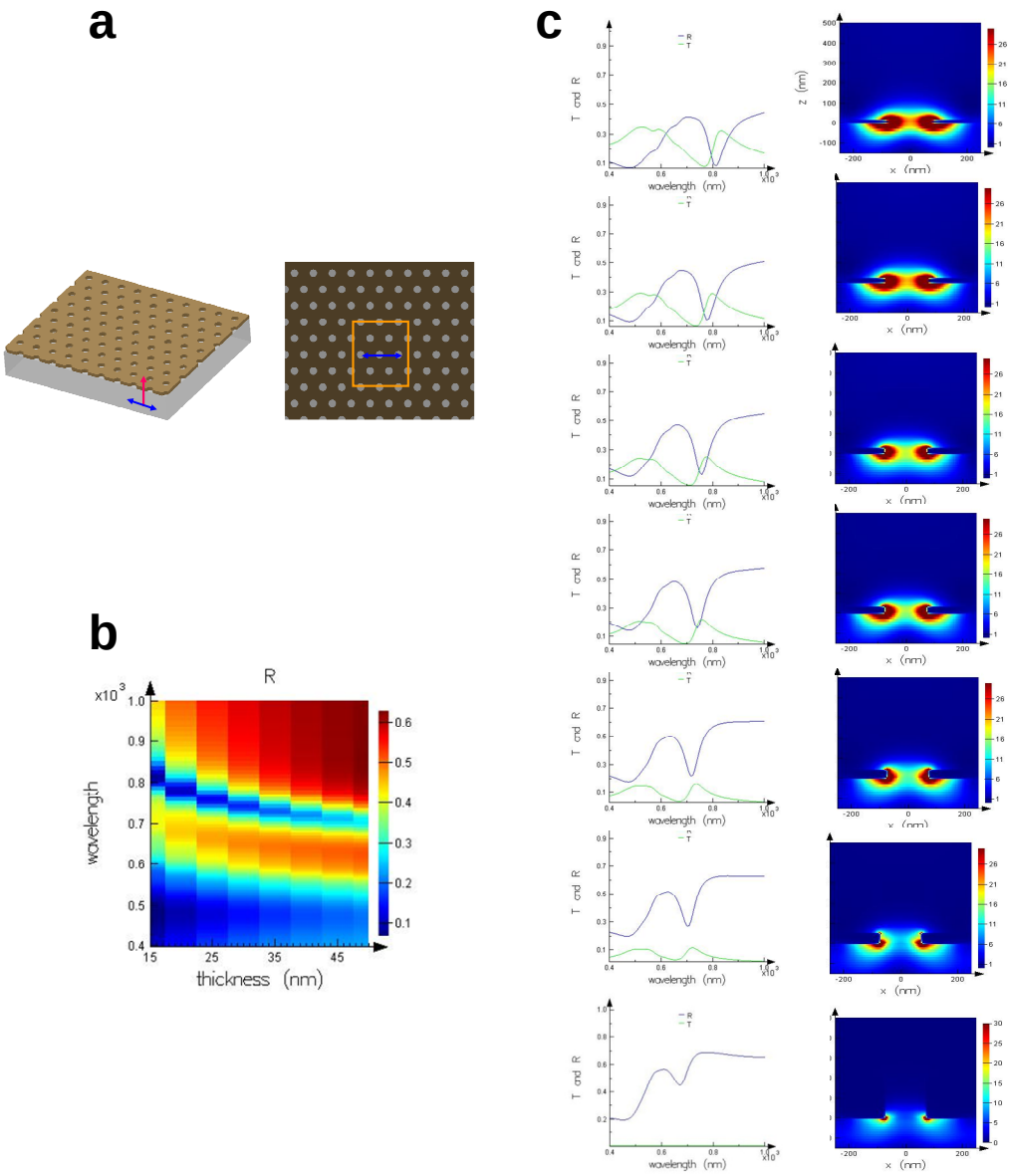

Figure A-17 The effect of the Au thickness on the plasmonic properties of the hole array structures. when illuminated by the light polarized along x axis (blue arrow) from the back side (red arrow) in the refractive index of medium 1.(a) Illustration of the structure simulated. (b) The plot of reflectivity of nanovoid arrays with different film thickness and at different wavelengths. The wavelength with the minimum reflectivity is the SPR wavelength. (c) The simulated reflection and transmission spectra and corresponding plots of electric field distribution under resonant conditions. All structures have a hole diameter 150nm and periodicity 450nm. The film thicknesses are 15nm, 20nm, 25nm, 30nm, 40nm, 50nm, 200nm respectively from the top.

REFERENCES

1. Stewart, M.E., et al., *Nanostructured plasmonic sensors.* Chemical Reviews, 2008. **108**(2): p. 494-521.

2. Homola, J., *Present and future of surface plasmon resonance biosensors.* Analytical and Bioanalytical Chemistry, 2003. **377**(3): p. 528-539.

3. Kim, P., et al., *Fabrication of nanostructures of polyethylene glycol for applications to protein adsorption and cell adhesion.* Nanotechnology, 2005. **16**(10): p. 2420-2426.

4. Israelachvili, J., *Intermolecular & Surface Forces*. 1991.

5. Warszynski, P. and Z. Adamczyk, *Calculations of double-layer electrostatic interactions for the sphere/plane geometry.* Journal of Colloid and Interface Science, 1997. **187**(2): p. 283-295.

6. Stankovich, J. and S.L. Carnie, *Electrical double layer interaction between dissimilar spherical colloidal particles and between a sphere and a plate: Nonlinear Poisson-Boltzmann theory.* Langmuir, 1996. **12**(6): p. 1453-1461.

7. Ohshima, H., *EFFECTIVE SURFACE-POTENTIAL AND DOUBLE-LAYER INTERACTION OF COLLOIDAL PARTICLES.* Journal of Colloid and Interface Science, 1995. **174**(1): p. 45-52.

8. Adamczyk, Z. and P. Warszynski, *Role of electrostatic interactions in particle adsorption.* Advances in Colloid and Interface Science, 1996. **63**: p. 41-149.

9. Johnson, C.A. and A.M. Lenhoff, *Adsorption of charged latex particles on mica studied by atomic force microscopy.* Journal of Colloid and Interface Science, 1996. **179**(2): p. 587-599.

10. Hanarp, P., et al., *Control of nanoparticle film structure for colloidal lithography.* Colloids and Surfaces a-Physicochemical and Engineering Aspects, 2003. **214**(1-3): p. 23-36.

11. Denis, F.A., et al., *Nanoscale chemical patterns fabricated by using colloidal lithography and self-assembled monolayers.* Langmuir, 2004. **20**(21): p. 9335-9339.
12. Oberholzer, M.R., et al., *2-D and 3-D interactions in random sequential adsorption of charged particles.* Journal of Colloid and Interface Science, 1997. **194**(1): p. 138-153.

13. Senger, B., J.C. Voegel, and P. Schaaf, *Irreversible adsorption of colloidal particles on solid substrates.* Colloids and Surfaces a-Physicochemical and Engineering Aspects, 2000. **165**(1-3): p. 255-285.

14. Semmler, M., et al., *Diffusional deposition of charged latex particles on water-solid interfaces at low ionic strength.* Langmuir, 1998. **14**(18): p. 5127-5132.

15. Antelmi, D.A. and O. Spalla, *Adsorption of nanolatex particles to mineral surfaces of variable surface charge.* Langmuir, 1999. **15**(22): p. 7478-7489.

16. Serizawa, T., S. Kamimura, and M. Akashi, *Electrostatic adsorption of polystyrene particles with different surface charges onto the surface of an ultrathin polymer film.* Colloids and Surfaces a-Physicochemical and Engineering Aspects, 2000. **164**(2-3): p. 237-245.

17. Xia, Y.N., et al., *Monodispersed colloidal spheres: Old materials with new applications.* Advanced Materials, 2000. **12**(10): p. 693-713.

18. Davis, K.E., W.B. Russel, and W.J. Glantschnig, *DISORDER-TO-ORDER TRANSITION IN SETTLING SUSPENSIONS OF COLLOIDAL SILICA - X-RAY MEASUREMENTS.* Science, 1989. **245**(4917): p. 507-510.

19. Miguez, H., et al., *Evidence of FCC crystallization of SiO2 nanospheres.* Langmuir, 1997. **13**(23): p. 6009-6011.

20. Pusey, P.N. and W. Vanmegen, *PHASE-BEHAVIOR OF CONCENTRATED SUSPENSIONS OF NEARLY HARD COLLOIDAL SPHERES.* Nature, 1986. **320**(6060): p. 340-342.

21. Dosho, S., et al., *RECENT STUDY OF POLYMER LATEX DISPERSIONS.* Langmuir, 1993. **9**(2): p. 394-411.

22. Park, S.H. and Y.N. Xia, *Assembly of mesoscale particles over large areas and its application in fabricating tunable optical filters.* Langmuir, 1999. **15**(1): p. 266-273.

23. Park, S.H., D. Qin, and Y. Xia, *Crystallization of mesoscale particles over large areas.* Advanced Materials, 1998. **10**(13): p. 1028-+.

24. Maier, S.A., *Plasmonics: Fundamentals and Applications*. 2007: Springer.
25. Fox, M., *Optical Properties of Solids*. 2006.

26. Long, D.A., *The Raman Effect*. 2002.

27. Aroca, R., *Surface-Enhanced Vibrational Spectroscopy*. 2007.

28. Fleischmann, M., *Raman spectra of pyridine adsorbed at a silver electrode* Chemical Physics Letters 1974. **26**(2): p. 163-166.

29. Jeanmaire, D.L. and R.P. Vanduyne, *Surface Raman spectroelectrochemistry.1. Heterocyclic, aromatic, and aliphatic-amines adsorbed on anodized silver electrode.* Journal of Electroanalytical Chemistry, 1977. **84**(1): p. 1-20.

30. Albrecht, M.G. and J.A. Creighton, *Anomalously interse Raman-spectra of pyridine at a silver electrode.* Journal of the American Chemical Society, 1977. **99**(15): p. 5215-5217.

31. Kerker, M., *Founding-fathers of light-scattering and surface-enhanced Raman-scattering.* Applied Optics, 1991. **30**(33): p. 4699-4705.

32. Gersten, J.I., *Rayleigh, Mie, and Raman-scattering by molecules adsorbed on rough surfaces.* Journal of Chemical Physics, 1980. **72**(10): p. 5780-5781.

33. Moskovits, M., *Surface-enhanced spectroscopy.* Reviews of Modern Physics, 1985. **57**(3): p. 783-826.

34. Otto, A., *Surface-enhanced Raman-scattering- classical and chemical origins.* Topics in Applied Physics, 1984. **54**: p. 289-418.

35. Kneipp, K., *Surface-enhanced Raman scattering.* Physics Today, 2007. **60**(11): p. 40-46.

36. Su, L., T.H. Lee, and S.R. Elliott, *Evanescent-wave excitation of surface-enhanced Raman scattering substrates by an optical-fiber taper.* Opt Lett, 2009. **34**(17): p. 2685-7.

37. Shi, C., et al., *Molecular fiber sensors based on surface enhanced Raman scattering (SERS).* J Nanosci Nanotechnol, 2009. **9**(4): p. 2234-46.

38. Oo, M.K., et al., *Forward-propagating surface-enhanced Raman scattering and intensity distribution in photonic crystal fiber with immobilized Ag nanoparticles.* Opt Lett, 2009. **34**(7): p. 968-70.

39. Lan, X., et al., *Surface-enhanced Raman-scattering fiber probe fabricated by femtosecond laser.* Opt Lett, 2009. **34**(15): p. 2285-7.

40. Kostovski, G., et al., *Nanoimprinted optical fibres: Biotemplated nanostructures for SERS sensing.* Biosens Bioelectron, 2009. **24**(5): p. 1531-5.

41. Kim, K., et al., *Novel fabrication of au nanoparticle films on planar and curved surfaces of glass and fiber materials.* Langmuir, 2009. **25**(17): p. 9697-702.

42. Zheng, X., et al., *Photochemical modification of an optical fiber tip with a silver nanoparticle film: a SERS chemical sensor.* Langmuir, 2008. **24**(8): p. 4394-8.

43. Yan, H., et al., *Novel index-guided photonic crystal fiber surface-enhanced Raman scattering probe.* Opt Express, 2008. **16**(11): p. 8300-5.

44. White, D.J. and P.R. Stoddart, *Nanostructured optical fiber with surface-enhanced Raman scattering functionality.* Opt Lett, 2005. **30**(6): p. 598-600.

45. Smythe, E.J., et al., *Optical antenna arrays on a fiber facet for in situ surface-enhanced Raman scattering detection.* Nano Lett, 2009. **9**(3): p. 1132-8.

46. Xie, Z., et al., *Broad spectral photonic crystal fiber surface enhanced Raman scattering probe.* Applied Physics B-Lasers and Optics, 2009. **95**(4): p. 751-755.

47. Lan, X., et al., *Surface-enhanced Raman-scattering fiber probe fabricated by femtosecond laser.* Opt Lett, 2009. **34**(15): p. 2285-7.

48. Shi, C., et al., *A double substrate "sandwich" structure for fiber surface enhanced Raman scattering detection.* Applied Physics Letters, 2008. **92**(10): p. 3.

49. Lucotti, A. and G. Zerbi, *Fiber-optic SERS sensor with optimized geometry.* Sensors and Actuators B-Chemical, 2007. **121**(2): p. 356-364.

50. Hankus, M.E., et al., *Surface-enhanced Raman scattering-based nanoprobe for high-resolution, non-scanning chemical imaging.* Analytical Chemistry, 2006. **78**(21): p. 7535-7546.

51. Gessner, R., et al., *The application of a SERS fiber probe for the investigation of sensitive biological samples.* Analyst, 2004. **129**(12): p. 1193-1199.

52. Viets, C. and W. Hill, *Single-fibre surface-enhanced Raman sensors with angled tips.* Journal of Raman Spectroscopy, 2000. **31**(7): p. 625-631.
53. Stokes, D.L. and T. Vo-Dinh, *Development of an integrated single-fiber SERS sensor.* Sensors and Actuators B-Chemical, 2000. **69**(1-2): p. 28-36.

54. Zhang, Y., et al., *Liquid core photonic crystal fiber sensor based on surface enhanced Raman scattering.* Applied Physics Letters, 2007. **90**(19): p. 3.

55. Cox, F.M., et al., *Surface enhanced Raman scattering in a hollow core microstructured optical fiber.* Optics Express, 2007. **15**(21): p. 13675-13681.

56. Smythe, E.J., et al., *A Technique to Transfer Metallic Nanoscale Patterns to Small and Non-Planar Surfaces.* Acs Nano, 2009. **3**(1): p. 59-65.

57. Smythe, E.J., et al., *Optical Antenna Arrays on a Fiber Facet for in Situ Surface-Enhanced Raman Scattering Detection.* Nano Letters, 2009. **9**(3): p. 1132-1138.

58. Adamczyk, Z., et al., *KINETICS OF LOCALIZED ADSORPTION OF COLLOID PARTICLES.* Advances in Colloid and Interface Science, 1994. **48**: p. 151-280.

59. Denkov, N.D., et al., *Mechanism of formation of 2-dimensional crystals from latex-particles on substrated.* Langmuir, 1992. **8**(12): p. 3183-3190.

60. Denkov, N.D., et al., *2-DIMENSIONAL CRYSTALLIZATION.* Nature, 1993. **361**(6407): p. 26-26.

61. Kralchevsky, P.A., et al., *CAPILLARY MENISCUS INTERACTION BETWEEN COLLOIDAL PARTICLES ATTACHED TO A LIQUID-FLUID INTERFACE.* Journal of Colloid and Interface Science, 1992. **151**(1): p. 79-94.

62. Larsen, A.E. and D.G. Grier, *Like-charge attractions in metastable colloidal crystallites.* Nature, 1997. **385**(6613): p. 230-233.

63. Sangani, A.S., et al., *Capillary force on particles near a drop edge resting on a substrate and a criterion for contact line pinning.* Physical Review E, 2009. **80**(1): p. 15.

64. Coyle, S., et al., *Confined Plasmons in Metallic Nanocavities.* Physical Review Letters, 2001. **87**(17): p. 176801.

65. Kelf, T.A., et al., *Localized and delocalized plasmons in metallic nanovoids.* Physical Review B, 2006. **74**(24): p. 12.

66. Cole, R.M., et al., *Understanding plasmons in nanoscale voids.* Nano Letters, 2007. **7**(7): p. 2094-2100.

67. Mahajan, S., et al., *Relating SERS Intensity to Specific Plasmon Modes on Sphere Segment Void Surfaces.* Journal of Physical Chemistry C, 2009. **113**(21): p. 9284-9289.

68. Teperik, T.V. and V.V. Popov, *Strong coupling of light to flat metals via a buried nanovoid lattice: the interplay of localized and free plasmons.* Optics Express, 2006. **14**(5): p. 1965-1972.

69. Teperik, T.V., et al., *Mie plasmon enhanced diffraction of light from nanoporous metal surfaces.* Optics Express, 2006. **14**(25): p. 11964-11971.

70. *http://ab-initio.mit.edu/wiki/index.php/Meep_Introduction*.

71. Han, X.X., B. Zhao, and Y. Ozaki, *Surface-enhanced Raman scattering for protein detection.* Analytical and Bioanalytical Chemistry, 2009. **394**(7): p. 1719-1727.

BIOGRAPHICAL INFORMATION

Shih-Hsin Chang received his B.S. in Chemical Engineering from Chinese Culture University in1993, his M.E. in Materials Science and Engineering from University of Texas at Arlington in 2004, and later his Ph.D. degree in Materials Science and Engineering from University of Texas at Arlington in 2010 under the supervision of Dr. Yauwu Hao. His research projects were focused on the optical properties of nano-structures and their applications as the sensors.